

Manipulating the magnetic anisotropy  
in the ferromagnetic semiconductor  
Gallium Manganese Arsenide

Arianna Casiraghi, BSc, MSc

Thesis submitted to the University of Nottingham

for the degree of Doctor of Philosophy

July 2012

# Abstract

Since its first successful growth in 1996, the ferromagnetic semiconductor (Ga,Mn)As has had a great influence on the research field of semiconductor spintronics. Among the outstanding characteristics of this material the large spin-orbit interaction for the holes in the valence band plays a major role, since it is responsible for some of the most interesting properties of (Ga,Mn)As, like the magnetocrystalline anisotropy, the magnetoelastic coupling and the extraordinary contributions to the magnetotransport. Furthermore, the combination of large magnetic anisotropies, large spin stiffness and relatively small magnetic moments renders (Ga,Mn)As a hard ferromagnetic system with excellent micromagnetic properties, including mean-field like magnetization and macroscopic single-domain characteristics, that can be described both phenomenologically and microscopically, thanks to the relatively simple band structure. Finally, the interplay between ferromagnetism and semiconductivity, arising from the hole-mediated nature of the ferromagnetic interaction in (Ga,Mn)As, allows for the remarkable possibility of manipulating its magnetic properties by varying the state of the holes using non-magnetic parameters like electric fields, electric currents, light or strain. This circumstance could in principle be very useful to improve the process of writing information in magnetic memories, which is currently performed, not very efficiently, with magnetic fields. However, it does seem unlikely that (Ga,Mn)As will become a relevant material for technological applications since the highest Curie temperature so far obtained for (Ga,Mn)As is still well below room temperature. Nonetheless the study of (Ga,Mn)As remains a fervent research area since it allows to explore a variety of novel functionalities and spintronics concepts that could in future be implemented in other systems. For this reason (Ga,Mn)As is often referred to as a test bench material for semiconductor spintronics.

This Thesis presents the results of a series of experimental investigations showing how different approaches can be used to manipulate the magnetic anisotropy in (Ga,Mn)As thin films.

In Chapter 4 the properties of the ferromagnetic semiconductor (Ga,Mn)(As,P) are investigated through structural, magnetometry, transport and magnetotransport measurements. By varying the amount of phosphorus incorporated it is possible to vary the sign of the in-built growth strain, to which the magnetic ani-

sotropy in (Ga,Mn)As is extremely sensitive. It is in fact shown that samples with large enough phosphorus concentrations are characterized by a perpendicular-to-plane magnetic easy axis, which is an extremely useful property since it allows to detect the orientation of the magnetization via anomalous Hall effect and polar magneto-optical Kerr effect. Furthermore, it is demonstrated that by varying the temperature or the post-growth annealing time it is possible to obtain a reorientation of the magnetic easy axis from an in-plane direction to the perpendicular-to-plane direction in some samples, which is another interesting aspect of this material.

Chapter 5 consists of a study exploring the effects of piezoelectric-induced strain on the magnetic anisotropy of a highly-doped annealed (Ga,Mn)As sample bonded to a piezoelectric actuator. It is shown that large and reversible rotations of the magnetic easy axis can be achieved in this sample by varying the voltage applied to the piezoelectric actuator, thus demonstrating that strain-mediated electric control of ferromagnetism is effective even in the limit of high doping levels and high Curie temperatures, where direct electric control of ferromagnetism via carrier manipulation is not possible. Furthermore, the results obtained from magnetotransport and SQUID magnetometry measurements are compared, extracting the dependence of the piezo-induced uniaxial magnetic anisotropy constant upon strain in both cases and discussing why the magnetotransport measurements are believed to be more accurate than SQUID magnetometry measurements in evaluating the inverse magnetostriction effects in (Ga,Mn)As-piezoelectric actuator hybrid systems.

Finally, Chapter 6 contains the results of an investigation attempting to use ultrashort strain pulses to switch the magnetization direction in a (Ga,Mn)(As,P) sample on fast time scales. These pulses are generated by femtosecond optical excitation of a metal transducer film deposited on the back of the substrate and travel ballistically through it until they reach the sample under investigation. Despite demonstrating that this method can indeed be used to induce a fast irreversible switching of the magnetization orientation in the (Ga,Mn)(As,P) sample, time-resolved magnetotransport measurements show that the switching is not triggered by the strain pulse, but rather by the transverse heat pulse, the latter being generated with the strain pulse during the optical excitation of the metal film. It is shown that the switching occurs through domain-related processes and the possible mechanisms behind its cause are speculated.

# List of publications

A. Casiraghi, A. W. Rushforth, M. Wang, N. R. S. Farley, P. Wadley, J. L. Hall, C. R. Staddon, K. W. Edmonds, R. P. Campion, C. T. Foxon, and B. L. Gallagher, “*Tuning perpendicular magnetic anisotropy in (Ga,Mn)(As,P) by thermal annealing*”, Appl. Phys. Lett. **97**, 122504 (2010).

D. Fang, H. Kurebayashi, J. Wunderlich, K. Vyborny, L. P. Zârbo, R. P. Campion, A. Casiraghi, B. L. Gallagher, T. Jungwirth, and A. J. Ferguson, “*Spin-orbit-driven ferromagnetic resonance*”, Nat. Nanotechnol. **6**, 413 (2011).

P. Wadley, A. Casiraghi, M. Wang, K. W. Edmonds, R. P. Campion, A. W. Rushforth, B. L. Gallagher, C. R. Staddon, K. Y. Wang, G. van der Laan, and E. Arenholz, “*Polarized x-ray spectroscopy of quaternary ferromagnetic semiconductor (Ga,Mn)(As,P) thin films*”, Appl. Phys. Lett. **99**, 022502 (2011).

A. Casiraghi, P. Walker, A. V. Akimov, K. W. Edmonds, A. W. Rushforth, E. De Ranieri, R. P. Campion, B. L. Gallagher, and A. J. Kent, “*Fast switching of magnetization in the ferromagnetic semiconductor (Ga,Mn)(As,P) using nonequilibrium phonon pulse*”, Appl. Phys. Lett. **99**, 262503 (2011). Also selected for publication in the Virtual Journal of Ultrafast Science.

A. Casiraghi, A. W. Rushforth, J. Zemen, J. A. Haigh, M. Wang, K. W. Edmonds, R. P. Campion, and B. L. Gallagher, “*Piezoelectric strain induced variation of the magnetic anisotropy in a high Curie temperature (Ga,Mn)As sample*”, arXiv:1205.3725v1 [cond-mat], submitted to Appl. Phys. Lett.

E. De Ranieri, P. E. Roy, D. Fang, E. K. Vehstedt, A. C. Irvine, D. Heiss, A. Casiraghi, R. P. Campion, B. L. Gallagher, T. Jungwirth and J. Wunderlich, “*Piezo-electric control of the mobility of a domain wall driven by adiabatic and non-adiabatic torques*”, submitted to Nature Mater.

# Acknowledgements

The Thesis presented here would not have come to fruition had it not been for the support of my supervisor, Prof. Bryan Gallagher, whose advice has always been very appreciated. I am also extremely grateful to Dr. Andrew Rushforth and Prof. Kevin Edmonds, for their close guidance throughout my Ph.D.

A large proportion of my time as a postgraduate student at the University of Nottingham has been spent collaborating with the Terahertz Acoustics group. Here I have had the pleasure to work with Prof. Anthony Kent and Prof. Andrey Akimov, to whom I am indebted for having guided me through the realization of a successful experiment. I am also grateful to Dr. Paul Walker and Dr. David Fowler for their hands-on help in the lab.

There are several other people from the University of Nottingham that I would like to thank: Dr. Richard Campion and Prof. Tom Foxon for growing the wafers on which the experiments described in this Thesis have been performed; Jas Chauhan, Dave Taylor and Dr. Ehsan Ahmad for their advice on sample fabrication; Stephen Booth, Robert Chettle, David Holt and Peter Smith for technical support; and Christopher Pallender for providing liquid Helium. I am also grateful to the past and present occupants of the “Advanced Semiconductor Spintronics” office – Adam, Chris, Vicky, Jacky, Robin, Mu, Pete, James, Lucy, Duncan, Fintan and Bryn, for their help with Physics but mostly for having made it so fun to share an office with them. Thanks guys!

I count myself lucky to have had the opportunity to collaborate with research groups from other European Universities. I would like to thank Dr. Elisa De Ranieri and Dr. Jörg Junderlilch from Hitachi Cambridge Laboratory for allowing me to use their MOKE microscope and for useful discussions; Dr. Andrew Irvine from the Cavendish Laboratory of the University of Cambridge for fabricating high quality nanostructures for some of my measurements; Dr. Jan Zemen and Prof. Tomas Jungwirth from the Institute of Physics in Prague for theoretical calculations and guidance; Dr. Thibault Devolder from Institut d’Électronique Fondamentale of Université Paris Sud for giving me the opportunity to make measurements in his Lab. I am also grateful to all the members of the Namaste and SemiSpinNet European networks, that I have had the pleasure to be part of, for all the useful meetings and discussions from which I have learnt a lot.

Finally I would like to thank my dad, grandpa and grandma, whom I have lost during this Ph.D., my mum, aunt and uncle, and Dan for loving and supporting me always.

# Contents

<b>Abstract</b>	<b>ii</b>
<b>List of publications</b>	<b>iv</b>
<b>Acknowledgements</b>	<b>v</b>
<b>1 Introduction</b>	<b>1</b>
1.1 Spintronics . . . . .	1
1.2 Ferromagnetic semiconductors . . . . .	3
1.3 Thesis layout . . . . .	4
<b>2 Properties of (Ga,Mn)As</b>	<b>6</b>
2.1 Growth . . . . .	6
2.2 Crystal structure . . . . .	7
2.3 Origin of ferromagnetism . . . . .	9
2.4 Spin-orbit interaction . . . . .	10
2.5 Magnetic properties . . . . .	11
2.5.1 Curie temperature . . . . .	11
2.5.2 Magnetization . . . . .	12
2.5.3 Magnetic anisotropy . . . . .	13
2.5.4 Magnetic domains . . . . .	16
2.6 Transport properties . . . . .	18
2.7 Magnetotransport properties . . . . .	19
2.7.1 Ordinary magnetotransport properties . . . . .	19
2.7.2 Extraordinary magnetotransport properties . . . . .	20
<b>3 Materials and experimental methods</b>	<b>25</b>
3.1 Materials . . . . .	25
3.2 Sample fabrication . . . . .	26
3.3 Measuring instruments and procedures . . . . .	28
3.3.1 SQUID magnetometer . . . . .	28
3.3.2 Transport and magnetotransport equipment . . . . .	32
3.3.3 Magneto-optical Kerr effect imaging equipment . . . . .	33

---

<b>4</b>	<b>Properties of (Ga,Mn)(As,P)</b>	<b>36</b>
4.1	Introduction . . . . .	36
4.2	Growth . . . . .	38
4.3	In-built growth strain . . . . .	39
4.4	SQUID magnetometry results . . . . .	41
4.5	Transport results . . . . .	48
4.6	Magnetotransport results . . . . .	49
4.7	Conclusions . . . . .	52
<b>5</b>	<b>Manipulation of the magnetization in (Ga,Mn)As using a piezo- electric actuator</b>	<b>54</b>
5.1	Introduction . . . . .	54
5.2	Experimental method . . . . .	55
5.2.1	Piezoelectric actuator characteristics . . . . .	55
5.2.2	Device fabrication . . . . .	57
5.3	Material characterization . . . . .	59
5.4	Magnetotransport results . . . . .	61
5.4.1	Transverse AMR in saturating magnetic field . . . . .	61
5.4.2	Dependence of $\Delta R$ on the magnetic field . . . . .	63
5.4.3	Effects of the piezoelectric actuator on the magnetic aniso- tropy . . . . .	64
5.5	SQUID magnetometry results . . . . .	70
5.5.1	Magnetic properties of the piezoelectric actuator . . . . .	71
5.5.2	Effects of the piezoelectric actuator on the magnetic aniso- tropy . . . . .	72
5.6	Results comparison . . . . .	74
5.7	Conclusions . . . . .	76
<b>6</b>	<b>Fast switching of the magnetization in (Ga,Mn)(As,P) using phonon pulses</b>	<b>78</b>
6.1	Introduction . . . . .	78
6.2	Experimental method . . . . .	80
6.2.1	Overview . . . . .	80
6.2.2	Strain pulse characteristics . . . . .	82
6.3	Experimental set-up and details . . . . .	84
6.4	Material characterization . . . . .	86
6.4.1	XRD measurements . . . . .	86
6.4.2	SQUID magnetometry measurements . . . . .	87
6.4.3	Transport measurements . . . . .	89
6.4.4	MOKE imaging measurements . . . . .	90
6.5	Static magnetotransport results . . . . .	91

---

6.6	Time-resolved magnetotransport results . . . . .	94
6.7	Conclusions . . . . .	97
<b>7</b>	<b>Summary and future work</b>	<b>99</b>
<b>A</b>	<b>Angles definition</b>	<b>103</b>
<b>B</b>	<b>List of acronyms</b>	<b>104</b>
<b>C</b>	<b>Conversion of magnetic units</b>	<b>106</b>
	<b>Bibliography</b>	<b>107</b>

# Chapter 1

## Introduction

### 1.1 Spintronics

Since the realization of the silicon transistor in 1954 and the development of the integrated circuit in 1959, the field of information and communication technologies has experienced a huge growth and increased its importance in everyday life. This rapid progress has been achieved thanks to a continuous miniaturization of the transistors, which has allowed for electronic devices of increasingly higher performance and lower cost to be fabricated. Moore's law [1] describes quantitatively this trend: formulated as early as 1965, this law predicted that the density of transistors on an integrated circuit would double approximately every year. Even if during the 1970s and 1980s the doubling time was closer to 18 months than 1 year [2], Moore's law proved overall to be accurate, partly because it was adopted by the semiconductor industry as a business plan to drive long-term goals. As a result of this, the latest available technologies employ transistors with features as small as 22 nm [3]. But since technical challenges increase dramatically with decreasing the features size, this scaling trend will unavoidably slow down and ultimately fundamental physical limits will be encountered. Therefore, in order for Moore's law to maintain its validity, it is necessary to go beyond the miniaturization of the existing technology and exploit new physical concepts [4].

One interdisciplinary research area that has emerged in the last few decades as a reply to these needs is known as spintronics. Its key concept is that of relying on the electron spin, and not only on its charge, to store and manipulate information. In fact, adding the spin degree of freedom to the existing, charged-based, semiconductor electronics can significantly improve the performance of electronic devices as well as enabling new functionalities [5, 6].

The foundations of spintronics can be traced back to the experiments performed in 1857 by Thomson (Lord Kelvin) [7], who first observed the existence of anisotropic magnetoresistance (AMR), i.e. the dependence of electrical resistance in a conductor upon the relative orientation between magnetization and current,

in ferromagnetic metals. A step forward was made in 1975 by Jullière [8] with his discovery that the tunneling resistance across a thin insulator layer separating two ferromagnetic layers could be modulated with a magnetic field, an effect known as tunneling magnetoresistance (TMR). But TMR did not attract much attention at the time and it was not until more recently, when in 1988 Fert *et al.* [9] and Grünberg *et al.* [10] independently discovered the existence of giant magnetoresistance (GMR), that spintronics has been universally acknowledged as a research area of major technological and economical impact. In fact, it is not surprising that Fert and Grünberg were awarded the Nobel Prize in Physics in 2007.

The simplest system in which GMR can be observed is a trilayer structure, also known as a spin valve, in which a non-magnetic metal layer is sandwiched between two layers of a ferromagnetic metal. GMR manifests itself as a dependence of the electrical resistance of the structure upon the relative orientation of the magnetization in the two ferromagnetic layers. Since the 1990s, GMR has been extensively employed in magnetic field sensors and read heads for magnetic hard disk drives. More recently, TMR has replaced GMR in read heads and has also become the basis for magnetoresistive random access memory (MRAM) [11], a type of memory that, being both quickly accessible and non-volatile, could develop into a “universal” memory, thus replacing both conventional random access memory (RAM) and hard disk drives. While these metal-based spintronic devices are dominating the area of information storage, information processing is still carried out in conventional, charged-based, semiconductor electronics. A major achievement for spintronics would be that of developing a device able to perform both these tasks. Two routes are currently being followed by researchers to attain this result: on one hand, the magnetic community is trying to implement logic functionalities in metals [12, 13, 14, 15] and, on the other hand, the semiconductor community is focussing on how to engineer and manipulate magnetism in semiconductors [16, 17, 18]. The latter approach has given rise to that area of spintronics known as semiconductor spintronics.

Semiconductor spintronics has also made impressive progress in the last decade but, despite this, the number of its technological applications is still very limited [19]. This is a remarkable aspect if it is thought that the first suggestion of a spin-based current modulator in a semiconductor was presented around 22 years ago [20]. Nonetheless, semiconductor spintronics remains a fervent research area, thanks to its huge potentialities. Not only it would easily integrate with the existing semiconductor technology and enable the development of devices that could perform both logic and memory operations, as we have mentioned, but it would also allow for a vast range of novel functionalities to be implemented. This is due to the fact that spin-dependent phenomena in semiconductors are char-

acterized by robust spin polarization, extremely long spin coherence times and optical accessibility, that could be interesting for photonics applications [17, 21].

Before exploring the field of semiconductor spintronics in more detail, it is worth mentioning for completeness that, alongside metals and semiconductors, more exotic systems are also being investigated for the development of spintronics. These include organic semiconductors [22], topological insulators [23] and graphene [24].

## 1.2 Ferromagnetic semiconductors

The key concept of semiconductor spintronics is that of exploiting the unique characteristics derived from the simultaneous presence of magnetic and semiconducting properties in the same physical system. These properties naturally coexist in magnetic semiconductors, such as europium (Eu) chalcogenides and semiconducting spinels [25], in which one or more constituting elements are magnetic. These systems have been known for a long time and were the first candidates to be chosen for the implementation of semiconductor spintronics. Unfortunately, they were found to be not easy to integrate with the semiconductors used in conventional electronics, silicon (Si) and gallium arsenide (GaAs) and were soon disregarded. Only recently, after overcoming various technical issues, the interest in these systems, especially in the Eu chalcogenides, has seen a revival [26].

A more favourable approach was found to be that of doping standard non-magnetic semiconductors with magnetic impurities, usually transition metal elements, to make them magnetic [16]. These materials are known as diluted magnetic semiconductors (DMS), since the concentration of the magnetic elements is much smaller than in standard magnetic semiconductors. The research study in DMS initially focussed on II–VI semiconductors [27], such as CdTe and ZnSe, in which manganese (Mn), the most common magnetic element used for doping, is an isoelectronic impurity. This circumstance allows for relatively large Mn densities to be incorporated in the host matrix during growth. Nonetheless, the Curie temperature ( $T_C$ ) of these II–VI DMS is extremely low, being at most  $\sim 1$  K [28, 29]. Much different is the case of III–V semiconductors, like InAs and GaAs, in which Mn is no longer an isoelectronic impurity and its equilibrium solubility limit is very low. For this reason, it was not until non-equilibrium growth techniques were used that III–V DMS could be obtained: layers of (In,Mn)As and (Ga,Mn)As successfully grown on GaAs were reported for the first time in 1989 [30] and 1996 [31], respectively. The fact that soon after its discovery (Ga,Mn)As was found to show ferromagnetic order with a  $T_C$  as high as 110 K [32] immediately raised a large interest for III–V DMS and ever since a great effort has been made to understand and exploit their properties.

As will be described in the next Chapter, the ferromagnetic order in DMS arises as a result of a long-range coupling between the magnetic impurity atoms mediated by the charge carriers [16]. This interplay between magnetism and semi-conductivity allows for the remarkable possibility of manipulating the magnetic behaviour in DMS by varying the state of the charge carriers using, for example, electric fields [33, 34], electric currents [35, 36], light [37, 38] or strain [39, 40, 41]. Being able to control the magnetic state of spintronics materials via non-magnetic parameters could be very useful to improve the process of writing information in magnetic memories, which is currently performed, not very efficiently, with magnetic fields [42].

If it is clear that DMS are characterized by several attractive properties, they still need to meet a key requirement before they can effectively be used as spintronics materials: that of retaining ferromagnetism at or above room temperature. Unfortunately, the highest  $T_C$  that has so far been obtained, around 185 K [43] for (Ga,Mn)As, is still very low and it does seem unlikely that (Ga,Mn)As or any other DMS will ever reach a  $T_C$  of technological relevance [44, 45]. Nonetheless, this area of research continues to grow since DMS are constantly being used as a test bench for the exploration of a variety of new spintronics concepts, some of which have already found the prospect of being developed in devices involving ferromagnetic metals. Moreover, the ongoing work on several candidate DMS may ultimately lead to the discovery of the ideal ferromagnetic semiconductor.

### 1.3 Thesis layout

Within the research field of DMS, (Ga,Mn)As has been by far the most carefully studied system and the best understood one. For this reason (Ga,Mn)As is often regarded as a reference model for DMS.

This Thesis presents the results of a series of experimental investigations showing how different approaches can be used to manipulate the magnetic anisotropy in (Ga,Mn)As thin films. Its contents are organised as follows. Chapter 2 is a literature review of the main structural, magnetic, transport and magnetotransport properties of (Ga,Mn)As. The microscopic mechanisms behind the origin of ferromagnetism in (Ga,Mn)As and the important role of the spin-orbit interaction in giving rise to some of its intriguing characteristics are also discussed. Chapter 3 provides a description of the properties of the materials studied, of the techniques used to fabricate the samples and of the experimental equipment employed to investigate them. Chapter 4 presents the results of structural, magnetometry, transport and magnetotransport measurements performed on a series of (Ga,Mn)(As,P) samples with different phosphorus concentrations, and shows how the magnetic anisotropy in these samples can be controlled by varying the

phosphorus concentration, the temperature and the annealing time. Chapter 5 comprises a study exploring the effects of piezoelectric-induced strain on the magnetic anisotropy of a highly-doped (Ga,Mn)As sample, demonstrating that large and reversible rotations of the magnetic easy axis can be achieved in the latter via this approach. Chapter 6 contains the results of an investigation showing that ultrashort acoustic pulses can be used to switch the magnetization direction in a (Ga,Mn)(As,P) sample on fast time scales. Finally, the conclusions are drawn in Chapter 7, together with plans for future work.

# Chapter 2

## Properties of (Ga,Mn)As

### 2.1 Growth

Under equilibrium growth conditions, the substitution of Mn for Ga in GaAs is limited to a very small value, roughly 0.1%, beyond which Mn atoms start to segregate. But in order to observe the establishment of cooperative ferromagnetism in (Ga,Mn)As, concentrations of Mn higher than its equilibrium solubility level are necessary. This is achieved using non-equilibrium growth methods, such as molecular beam epitaxy (MBE).

The growth of single crystals through MBE consists in the deposition of evaporated elements on the surface of a substrate material, which is kept in rotation around the growth axis to ensure a good uniformity level. The slow deposition rate typical of this method allows the material to grow epitaxially, while ultra-high vacuum conditions guarantee a high purity degree. The substrate temperature is an important variable of the process, since it affects the way adatoms are incorporated, ultimately determining the crystalline quality of the material grown. In standard MBE growth of GaAs the substrate temperature is quite high, typically  $\sim 600$  °C, to ensure good crystal quality. However, when growing (Ga,Mn)As under these conditions, Mn atoms accumulate on the surface and combine with As atoms [46]. This problem is overcome by using low-temperature MBE (LT-MBE), in which the substrate is kept at a temperature  $< 300$  °C. The excess of Mn on the surface during growth can induce a transition from two dimensional (2D) to three dimensional (3D) growth conditions [47]. Since layers grown under 2D conditions and close to the 2D/3D boundary show the best properties, the substrate temperature for (Ga,Mn)As is chosen to be the highest possible while maintaining 2D growth conditions. Given that decreasing the substrate temperature reduces the segregation of Mn at the surface, the optimal substrate temperature decreases with increasing the Mn concentration [47], as shown in Fig. 2.1. The first successful growth of ferromagnetic (Ga,Mn)As with negligible second phase segregations was obtained via LT-MBE in 1996 [31]. Since then,

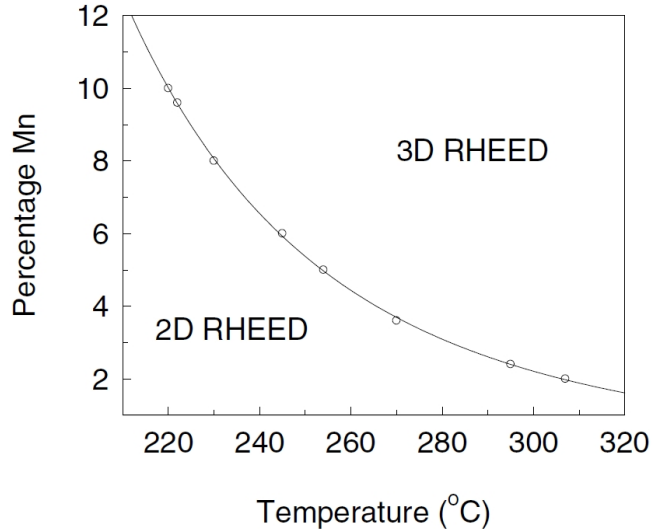


Figure 2.1: Surface phase diagram for the growth of (Ga,Mn)As. Reflection high-energy electron diffraction (RHEED) is used to monitor in real time the growth conditions. Image taken from [48].

LT-MBE has become a well established technique to grow (Ga,Mn)As layers.

## 2.2 Crystal structure

It is well known that GaAs crystallizes in the zinc-blende structure, which consists of two interpenetrating face-centred cubic lattices, each displaced from the other by a quarter of the lattice constant along the body diagonal of the cubic cell. X-ray diffraction (XRD) measurements show that also (Ga,Mn)As grown on GaAs via LT-MBE has the zinc-blende structure, without detectable second phase.

The most stable, and hence, most common position of Mn in the host GaAs matrix is on the Ga site ( $\text{Mn}_{\text{Ga}}$ ), as can be understood from the electronic configuration of the elements in (Ga,Mn)As:  $[\text{Ga}] = [\text{Ar}]3d^{10}4s^24p^1$ ,  $[\text{Mn}] = [\text{Ar}]3d^54s^2$  and  $[\text{As}] = [\text{Ar}]3d^{10}4s^24p^3$ . In this way, the two Mn  $4s$ -electrons participate in the crystal bonding in the same way as the two Ga  $4s$ -electrons and, because of the missing valence  $4p$ -electron,  $\text{Mn}_{\text{Ga}}$  acts as an acceptor. For this reason, each  $\text{Mn}_{\text{Ga}}$  atom is responsible for the presence in (Ga,Mn)As not only of a local magnetic moment (due to the half-filled  $d$  shell), but also of a hole.

$\text{Mn}_{\text{Ga}}$  atoms are not the only impurities introduced in GaAs while growing (Ga,Mn)As via LT-MBE. In fact, for Mn concentrations  $\gtrsim 1.5\%$  a fraction of Mn is unavoidably incorporated during growth in interstitial positions [49, 50], while the low substrate temperature characteristic of this growing technique is responsible for the occurrence of antisite defects (As atoms on cation sites) [51]. The unit cell of (Ga,Mn)As containing substitutional Mn ( $\text{Mn}_{\text{Ga}}$ ), interstitial Mn

$(\text{Mn}_\text{I})$  and As antisites ( $\text{As}_{\text{Ga}}$ ) impurities is shown in Fig. 2.2. Both  $\text{Mn}_\text{I}$  and

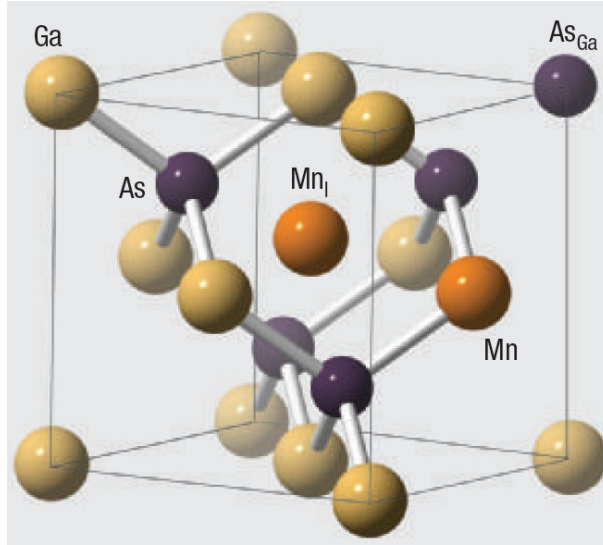


Figure 2.2: The zinc-blende unit cell of  $(\text{Ga},\text{Mn})\text{As}$ . Substitutional Mn ( $\text{Mn}_{\text{Ga}}$ ), interstitial Mn ( $\text{Mn}_\text{I}$ ) and As antisites ( $\text{As}_{\text{Ga}}$ ) impurities are shown.

$\text{As}_{\text{Ga}}$  impurities act as double donors, thus compensating for the holes provided by two  $\text{Mn}_{\text{Ga}}$  atoms. The consequent reduction of the hole concentration represents a major disadvantage for the onset of ferromagnetism, holes being the mediators of the ferromagnetic coupling in  $(\text{Ga},\text{Mn})\text{As}$ . A further issue is represented by the antiferromagnetic coupling that takes place between pairs of  $\text{Mn}_\text{I}$  and  $\text{Mn}_{\text{Ga}}$  (formed during growth via Coulomb interaction [52]) that reduces the total magnetic moment of  $(\text{Ga},\text{Mn})\text{As}$  layers [53].

Some solutions have been found to minimize the occurrence of these charge and moment compensating defects. It has been shown that a substantial decrease of  $\text{Mn}_\text{I}$  can be obtained via post-growth annealing at temperatures close to the growth temperatures [54]: in this way  $\text{Mn}_\text{I}$  are out diffused towards the surface, where they are passivated by oxidation [55]. As antisites are instead stable up to 450 °C [56] and thus cannot be simply removed by low temperature post-growth annealing. On the other hand, it has been shown that As antisites can be effectively reduced during growth by using As dimers ( $\text{As}_2$ ), that have a shorter surface lifetime, instead of As tetramers ( $\text{As}_4$ ), while maintaining a stoichiometric growth [47].

$(\text{Ga},\text{Mn})\text{As}$  layers grown on GaAs are fully strained up to the rather high thickness of  $\sim 1 \mu\text{m}$  [57], probably due to the low growth temperature which prevents dislocations from nucleating. This means that the in-plane lattice constant  $a_\parallel$  of  $(\text{Ga},\text{Mn})\text{As}$  grown on GaAs is equal to that of GaAs. The relaxed lattice constant  $a$  of  $(\text{Ga},\text{Mn})\text{As}$  can then be obtained by measuring with XRD the perpendicular lattice constant  $a_\perp$  and assuming that the elastic constants of

(Ga,Mn)As are equal to those of GaAs, i.e. with a Poisson ratio  $\nu = 0.31$  [31].  $a$  thus obtained is generally found to increase linearly with increasing the Mn concentration, following Vegard's law<sup>1</sup> [31]. As a consequence, (Ga,Mn)As layers grown on GaAs are under in-plane compressive strain. This condition is opposite to what could be intuitively expected when considering the values of the atomic radii of Mn ( $R_{\text{Mn}} = 1.17 \text{ \AA}$ ) and Ga ( $R_{\text{Ga}} = 1.25 \text{ \AA}$ ). In reality, the fact that (Ga,Mn)As has a larger lattice constant than that of GaAs is due to the longer length of the Mn–As bond with respect to the Ga–As bond. Moreover, it has been shown that the presence of  $\text{Mn}_{\text{I}}$  and  $\text{As}_{\text{Ga}}$  impurities also contributes to increasing the lattice constant of (Ga,Mn)As [58]. Given that the concentration of these impurities strongly depends on the growth conditions, (Ga,Mn)As lattice constant is also found to depend on them [59].

## 2.3 Origin of ferromagnetism

In principle, there could be three possible electronic states for  $\text{Mn}_{\text{Ga}}$  atoms:  $A^0(d^4)$  and  $A^0(d^5 + \text{hole})$  for  $\text{Mn}^{3+}$ , and  $A^-(d^5)$  for  $\text{Mn}^{2+}$ .  $A^0$  and  $A^-$  denote neutral (ground state) and negatively charged (excited state) centres respectively, while the notation in parentheses represents the electronic configuration of the  $3d$  Mn electrons. In reality, there has been no strong experimental evidence to support the existence of  $A^0(d^4)$  centres in GaAs and it is now well established that the ground state of  $\text{Mn}_{\text{Ga}}$  atoms is represented by  $A^0(d^5 + \text{hole})$  centres, which form when  $A^0(d^4)$  centres trap tightly an electron in the  $3d$  shell and, having thus become negatively charged, can subsequently attract and bind a hole [60]. Hence, according to Hund's rules, each  $\text{Mn}_{\text{Ga}}$  atom provides a local magnetic moment with angular momentum  $L = 0$  and spin  $S = 5/2$ , and a weakly bound hole (binding energy  $E_b \sim 0.1 \text{ eV}$  [49]).

Among the various microscopic mechanisms that can couple local magnetic moments in a solid to give rise to long-range magnetic order, two are believed to play a role in (Ga,Mn)As<sup>2</sup>: Kramer's superexchange [61] and Zener's indirect exchange [62]. The superexchange mechanism occurs between non-neighbouring local magnetic moments via an intermediate non-magnetic atom and in (Ga,Mn)As is responsible for an antiferromagnetic coupling between  $\text{Mn}_{\text{Ga}}$  atoms [63]. The indirect exchange mechanism arises between  $d$ -shell or  $f$ -shell local magnetic moments via  $s$  or  $p$  itinerant carriers and in (Ga,Mn)As is responsible for a ferromagnetic coupling between  $\text{Mn}_{\text{Ga}}$  atoms [63]. The latter is the dominant mechanism

<sup>1</sup>Vegard's law is an approximate empirical rule according to which the lattice constant of an alloy is linearly related to the concentration of its constituents.

<sup>2</sup>The double exchange mechanism is not mentioned here since it is typically used to describe the onset of ferromagnetism in (Ga,Mn)As layers with very low Mn concentrations [49], that are not considered in this Thesis.

and thus accounts for the establishment of ferromagnetism in (Ga,Mn)As.

The indirect exchange mechanism in (Ga,Mn)As occurs via the hybridisation of the Mn  $3d$  orbitals with the GaAs  $4p$  valence orbitals, which can be described as follows. For an isolated  $\text{Mn}_{\text{Ga}}$  atom the filled, for instance spin-down  $\downarrow$ , Mn  $3d$  level is well within the valence band, while the empty spin-up  $\uparrow$  Mn  $3d$  level is above the Fermi energy. Due to the repulsion between states with the same spin,  $p$ - $d$  hybridization takes place, with the spin-down valence state being pushed up in energy relatively to the spin-up valence state, as shown in Fig. 2.3. This

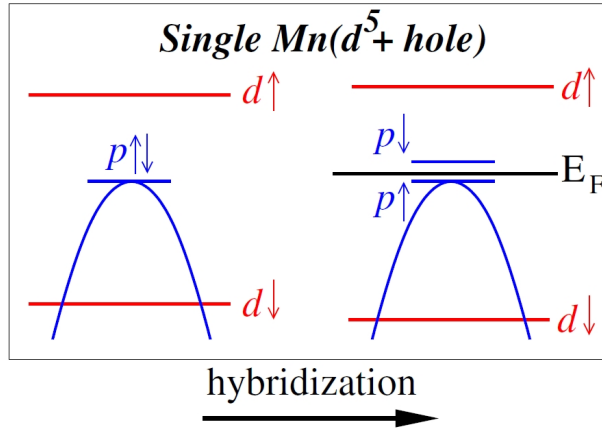


Figure 2.3: Electron-picture representation of the  $p$ - $d$  hybridization mechanism for an isolated  $\text{Mn}_{\text{Ga}}$  atom. Image taken from [49].

results in the establishment of an antiferromagnetic coupling between the spin of the valence carrier<sup>3</sup> and the spin of the  $3d$  electrons [49]. If now a many- $\text{Mn}_{\text{Ga}}$ -atom system is considered, it is possible to understand that the establishment of ferromagnetism can occur just at large enough Mn concentrations, i.e. when the average distance between  $\text{Mn}_{\text{Ga}}$  atoms becomes comparable with the average holes localization length, thus allowing the holes to mediate, via the  $p$ - $d$  hybridization mechanism, the ferromagnetic interaction between  $\text{Mn}_{\text{Ga}}$  local moments. The Mn doping level beyond which (Ga,Mn)As becomes ferromagnetic is  $\sim 1\%$  [47].

## 2.4 Spin-orbit interaction

The spin-orbit interaction is a relativistic phenomenon that accounts for the interaction between the spin angular momentum  $\mathbf{S}$  and the orbital angular momentum  $\mathbf{L}$  of a particle.

An electron orbiting a nucleus, having both  $\mathbf{S}$  and  $\mathbf{L}$  non-zero, experiences the spin-orbit interaction. In the reference frame where the electron is at rest, the

<sup>3</sup>Valence carriers in (Ga,Mn)As are holes but, for better clarity, Fig. 2.3 sketches the band structure for electrons.

nucleus is a positive charge orbiting it and, like a current, it generates an effective magnetic field  $\mathbf{B}_{\text{eff}}$  at the electron site. This field interacts with the electron spin through an Hamiltonian term of the form:

$$H_{SO} = \mathbf{B}_{\text{eff}} \cdot \mathbf{S} = \left( \frac{1}{2m_e^2 c^2} \nabla V \times \mathbf{p} \right) \cdot \mathbf{S}, \quad (2.1)$$

where  $m_e$  is the electron mass,  $c$  is the speed of light,  $\nabla V$  is the electric field generated by the nucleus at the electron site and  $\mathbf{p}$  is the electron momentum ( $\mathbf{L} = \mathbf{r} \times \mathbf{p}$ ) [49]. Via this Hamiltonian term, the orbital motion of the electron affects its spin orientation, and vice-versa. These remarks clearly hold also when a hole, rather than an electron, is being considered.

The spin-orbit splitting in the GaAs valence band is 0.34 eV, which is comparable to or larger than the Fermi energy in (Ga,Mn)As. Therefore, the spin-orbit interaction for the holes in the valence band of (Ga,Mn)As is remarkably large [49] and is responsible for the origin of some of the most interesting properties of (Ga,Mn)As, like the magnetocrystalline anisotropy, the magnetoelastic coupling and the extraordinary contributions to magnetotransport, which will be discussed in the following Sections.

## 2.5 Magnetic properties

### 2.5.1 Curie temperature

In its original form, the mean-field model description of ferromagnetism, based upon the  $p$ - $d$  Zener indirect exchange mechanism applied to a simple parabolic band structure, predicted that the Curie temperature  $T_C$  in (Ga,Mn)As should scale as  $x_{\text{eff}} \cdot p^{1/3}$ , where  $x_{\text{eff}}$  is the effective Mn concentration, i.e. the concentration of uncompensated Mn atoms<sup>4</sup>, and  $p$  is the hole concentration [63]. More recently, refinements to the mean-field model that include a more realistic band structure have shown that the dependence of  $T_C$  on  $p$  could actually be weaker than the initially found one, at least in the low hole compensation limit, while the linear dependence of  $T_C$  on  $x_{\text{eff}}$  has been confirmed [49]. According to these mean-field calculations, room temperature ferromagnetism should be achieved in weakly compensated (Ga,Mn)As for effective Mn concentrations of  $\sim 10\%$ .

The first successfully grown ferromagnetic (Ga,Mn)As had a  $T_C$  of about 60 K [31]. Since then, in just a couple of years,  $T_C$  increased to the remarkably large value of 110 K [32], generating a lot of enthusiasm in the semiconductor spintronics community. But 110 K remained the record  $T_C$  for many years,

---

<sup>4</sup> $x_{\text{eff}} = x_s - x_i$ , where  $x_s$  and  $x_i$  are the concentrations of substitutional and interstitial Mn atoms, respectively. Unless otherwise stated, for Mn concentration it is intended the nominal Mn concentration  $x = x_s + x_i = x_{\text{eff}} + 2x_i$ .

leading to suggesting that this could actually be a fundamental limit for  $T_C$  in (Ga,Mn)As [50]. However, it was later proven that  $T_C$  higher than 110 K could actually be reached when carefully controlled post-growth annealing procedures were employed [54, 55], leading to a substantial reduction of  $Mn_I$  atoms that are known to be detrimental to ferromagnetism in (Ga,Mn)As [53]. These improvements led to the achievement of  $T_C$  as high as 173 K for a sample with  $x_{eff} = 6.8\%$  ( $x = 9\%$ ) [64]. Further refinements in the growth and in post-growth annealing procedures have recently yielded the latest record  $T_C$  of 185 K for a sample with  $x_{eff} = 8.7\%$  ( $x = 12\%$ ) [43].

The dependence of  $T_C$  on  $x_{eff}$  has been following the predicted linear trend up to about  $x_{eff} = 6.8\%$  [49], becoming slightly sublinear for greater  $x_{eff}$  values. This is probably due to the fact that the growth of (Ga,Mn)As becomes increasingly hard for increasing  $x$  values, with more  $Mn_I$  and  $As_{Ga}$  impurities being incorporated. So, even if in principle  $T_C$  could increase further, the technological issues that have to be overcome to succeed are so challenging that it seems unlikely, at this stage, that (Ga,Mn)As ferromagnetic at room temperature will ever be grown.

## 2.5.2 Magnetization

The magnetization  $M$  of a layer of (Ga,Mn)As stems from the  $Mn_{Ga}$  atoms. As discussed in Section 2.3, each  $Mn_{Ga}$  atom is characterized by an angular momentum  $L = 0$  and a spin  $S = 5/2$ , thus providing a magnetic moment  $m = gS\mu_B = 5\mu_B$ , where  $g$  is the Landé  $g$  factor<sup>5</sup> and  $\mu_B = 9.274 \times 10^{-24}$  JT<sup>-1</sup> is the Bohr magneton. The antiferromagnetic coupling between  $Mn_{Ga}$  local moments and valence hole spins due to the  $p$ - $d$  hybridization mechanism should be responsible for a reduction of  $m$  [65]. The establishment of an antiferromagnetic coupling between pairs of  $Mn_{Ga}$  and  $Mn_I$  atoms is believed to be a further source of this reduction [53]. Finally, magnetic disorder could be enhanced by the anisotropic character of the  $Mn_{Ga}$ - $Mn_{Ga}$  interaction [66].

Having taken into account all these aspects, theoretical calculations based on the tight-binding model have predicted that the net magnetic moment per  $Mn_{Ga}$  atom  $m_{eff}$  should be  $\sim 5\%$ – $10\%$  smaller than its atomic value of  $5\mu_B$  [67]. Accordingly, experimental studies based on Superconducting Quantum Interference Device (SQUID) magnetometry and x-ray magnetic circular dichroism (XMCD) measurements have obtained  $m_{eff} \sim 4.5\mu_B$  for annealed (Ga,Mn)As samples with both low ( $x = 2.2\%$ ) and high ( $x = 8.4\%$ ) Mn content [53]. However, since the factors determining the value of  $m_{eff}$  are strongly sample dependent and since it is not always practical to perform time consuming experiments to extract it, it is

---

<sup>5</sup> $g = 2$  for an electron with  $L = 0$ .

usually assumed that the value of  $m_{eff}$  is in the range between  $4 \mu_B$  and  $5 \mu_B$ .

### 2.5.3 Magnetic anisotropy

Magnetic anisotropy is the dependence of the magnetic properties of a material upon the magnetization direction. In the absence of a magnetic field, the magnetization  $M$  of a magnetically isotropic material has no favourite direction while, in a material with magnetic anisotropy, it is aligned along one (or more) preferential direction(s), called magnetic easy axis (axes). Since a magnetic force needs to be applied in order to rotate  $M$  away from the easy axis (axes), it is possible to describe the magnetic anisotropy in terms of an anisotropy energy  $E_a$ <sup>6</sup>. In the simplest case of uniaxial magnetic anisotropy just one easy axis is present and  $E_a$  can be expressed as  $KV \sin^2 \theta$ , where  $K > 0$  is the magnetic anisotropy constant (measured in J/m<sup>3</sup>),  $V$  is the volume of the material and  $\theta$  is the angle between  $M$  and the easy axis direction.

There are various sources of magnetic anisotropy. The ones relevant to the samples that are used in this Thesis are magnetocrystalline, shape and strain anisotropies, for which a brief description follows. The reader can find further details in [68, 69].

**Magnetocrystalline anisotropy** This kind of anisotropy is the dependence of the magnetic energy on the direction of  $M$  with respect to the crystallographic axes. The microscopic origin of the magnetocrystalline anisotropy is the spin-orbit interaction, that links the spin and the orbit of an electron (hole), as has been explained in Section 2.4. The relationship between the spin-orbit interaction and the magnetocrystalline anisotropy can be qualitatively understood as follows. When, for instance, a magnetic field is used to change the orientation of the spin of an electron (hole), the orbit of that electron (hole) will also tend to change. But since the orbit of the electron (hole) is coupled to the lattice via the strong orbit-lattice interaction, it will resist the attempt of the magnetic field at reorienting the spin. Only if the magnetic field is strong enough to overcome the effect of the spin-orbit interaction or, in other words, the magnetocrystalline anisotropy energy, it will succeed in reorienting the spin of the electron (hole).

**Shape anisotropy** This kind of anisotropy is present in any non-spherical magnetic sample<sup>7</sup> and is due to the existence of demagnetizing fields. A demagnetizing field  $H_d$  is generated by the magnetic poles that form at the

---

<sup>6</sup>It is also possible to describe magnetic anisotropy in terms of an anisotropy field. This will be discussed in Section 3.3.1.

<sup>7</sup>It is here assumed that a sample is composed of a single magnetic domain. The concept of magnetic domains will be dealt with in the next Section.

physical boundaries of a ferromagnetic sample, where  $M$  suddenly stops, and always acts in the opposite direction to  $M$ , hence its name. While in a spherical sample  $H_d$  does not depend on the direction of  $M$ , for a long and thin planar sample (a film) it is much stronger when  $M$  lies perpendicular to the sample, i.e. along its short axis. Since the smallest  $H_d$  corresponds to the lowest energy configuration in the sample, shape anisotropy is generally responsible for  $M$  being preferentially aligned in the plane of a ferromagnetic film.

**Strain anisotropy** This kind of anisotropy is present in any ferromagnetic sample that experiences an anisotropic mechanical stress and is due to the existence of the magnetoelastic coupling, i.e. the connection between the magnetic and elastic properties of a magnetic material. The magnetoelastic energy of a magnetic sample<sup>8</sup> under an applied stress  $\sigma$  can be written as:

$$E = \frac{3}{2}\lambda\sigma \sin^2 \xi, \quad (2.2)$$

where  $\lambda$  is the magnetoelastic coefficient and  $\xi$  is the angle between  $M$  and  $\sigma$ . The magnetoelastic anisotropy constant associated with a stress  $\sigma$  can then be expressed as  $K_\sigma = \frac{3}{2}\lambda\sigma$ . The microscopic origin of the magnetoelastic coupling is, once more, the spin-orbit interaction. As a consequence of the magnetoelastic coupling, when a magnetic field is used to change the direction of  $M$  in a ferromagnetic sample its dimensions change. This effects is known as magnetostriction. Accordingly, inverse magnetostriction (also known as Villari effect) consists in the variation of the magnetic properties of a ferromagnetic sample when a mechanical stress is applied to it. If this stress is anisotropic, then the magnetic properties will be varied anisotropically.

The complex scenario of the magnetic anisotropy in (Ga,Mn)As is governed by an interplay among magnetocrystalline, shape and strain anisotropies. Shape anisotropy is proportional to  $M^2$  and given that  $M$  is quite small in (Ga,Mn)As (typically a few tens of emu/cm<sup>3</sup>), shape anisotropy is often much weaker than magnetocrystalline and strain anisotropies and can thus usually be neglected. Strain anisotropy instead plays a crucial role in (Ga,Mn)As, whether the strain is in-built due to growth on lattice-mismatched substrates or is induced by external sources. As mentioned in Section 2.2, the lattice constant of relaxed (Ga,Mn)As is larger than the lattice constant of GaAs [31], especially if Mn<sub>I</sub> and As<sub>Ga</sub> impurities are present [58]. As a consequence, (Ga,Mn)As layers grown on GaAs substrates are under in-plane compressive strain. This circumstance normally

---

<sup>8</sup>See footnote 7.

induces the easy axis to lie in the plane of (Ga,Mn)As, as it has been proven both experimentally [31, 39] and theoretically [70, 71]. On the other hand, (Ga,Mn)As layers that are under in-plane tensile strain, as when grown on relaxed (Ga,In)As buffer layers or when co-doped with enough phosphorus<sup>9</sup>, are normally characterized by a perpendicular-to-plane easy axis. The magnetocrystalline anisotropy provides a cubic contribution to the overall magnetic anisotropy of (Ga,Mn)As, which derives from the cubic symmetry of its zinc-blende crystal structure.

If the [001] is the (Ga,Mn)As growth direction, as for the samples used in this Thesis, then the magnetocrystalline anisotropy gives rise to three equivalent easy axes along the [100], [010] and [001] directions. The in-built growth strain though, which acts along the [001] direction, breaks the cubic symmetry and, as explained above, originates either an easy plane perpendicular to the [001] direction (usually for compressive strain) or an easy axis along the [001] direction (usually for tensile strain). When the former situation takes place, it would be reasonable to think that the magnetic anisotropy landscape in the easy plane of (Ga,Mn)As is entirely governed by the in-plane biaxial contribution of the magnetocrystalline anisotropy, that would provide two equivalent easy axes along the [100] and [010] directions. But this is not the case, since it is found experimentally that the in-plane biaxial anisotropy is in competition with an in-plane uniaxial anisotropy that breaks the in-plane symmetry and yields an easy axis along the  $[1\bar{1}0]$  direction [72, 73]. Even if the origin of this uniaxial anisotropy is still controversially discussed, with some works ascribing it to preferential Mn incorporation induced by surface reconstruction during growth [74], to the presence of surface ripples [75] or of stacking faults defects [76], it can nonetheless be easily modelled via an in-plane shear strain [77]. Taking into account the competition between biaxial and uniaxial contributions, the anisotropy energy of a single-domain (Ga,Mn)As sample with in-plane easy axis can be phenomenologically expressed as [78]:

$$E_a = -\frac{K_C}{4} \sin^2 2\theta + K_U \sin^2 \theta, \quad (2.3)$$

where  $K_C > 0$  and  $K_U > 0$  are the lowest-order biaxial and uniaxial magnetic anisotropy constants, respectively, and  $\theta$  is the angle that  $M$  forms with the  $[1\bar{1}0]$  direction. As can be seen by taking the derivative of Eq. 2.3 with respect to  $\theta$ , its first and second term yield minima for  $\theta = \pm\pi/4$  and  $\theta = 0$ , thus reproducing the easy axes orientations expected for the biaxial and uniaxial anisotropy, respectively. According to Eq. 2.3, for  $K_U \geq K_C$  the sample will have one easy axis along the  $[1\bar{1}0]$  direction, while for  $K_U < K_C$  two easy axes will be present, with orientations given by  $\theta = 1/2 \cdot \arccos(K_U/K_C)$ . Then, in the

---

<sup>9</sup>The properties of (Ga,Mn)As co-doped with phosphorus, i.e. (Ga,Mn)(As,P), will be discussed in detail in Chapter 4.

limit of  $K_C \gg K_U$ , the two easy axes will lie along the [100] and [010] directions. It is usually found that the biaxial anisotropy prevails at low temperatures [78]. However, since  $K_U$  and  $K_C$  scale with the magnetization roughly as  $M^2$  and  $M^4$ , respectively [78, 79], and given that  $M$  decreases with increasing temperature, the dominant magnetic anisotropy often changes from biaxial to uniaxial with increasing temperature [78].

Being mainly induced by spin-orbit interaction, the magnetic anisotropy in (Ga,Mn)As depends strongly on the hole concentration [71], that has not been taken into account yet in this discussion. Then, for instance, (Ga,Mn)As layers under in-plane compressive (tensile) strain can exhibit a perpendicular-to-plane (in-plane) easy axis (axes) provided their hole concentration is sufficiently low [73]. Moreover, since the hole concentration can be greatly increased by post-growth annealing, there can be significant differences in the magnetic anisotropy of as-grown and annealed samples. A rotation of the easy axis from the  $[1\bar{1}0]$  direction to the [110] direction upon annealing has indeed been observed [80].

To simplify the notation, from now onwards samples characterized by in-plane and perpendicular-to-plane magnetic easy axis (axes) will be referred to as samples with in-plane and perpendicular magnetic anisotropy, respectively.

#### **2.5.4 Magnetic domains**

A magnetic domain is a region of a ferromagnetic material in which all the magnetic moments are aligned along the same easy axis direction. Hence  $M$  is saturated within each domain. Since the direction of the alignment of  $M$  varies from domain to domain, a multi-domain ferromagnetic material might not exhibit a spontaneous  $M$  below its  $T_C$ . The regions separating adjacent magnetic domains are called domain walls. Within a domain wall  $M$  has to change direction from one domain easy axis to the neighbouring domain easy axis. The angle between these two easy axis directions is used to classify domain walls: a  $180^\circ$  domain wall separates domains with opposite  $M$ , while a  $90^\circ$  domain wall separates domains with perpendicular  $M$ .  $180^\circ$  domain walls can be further divided into two categories, depending on the relative orientation between the rotation plane of  $M$  and the plane of the wall, this being parallel and perpendicular for Bloch and Néel domain walls, respectively.

The reason for the existence of magnetic domains is that their formation reduces the energy associated with demagnetizing fields. On the other hand, each created domain costs energy because of the presence of domain walls. So, the size of a domain is determined by the competition between the cost of demagnetizing fields and the cost of domain walls. The fact that a domain wall costs energy is due to the exchange energy associated with pairs of non-parallel neighbouring

magnetic moments<sup>10</sup> and to the magnetocrystalline anisotropy energy associated with magnetic moments lying away from the easy axes. Incidentally, while the former favours wide domain walls to minimize the angle between adjacent magnetic moments, the latter favours narrow domain walls to reduce the number of magnetic moments pointing in non-easy directions. Hence, not only the size of magnetic domains, but also the size of domain walls is the result of a trade-off between two competing processes.

Knowing the domain configuration of a sample is necessary to understand the mechanisms through which its magnetization changes upon application of an external magnetic field  $H$ . When  $H$  is applied to a multi-domain ferromagnetic sample that is initially demagnetized,  $M$  can vary from 0 to its saturation value  $M_S$ , along the direction of  $H$ , through one or more of the following processes: domain wall motion, in which domains possessing a magnetic moment already aligned with  $H$  grow at the expense of the other domains; non-coherent domain rotation, through which the magnetic moment of non-aligned domains suddenly switches towards the easy axis closest to the direction of  $H$ ; and coherent domain rotation, in which the magnetic moment of non-aligned domains coherently rotates towards the direction of  $H$ . In a single-domain ferromagnetic sample, given the absence of domain walls, only domain rotation processes have to be considered. In this case, once the contribution of the magnetic anisotropy is known, the dependence of  $M$  on  $H$  can be obtained using the Stoner-Wohlfarth model [81]. For  $H$  applied perpendicular to the easy axis (axes), domain rotation is a reversible process, meaning that the same  $M$  vs  $H$  curve is followed for both increasing (from  $-M_S$  to  $+M_S$ ) and decreasing (from  $+M_S$  to  $-M_S$ )  $H$ . For all the other  $H$  directions domain rotation is an irreversible process, with associated open  $M$  vs  $H$  loops, also called hysteresis loops. Domain wall motion is always an irreversible process, because of the unavoidable presence of defects or strains in the sample, by which the domain wall can be pinned. Further details about magnetic domains, domain walls and magnetization processes can be found in [68, 69].

As for most ferromagnetic materials with macroscopic dimensions, magnetic domains are present also in layers of (Ga,Mn)As and play an important role in its magnetization processes. Stripe-shaped magnetic domains a few  $\mu\text{m}$  wide have been observed in layers of tensile-strained (Ga,Mn)As with perpendicular magnetic anisotropy [82]. Compressively-strained (Ga,Mn)As layers with in-plane magnetic anisotropy are instead characterized by much larger magnetic domains, with sizes reaching hundreds of  $\mu\text{m}$  [83]. Indeed, when very high crystalline quality is achieved in these layers, samples as large as a few square millimetres

---

<sup>10</sup>The exchange energy between two neighbouring magnetic moments  $\mathbf{m}_1$  and  $\mathbf{m}_2$  is proportional to  $-\mathbf{m}_1 \cdot \mathbf{m}_2$ .

can be in a single-domain state, as it has been proven by showing that their magnetic behaviour can be mostly explained using the single-domain Stoner-Wohlfarth model [78]. Nonetheless, for values of  $H$  close to switching processes, domain dynamics cannot be neglected.

## 2.6 Transport properties

(Ga,Mn)As layers can exhibit insulating or metallic behaviour depending on the Mn concentration and the compensation level [32, 49, 84]. At low Mn concentrations the band occupied by the holes in (Ga,Mn)As, called impurity band, is narrow and separated from the valence band by an energy gap of magnitude similar to the impurity binding energy  $E_b$ , i.e.  $\sim 0.1$  eV. These dilute (Ga,Mn)As layers are insulating. Metallic behaviour appears in (Ga,Mn)As for larger Mn concentrations, when the broadened impurity band merges with the valence band [49, 85] and the holes become delocalized. The insulator-to-metal transition typically occurs for Mn concentrations  $\gtrsim 1.5\%$  [47], when also a transition from paramagnetic to ferromagnetic behaviour occurs, as described in Section 2.3. This circumstance is a signature of the carrier-mediated nature of ferromagnetism in (Ga,Mn)As. When suffering from high levels of charge compensation, even (Ga,Mn)As layers with Mn concentrations  $> 1.5\%$  can be insulating. This is due to the fact that, because of compensation, the merged impurity-valence band is only partially filled and the holes remain localized [84]. Post-growth annealing can be used in these (Ga,Mn)As layers to remove the charge compensating defects and make them metallic [54].

The temperature dependence of the electrical resistivity  $\rho$  is very different in the two transport regimes of (Ga,Mn)As. For insulating samples  $\rho$  increases monotonically with decreasing  $T$ . For metallic samples the initial increase of  $\rho$  for decreasing  $T$  is followed by a peak, then by a sharp decrease, and sometimes by a further increase for temperatures less than a few K. This critical behaviour in the dependence of  $\rho$  on  $T$  for metallic (Ga,Mn)As is commonly observed in ferromagnetic metals and semiconductors and is due to a decreased effectiveness of the scattering of carriers by spin fluctuations when the material enters the ferromagnetic state, i.e. when its spins start aligning along the easy axis (axes) [32]. This explains why the peak in  $\rho$  vs  $T$  roughly occurs for  $T = T_C$ . Indeed it has been shown that, even when the peak in  $\rho$  vs  $T$  is quite broad, a clear cusp for  $T = T_C$  is present in the temperature derivative of the resistivity  $d\rho/dT$  [86]. The increase of  $\rho$  that can occur at very low temperatures is the result of a quantum effect, known as weak localization [87]. Post-growth low-temperature annealing always results in a reduction of  $\rho$ , and this reduction is found to be larger at lower temperatures. Moreover, the annealing procedure has the effect of broadening the

peak in  $\rho$  vs  $T$  and moving it to higher temperatures [54].

Carefully annealed (Ga,Mn)As layers with nominal Mn concentrations ranging from 4.5% to 12.5% exhibit metallic behaviour with corresponding  $\rho$  values going from  $\sim 4.6 \times 10^{-5}$  to  $\sim 2.3 \times 10^{-5}$   $\Omega\text{m}$  at room temperature and from  $\sim 3.5 \times 10^{-5}$  to  $\sim 1.7 \times 10^{-5}$   $\Omega\text{m}$  at 4.2 K [86].

## 2.7 Magnetotransport properties

### 2.7.1 Ordinary magnetotransport properties

The transport properties of any conductive material change in the presence of a magnetic field  $\mathbf{B}$ , since this acts on the carriers via the Lorentz force  $\mathbf{F} = q(\mathbf{v} \times \mathbf{B})$ , where  $q$  is the carrier charge and  $\mathbf{v}$  is the carrier velocity, thus deviating their trajectories. The effects of a magnetic field on the transport properties of a material define the ordinary magnetotransport properties of this material, which manifest themselves in the ordinary magnetoresistance effect and the ordinary Hall effect [69]. Symmetry considerations prove that the former is an even function of  $\mathbf{B}$  while the latter is an odd function of  $\mathbf{B}$  [88].

#### Ordinary magnetoresistance effect

The ordinary magnetoresistance effect results in the dependence of the electrical resistance of a material on the magnitude and direction of  $\mathbf{B}$ . As it may be expected, the resistance increases with increasing  $B$ . This increase is normally found to be proportional to  $B^2$ , although it can be a more complicated function of  $B$  at low temperatures and/or high magnetic fields [88]. Moreover, the resistivity measured for  $\mathbf{B}$  perpendicular to the current direction, is always found to be larger than the resistivity measured for  $\mathbf{B}$  parallel to the current direction. This anisotropy arises from the non-spherical shape of the Fermi surface

#### Ordinary Hall effect

Considering the geometry in which the current flows in the plane of a thin film, the ordinary Hall effect (OHE) results in the appearance of an electric voltage in the in-plane direction perpendicular to the current direction, when an external magnetic field is applied perpendicular to the film [89]. The transverse resistance

$R_{xy}$ <sup>11</sup> due to the OHE is given by:

$$R_{xy} \equiv \frac{\rho_{xy}}{d} = R_O B \cos \alpha, \quad (2.4)$$

where  $d$  is the thickness of the film,  $R_O$  is the ordinary Hall coefficient and  $\alpha$  is the angle formed by the magnetic field with the direction perpendicular to the film plane. Since  $R_O = 1/nqd$ , where  $n$  is the carrier concentration and  $q$  is the carrier charge, the OHE can be used to determine the carrier concentration of a material.

### 2.7.2 Extraordinary magnetotransport properties

In ferromagnetic materials the ordinary magnetotransport effects are overlaid by the typically much larger extraordinary magnetotransport effects, which arise from the spin-orbit interaction: when the magnetization rotates, the electron cloud around each nucleus deforms, thus changing the amount of scattering undergone by the carriers. So, as the ordinary magnetotransport phenomena describe the influence of a magnetic field on the transport properties of a generic material, the extraordinary magnetotransport phenomena describe how these properties in a ferromagnet are influenced by the magnetization. There are two distinct extraordinary magnetotransport effects: the anisotropic magnetoresistance and the anomalous Hall effect, which are the analogues of their ordinary counterparts.

#### Anisotropic magnetoresistance

The anisotropic magnetoresistance (AMR) is the dependence of the electrical resistance of a ferromagnet on the orientation of the magnetization with respect to the current direction and the crystallographic axes. The AMR was discovered in 1857 by Thomson (Lord Kelvin), who found that in iron and nickel the resistivity is smaller when  $\mathbf{M}$  is perpendicular to the current direction than when  $\mathbf{M}$  is parallel to it, i.e.  $\rho_{xx}(\mathbf{M} \perp \mathbf{I}) < \rho_{xx}(\mathbf{M} \parallel \mathbf{I})$  [7], which is often found to be the case for ferromagnetic metals [88].

Due to the broken cubic symmetry of (Ga,Mn)As layers grown on lattice-mismatched substrates, the AMR in (Ga,Mn)As is described with two coefficients [90]:

$$\text{AMR}_{\text{op}} = \frac{\rho_{xx}(\mathbf{M} \parallel \hat{x}) - \rho_{xx}(\mathbf{M} \parallel \hat{z})}{\rho_{xx}(\mathbf{M} \parallel \hat{z})}, \quad (2.5)$$

$$\text{AMR}_{\text{ip}} = \frac{\rho_{xx}(\mathbf{M} \parallel \hat{x}) - \rho_{xx}(\mathbf{M} \parallel \hat{y})}{\rho_{xx}(\mathbf{M} \parallel \hat{y})}, \quad (2.6)$$

---

<sup>11</sup>If  $x$  is the direction of the current in the  $x$ - $y$  plane, then  $R_{xx}$  ( $\rho_{xx} \equiv \rho$  of Section 2.6) and  $R_{xy}$  ( $\rho_{xy}$ ) are the notations used to refer to the longitudinal and transverse resistance (resistivity), respectively, i.e. the resistance (resistivity) measured along the direction of the current, and along the direction perpendicular to it.

where  $\hat{x}$  is the direction of the in-plane current and  $\hat{z}$  is the growth direction. The subscripts “op” and “ip” stand for out-of-plane and in-plane, respectively. Thus, the AMR in (Ga,Mn)As is influenced by the in-built growth strain in a similar way as the magnetic anisotropy is, which may be expected since they both originate from the spin-orbit interaction. It is experimentally found that the  $\text{AMR}_{\text{op}}$  and  $\text{AMR}_{\text{ip}}$  coefficients are negative in (Ga,Mn)As, which means that the configuration in which  $\mathbf{M}$  and  $\mathbf{I}$  are parallel is characterized by the lowest resistance, as opposed to the vast majority of ferromagnetic metals. Moreover, it can be shown that  $|\text{AMR}_{\text{op}}| > |\text{AMR}_{\text{ip}}|$  for compressively strained layers, while  $|\text{AMR}_{\text{op}}| < |\text{AMR}_{\text{ip}}|$  for tensile strained layers [90, 91]. The  $\text{AMR}_{\text{op}}$  and  $\text{AMR}_{\text{ip}}$  coefficients in (Ga,Mn)As have typical values of a few % at low temperatures [87, 90, 91] and they are found to decrease with increasing the Mn concentration and with post-growth annealing [91].

The remainder of this Section will focus on the  $\text{AMR}_{\text{ip}}$  coefficient, which will now be referred to as AMR. To simplify the notation,  $\rho_{xx}(\mathbf{M} \parallel \hat{x})$  and  $\rho_{xx}(\mathbf{M} \parallel \hat{y})$  will be called  $\rho_{\parallel}$  and  $\rho_{\perp}$ , respectively, so that  $\text{AMR} = (\rho_{\parallel} - \rho_{\perp})/\rho_{\perp}$ . In addition, it will be assumed that  $\mathbf{M}$  is saturated along the direction of  $\mathbf{B}$ . In the coordinate system defined by the magnetization direction and its orthogonal direction the resistivity tensor is given by:

$$\rho = \begin{pmatrix} \rho_{\parallel} & 0 \\ 0 & \rho_{\perp} \end{pmatrix}. \quad (2.7)$$

Hence, the resistivity tensor in the coordinate system defined by the current direction  $x$ , which lies at an angle  $\phi$  to the magnetization direction, and its orthogonal direction  $y$ , can be obtained as:

$$\begin{aligned} \rho &\equiv \begin{pmatrix} \rho_{xx} & \rho_{xy} \\ \rho_{yx} & \rho_{yy} \end{pmatrix} = \begin{pmatrix} \cos \phi & -\sin \phi \\ \sin \phi & \cos \phi \end{pmatrix} \begin{pmatrix} \rho_{\parallel} & 0 \\ 0 & \rho_{\perp} \end{pmatrix} \begin{pmatrix} \cos \phi & \sin \phi \\ -\sin \phi & \cos \phi \end{pmatrix} = \\ &= \begin{pmatrix} \bar{\rho} + \frac{1}{2}\Delta\rho \cos 2\phi & \frac{1}{2}\Delta\rho \sin 2\phi \\ \frac{1}{2}\Delta\rho \sin 2\phi & \bar{\rho} - \frac{1}{2}\Delta\rho \cos 2\phi \end{pmatrix}, \end{aligned} \quad (2.8)$$

where  $\bar{\rho} = (\rho_{\parallel} + \rho_{\perp})/2$  and  $\Delta\rho = \rho_{\parallel} - \rho_{\perp}$ . It follows that, if the AMR in (Ga,Mn)As would depend just upon the relative orientation between magnetization and current, the longitudinal and transverse resistivity would be phenomenologically described as:

$$\begin{aligned} \rho_{xx} &= \bar{\rho} + \frac{1}{2}\Delta\rho \cos 2\phi, \\ \rho_{xy} &= \frac{1}{2}\Delta\rho \sin 2\phi. \end{aligned} \quad (2.9)$$

However, the AMR in (Ga,Mn)As also depends on the relative orientation between magnetization and crystallographic axes, as it has been pointed out in distinguishing between the  $\text{AMR}_{\text{ip}}$  and  $\text{AMR}_{\text{op}}$  coefficients. This crystalline contribution to the AMR is the transport analogue of the magnetocrystalline contribution to the magnetic anisotropy. The phenomenological description of the crystalline component of the AMR in (Ga,Mn)As is obtained adapting, through symmetry considerations, the standard phenomenology used for cubic crystals [92] to the case of crystals with cubic and uniaxial anisotropy. Following this procedure the total longitudinal AMR in (Ga,Mn)As can be written as [93]:

$$\frac{\Delta\rho_{xx}}{\rho_{av}} = C_I \cos 2\phi + C_U \cos 2\psi + C_C \cos 4\psi + C_{I,C} \cos(4\psi - 2\phi), \quad (2.10)$$

where  $\Delta\rho_{xx} = \rho_{xx} - \rho_{av}$ ,  $\rho_{av}$  is  $\rho_{xx}$  averaged over  $360^\circ$  in the plane of the film,  $\phi$ , as above, is the angle between  $\mathbf{M}$  and  $\mathbf{I}$  and  $\psi$  is the angle between  $\mathbf{M}$  and the [110] crystal direction. The four contributions in Eq. 2.10 are the non-crystalline term  $C_I$ , the lowest-order uniaxial  $C_U$  and cubic  $C_C$  crystalline terms and a crossed non-crystalline/crystalline term  $C_{I,C}$ . For symmetry reasons the purely crystalline terms are excluded from the expression of the transverse AMR, which then turns out to be [93]:

$$\frac{\rho_{xy}}{\rho_{av}} = C_I \sin 2\phi - C_{I,C} \sin(4\psi - 2\phi). \quad (2.11)$$

Usually the non-crystalline term represents the dominant contribution ( $\sim 90\%$ ) to the AMR in (Ga,Mn)As [93], leading to the lowest resistance for the configuration in which  $\mathbf{M}$  and  $\mathbf{I}$  are parallel, as anticipated above. For ultra thin (Ga,Mn)As layers, i.e.  $\sim 5$  nm, the situation is very different, with the crystalline terms dominating and the uniaxial one being the largest [93]. Independently of the layer thickness, however, the crystalline components of the AMR depend on temperature in a similar way as the magnetic anisotropy does. So, for instance, standard-thickness (Ga,Mn)As layers are characterized by the cubic and uniaxial term prevailing at low and high temperatures, respectively, while ultra-thin (Ga,Mn)As layers show dominating uniaxial AMR over the whole temperature range [93].

The spin-orbit dependent mechanisms responsible for the origin of the non-crystalline and crystalline components of the AMR in (Ga,Mn)As are described in detail in [93].

As with its ordinary analogue, the AMR is an even function of  $\mathbf{M}$ , meaning that  $\Delta\rho_{xx}(\mathbf{M}) = \Delta\rho_{xx}(-\mathbf{M})$  and  $\rho_{xy}(\mathbf{M}) = \rho_{xy}(-\mathbf{M})$ .

Finally, it is worth mentioning an additional magnetoresistance effect in (Ga,-Mn)As. At large fields, a negative isotropic magnetoresistance (IMR) can be

always observed below  $T_C$ . The IMR can be very large for low conductive layers [90] and becomes weaker after post-growth annealing [91]. The dependence of the IMR on  $B$  is not well defined but it can normally be considered as linear for  $B$  varying in a small range. It was initially suggested that the IMR could be due to the suppression of spin disorder that occurs for  $T < T_C$ , which also accounts for the critical behaviour observed in  $\rho$  vs  $T$ , as described in Section 2.6. However, if this consideration can justify the presence of the negative IMR for temperatures just below  $T_C$ , it fails to explain why the IMR does not saturate at low temperatures, where the local spins are almost fully aligned, even when magnetic fields larger than 20 T are applied [94]. It has then been proposed that the IMR at low temperatures could be described in terms of the suppression of the weak localization [90].

### **Anomalous Hall effect**

If a current is flowing in the plane of a ferromagnetic layer, an electric voltage can appear in the in-plane direction perpendicular to the current direction even without an applied  $\mathbf{B}$ , provided  $\mathbf{M}$  has a non-zero component along the direction perpendicular to the layer. This is known as the spontaneous or anomalous Hall effect (AHE). The transverse resistance  $R_{xy}$  due to the AHE is given by:

$$R_{xy} \equiv \frac{\rho_{xy}}{d} = R_S M \cos \beta, \quad (2.12)$$

where the geometric configuration and the notations used are the same as in Eq. 2.4,  $R_S$  is the anomalous Hall coefficient and  $\beta$  is the angle formed by the magnetization with the direction perpendicular to the film plane. The AHE arises from the spin-orbit interaction which induces anisotropy in the scattering mechanisms undergone by spin-up and spin-down carriers [88]. In particular, “skew” and “side-jump” scattering mechanisms predict  $R_S \propto \rho_{xx}$  and  $R_S \propto \rho_{xx}^2$ , respectively [95]. Further theoretical investigations have suggested that the dominant contribution to the AHE in (Ga,Mn)As may actually stem from a scattering-independent topological mechanism, which also predicts  $R_S \propto \rho_{xx}^2$  [96]. While an unambiguous description of the relative influence of the various microscopic mechanisms that could give rise to the AHE in (Ga,Mn)As has not been provided yet, the available experimental results are mostly consistent with  $R_S \propto \rho_{xx}^2$  [97].

In ferromagnetic materials, (Ga,Mn)As included, the AHE is normally much larger than the OHE, i.e.  $R_S \gg R_O$ . This circumstance, together with the uncertain dependence of  $R_S$  on  $\rho_{xx}$ , makes it quite hard to extract the hole concentration from  $R_O$  in (Ga,Mn)As [97, 54]: for typical hole and Mn concentrations the error in the evaluation of the hole concentration from the AHE can be as high as 20% [98].

On the other hand, since  $R_S \gg R_O$  and  $\rho_{xx}$  is usually weakly dependent on  $B$ , the functional form of  $\rho_{xy}(B)$  does closely follow that of  $M(B)$ , at least at low fields. The AHE then provides a useful tool to measure hysteresis loops without using magnetometry techniques. While  $R_O$  is temperature independent,  $R_S$ , being dependent on  $\rho_{xx}$ , is strongly influenced by temperature changes [97].

As with its ordinary analogue, the AHE is an odd function of  $\mathbf{M}$ , meaning that  $\rho_{xy}(\mathbf{M}) = -\rho_{xy}(-\mathbf{M})$ .

# Chapter 3

## Materials and experimental methods

### 3.1 Materials

The materials used for the experiments described in this Thesis are high-quality single-crystal films of (Ga,Mn)As and (Ga,Mn)(As,P). They are enumerated in Tab. 3.1, together with their specifications and key magnetic properties.

Wafer No.	Mn (%)	P (%)	$d$ (nm)	Annealing	$M_S$ (emu/cm <sup>3</sup> )	$T_C$ (K)	Anisotropy
Mn403	6	10	25	No	23.2	29	In-plane
	6	10	25	Yes	43.8	110	Perpendicular
Mn437	12	0	25	No	51.1	76	In-plane
	12	0	25	Yes	71.5	181	In-plane
Mn491	6	6	25	No	29.6	52	In-plane
	6	6	25	Yes	40.5	122	In-plane
Mn492	6	3	25	No	30.9	61	In-plane
	6	3	25	Yes	38.4	125	In-plane
Mn498	6	9	25	No	28.6	47	In-plane
	6	9	25	Yes	33.8	109	Perpendicular
Mn591	6	9	100	No	26.5	51	In-plane
	6	9	100	Yes	37.9	110	Perpendicular

Table 3.1: List of the materials used in the experiments described in this Thesis. The nominal Mn and P concentrations, the film thickness  $d$ , the saturation magnetization  $M_S$ , the Curie temperature  $T_C$  and the orientation of the easy axis (axes) are provided for each material in both its as-grown and annealed state (see text for details).

The films were grown by Dr. Richard P. Campion via LT-MBE with As dimers on semi-insulating 350  $\mu\text{m}$  thick GaAs(001) wafers using the Veeco Modular GEN-III MBE system of the University of Nottingham. A buffer layer of

Ga(As,P) for Mn403 or GaAs for all the other wafers was grown between the substrate and the magnetic film. The magnetic films were grown at a temperature of  $\sim 230$  °C, apart from Mn437 that was grown at a temperature of  $\sim 200$  °C.

Each material was characterized both in the as-grown and annealed state, as shown in Tab. 3.1. It is here intended that an annealed material has undergone a full post-growth annealing procedure or, in other words, that no further variation of its transport and magnetic properties can be observed upon further annealing. The time necessary to fully anneal a material depends on its thickness and on the chosen annealing temperature, being longer for thicker materials and lower annealing temperatures [55]. It has been shown that annealing at lower temperatures results in better magnetic properties [43], but this is often impractical for thick materials because highly time consuming. The 25 nm thick films listed in Tab. 3.1 were annealed at 180 °C for 48 hours, while the 100 nm thick film Mn591 was annealed at 200 °C for roughly a week. Annealing was always performed in air.

## 3.2 Sample fabrication

In order to investigate the magnetic, transport and magnetotransport properties of a material it is necessary to shape it in a configuration suitable for the chosen type of measurement<sup>1</sup>. For magnetometry measurements this simply requires to cut the wafer into small rectangular pieces, typically of  $4 \times 5$  mm<sup>2</sup>, which is quickly accomplished using a scribing machine with a diamond tip. The cleavage directions are the [110] and the [1 $\bar{1}$ 0] for both (Ga,Mn)As and (Ga,Mn)(As,P) wafers. For transport and magnetotransport measurements the material has usually to be patterned into a more complex shape, which requires the use of lithography fabrication techniques. In a general sense lithography is any procedure that uses selective chemical processes to write on a material. Depending on the required resolution, different lithography techniques can be used for sample fabrication. When the size of the smallest feature that needs to be patterned is in the  $\mu\text{m}$  range, as for all the samples measured in this Thesis, then photolithography is an adequate choice.

Standard photolithography procedures involve following a number of sequential steps that are here briefly described. At first the wafer is chemically cleaned, normally using solvents in an ultrasonic bath, in order to remove any debris or contamination from its surface. Then the wafer surface is covered with a uniform layer of photoresist, a light-sensitive material, usually a few hundreds of  $\mu\text{m}$  thick. This is achieved rotating the wafer at high speed in order to spread the photoresist by centrifugal force, a technique known as spin coating. Next the wafer is

<sup>1</sup>Apart from imaging measurements.

baked in an oven or on an hotplate to eliminate the excess solvent present in the photoresist. Now the wafer is ready to be irradiated with light, a process that causes the chemical properties of the photoresist to change. In particular, positive (negative) photoresist that is exposed to high-intensity UV light becomes soluble (insoluble) in a specific solution, known as developer. Hence the photoresist can be patterned into the desired geometry if it is selectively exposed to light. This is achieved interposing a photomask, i.e. a glass plate covered with a patterned metal film, between the UV light source and the wafer. Since the UV light is absorbed by the metal film and let through by the rest of the photomask, the pattern is transferred from the photomask to the photoresist. Once developed, the photoresist is left to cover just selected regions of the wafer surface. At this point specific chemical treatments, to which the photoresist is mostly immune, are used to remove those regions of the wafer surface that are not covered by the photoresist, thus allowing the pattern to be engraved into the material. At the end of this process, known as etching, the photoresist is no longer needed and is dissolved, typically using acetone. If electrical measurements need to be performed, then further processing is required to deposit metal contacts on the patterned wafer. So, following the same steps described above, the photoresist is spin-coated and patterned again, although in a different geometry. The selected metal is then evaporated on the wafer surface under high vacuum conditions, until a sufficiently thick film of it is formed. When next the photoresist is dissolved in acetone, the metal film deposited on top of it is lifted-off and removed together with the photoresist. Metal thus remains just in those regions where it is in direct contact with the wafer and might be later annealed to favour its partial diffusion into the wafer. The patterned wafer is now finally provided with metal contacts and the fabrication process is over. Before the measurement can start though, the processed sample has to be glued onto a suitable header and electrically connected to its pins via bond wires.

All the samples used for the transport and magnetotransport measurements presented in this Thesis have been fabricated according to the standard photolithography procedures described above and mounted on non-magnetic headers. Particular care has been taken in avoiding, or at least minimizing, those processing steps that require the use of high temperatures, in order to prevent accidental annealing of the materials. Two different geometries have been used for the patterning: they are the Hall bar and the Corbino disk sketched in Fig. 3.1 (a) and (b), respectively.

In the Hall bar geometry the current flows across the 45  $\mu\text{m}$  wide channel and the voltage is measured via the six 20  $\mu\text{m}$  wide probes that are separated from each other by 295  $\mu\text{m}$ . In the Corbino disk geometry the current flows radially across the 7  $\mu\text{m}$  wide annulus. The yellow regions of Fig. 3.1 represent

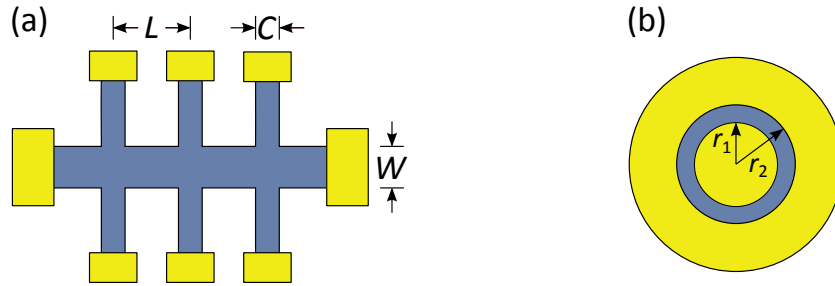


Figure 3.1: Sketch of the Hall bar (a) and Corbino disk (b) geometries patterned on the wafers measured in this Thesis. The relevant dimensions for the Hall bar geometry are  $L = 295 \mu\text{m}$ ,  $C = 20 \mu\text{m}$  and  $W = 45 \mu\text{m}$ , while for the Corbino disk geometry they are  $r_1 = 90 \mu\text{m}$  and  $r_2 = 97 \mu\text{m}$ . The yellow regions represent the metal contacts.

the metal contacts, that were obtained evaporating on the wafers a  $\sim 30 \text{ nm}$  Ti layer followed by a  $\sim 150 \text{ nm}$  Au layer. The Ti layer improves the adhesion of the metal to the wafer, thus allowing for ohmic contacts to be realized.

The samples measured in Chapter 5 and Chapter 6 underwent some further minor fabrication steps, whose description will be given in the Chapters themselves.

### 3.3 Measuring instruments and procedures

#### 3.3.1 SQUID magnetometer

##### System description

A Superconducting Quantum Interference Device (SQUID) magnetometer is among the most sensitive instruments used for measuring magnetic fields and, as such, it is often chosen to study the magnetic properties of thin films containing diluted magnetic moments like (Ga,Mn)As. The SQUID is the detection system of a SQUID magnetometer and consists of a closed superconducting loop containing one or two Josephson junctions, in the case of radio frequency (RF) or direct current (DC) SQUID, respectively. The extraordinary sensitivity of the SQUID derives from the highly non-linear  $I$ - $V$  characteristic of the Josephson junction and the quantized nature of the magnetic flux through it.

All the magnetometry measurements described throughout this Thesis were carried out using the Quantum Design MPMS-XL SQUID magnetometer of the School of Physics and Astronomy in the University of Nottingham. This SQUID magnetometer has always been used with the reciprocating sample measurement option, which allows to detect magnetic moments as small as  $10^{-9} \text{ emu}$ , according to manufacturer specifications. In the MPMS-XL magnetometer the RF SQUID

is coupled via superconducting wires to a system of superconducting coils, known as detection coils. When a sample is moved through the detection coils, its magnetic moment causes a change in the magnetic flux through them, which in turn induces a change in the persistent electric current flowing across the whole superconducting loop, including the SQUID. The magnetic moment of the sample is then determined measuring the change in the SQUID output voltage. Hence the SQUID of the MPMS–XL magnetometer does not directly measure the magnetic moment of the sample, but is essentially used as a current-to-voltage converter. For the measurement to be accurate, both the SQUID and the detection coils need to be protected from ambient magnetic field fluctuations and from the large magnetic fields generated by the superconducting magnet. This is achieved placing the SQUID in a region of constant (and small) magnetic field enclosed by a superconducting shield and shaping the detection coils in a second-order gradiometer configuration which consists of three equally spaced coils, the outer ones wound clockwise in a single turn and the middle one wound anticlockwise in a double turn, and grants a high insensitivity to magnetic noise.

The sample is mounted, at times glued on a silver wire, in a clear drinking straw that is connected to the end of the sample rod. During the measurement the rod is moved through the detection coils, i.e. along the axis of the gradiometer, via a stepper motor and the SQUID voltage is measured a number of times at various positions over the specified scan length. The spatial dependence of the SQUID voltage thus obtained is then automatically fitted by the Quantum Design software to provide the magnetic moment of the sample. Independently on the fitting routine chosen, it is in any case assumed that the sample behaves like an ideal point-form magnetic dipole. This strong assumption imposes the sample to be much smaller than the detecting gradiometer and uniformly magnetized. In practice, if wanting to maintain the error associated with the fitting within 3%, the dimension of the sample along the scan direction should not exceed 5 mm [99]. In the opposite limit, samples longer than the gradiometer will not be detected during a scan and this is the reason why long uniform objects can safely be used for mounting purposes.

The superconducting magnet used in this SQUID magnetometer generates magnetic fields up to 1 T along the axis of the gradiometer and, according to manufacturer specifications, is uniform up to 99.99% over a 4 cm length. The temperature can be accurately set to any value within the range 1.9 – 400 K.

### **Measurements description**

In this Thesis the MPMS–XL SQUID magnetometer has been used to measure the dependence of the magnetization  $M$  of (Ga,Mn)As and (Ga,Mn)(As,P) samples, typically shaped in rectangular pieces of  $4 \times 5 \text{ mm}^2$ , upon temperature  $T$  and

magnetic field  $H$ .

The  $M$  vs  $T$  magnetometry measurements were performed following these steps. The sample was at first mounted in the straw according to the chosen measurement direction and then was cooled from room temperature down to 2 K under a magnetic field of 1000 Oe, large enough to saturate the magnetization along its direction. At  $T = 2$  K the field was removed<sup>2</sup>, allowing the magnetization to rotate towards the closest easy axis direction. The component of the magnetization along the field direction for zero applied field, known as remanent magnetization and denoted as  $M_R$ , was then measured while raising the temperature from 2 K to a value greater than  $T_C$ , usually with a rate of 1 K per minute. This procedure was then repeated for all the necessary directions so that a set of  $M_R$  vs  $T$  curves was finally obtained. A large amount of information on the magnetic properties of (Ga,Mn)As and (Ga,Mn)(As,P) samples is contained in such a set of measurements. Firstly, by comparing the values of  $M_R$  along the different directions it is possible to determine the dominant magnetic anisotropy contribution and establish whether the sample is characterized by perpendicular or in-plane magnetic anisotropy and, in the latter case, whether the uniaxial anisotropy prevails over the cubic, or vice-versa. Secondly, the Curie temperature  $T_C$  can be easily identified as the temperature at which  $M_R$  along a non-hard-axis direction goes to zero. Thirdly, for samples in a single-domain state, the saturation magnetization  $M_S$  can be determined as:

$$M_S = \sqrt{M_{[1\bar{1}0]}^2 + M_{[110]}^2 + M_{[001]}^2}, \quad (3.1)$$

where  $M_{[1\bar{1}0]}$ ,  $M_{[110]}$  and  $M_{[001]}$  are the remanent magnetizations along the  $[1\bar{1}0]$ ,  $[110]$  and  $[001]$  directions, respectively. For samples with in-plane magnetic anisotropy just the first two terms in Eq. 3.1 are necessary and they can be replaced by analogous terms involving  $M_{[100]}$  and  $M_{[010]}$  when the uniaxial anisotropy dominates over the cubic. Vice-versa, just the third term in Eq. 3.1 is necessary for samples with perpendicular magnetic anisotropy. Finally, for single-domain samples with in-plane magnetic anisotropy the orientation of the easy axis (axes) can be determined as:

$$\theta = \arctan \left( \frac{M_{[110]}}{M_{[1\bar{1}0]}} \right), \quad (3.2)$$

where, as usually,  $\theta$  is the angle that  $M_S$  forms with the  $[1\bar{1}0]$  direction. Since for  $K_U < K_C$ , as discussed in Section 2.5.3,  $\theta$  is proportional to  $\arccos(K_U/K_C)$ , then these magnetometry measurements also allow to evaluate the ratio between the uniaxial  $K_U$  and cubic  $K_C$  magnetic anisotropy constants when the latter

---

<sup>2</sup>The magnetic field trapped in the superconducting magnet after having been discharged from 1000 Oe is less than 1 Oe.

prevails over the former.

The  $M$  vs  $H$  magnetometry measurements were performed at a constant temperature and consisted in measuring the sample magnetization while sweeping the magnetic field from positive saturating values to negative saturating values and back. The resulting  $M$  vs  $H$  loop thus yielded the component of the magnetization along the field direction for the various field values and the two sweeping directions. As above, by mounting the sample in different ways and repeating the measurements for each of them a set of  $M$  vs  $H$  loops was finally obtained. A point worth noticing is that, unlike remanence measurements that are carried out in zero magnetic field, these magnetometry measurements are always affected by the presence of a strong field-dependent diamagnetic contribution, stemming mainly from the thick GaAs substrate, that is easily identified by the “tilted” shape of the loops. This contribution is quantified by linearly fitting those regions of the  $M$  vs  $H$  loop for which  $M > M_S$  or  $M < -M_S$  and hence can be subtracted from the raw data. This subtraction is the main reason why extracting  $M_S$  from measurements of  $M$  vs  $H$  loops could be less accurate than from remanence measurements. The  $M$  vs  $H$  magnetometry measurements are instead useful to determine the anisotropy fields<sup>3</sup>, i.e. those magnetic fields at which the magnetization is saturated along their direction (possibly corrected for the presence of the shape anisotropy), and the coercive fields  $H_c$ , i.e. those magnetic fields at which  $M = 0$ . Moreover, the shape of the loop can provide information on the magnetic anisotropy since open squared loops, for which  $M_R \sim M_S$ , are associated to easy axis directions while closed loops, for which  $M_R \sim 0$ , are associated with hard axis directions. Finally, it is possible to extract the value of the individual magnetic anisotropy constants by fitting the  $M$  vs  $H$  loops with an expression derived from the Stoner-Wohlfarth single-domain model [81]. The magnetic energy of single-domain samples with in-plane magnetic anisotropy can be phenomenologically expressed as [78]:

$$E = -\frac{K_C}{4} \sin^2 2\theta + K_U \sin^2 \theta - M_S H \cos(\gamma - \theta), \quad (3.3)$$

where the first two terms represent the magnetic anisotropy energy and were introduced in Eq. 2.3, while the last term is the field-dependent Zeeman energy term.  $\theta$  and  $\gamma$  are the angles formed by  $M_S$  and  $H$ , respectively, with the  $[1\bar{1}0]$  direction. The fitting expression linking  $M$  and  $H$  is analytically found for  $H$  along easy or hard axes directions by taking the derivative of Eq. 3.3 with respect

---

<sup>3</sup>The magnetic anisotropy of a sample exerts a torque on the magnetic moments that are not aligned along the easy axis (axes) in the same way as a magnetic field exerts a torque on the magnetic moments that are not aligned along its direction. For this reason it is possible to associate an anisotropy field  $H_K \sim K/M_S$  to a magnetic anisotropy characterized by the magnetic anisotropy constant  $K$ .

to  $\theta$ . For all the other directions of  $H$  the fitting has to proceed numerically. In both cases Eq. 2.3 can be used to extract the values of  $K_U$  and  $K_C$  for single-domain samples with in-plane magnetic anisotropy.

### **3.3.2 Transport and magnetotransport equipment**

#### **System description**

All the transport and most of the magnetotransport measurements described throughout this Thesis were carried out using the Oxford Instruments He-4 Variox cryostat of the School of Physics and Astronomy in the University of Nottingham<sup>4</sup>. The sample is mounted at the end of the sample rod which is inserted into the sample space of the cryostat. The sample space is cooled down allowing liquid helium to pass through a needle valve from the helium reservoir to the heat exchanger surrounding the sample space. Temperatures as low as 1.5 K can be obtained by decreasing the pressure of the helium gas filling the sample space through a rotatory pump. The heat exchanger is equipped with a heater and a Cernox temperature sensor. The temperature controller Oxford Instruments ITC503, which balances the helium flow through the needle valve and the power dissipated in the heater, allows to achieve temperature stabilities of  $\pm 0.1$  K for temperatures greater than 4.2 K, according to manufacturer specifications. The Cernox temperature sensor can be used to measure the sample temperature but the temperature sensor fitted to the sample holder of some of the sample rods provides increased accuracy. The cryostat is used in conjunction with an external water-cooled rotating electromagnet surrounding the sample space. This electromagnet can generate magnetic fields up to 0.6 T along any direction parallel to the laboratory floor. Using different sample rod configurations is then possible to work with magnetic fields perpendicular to the sample or along any direction in its plane. Keithley digital sourcemeters and digital multimeters controlled by a LabVIEW interface are used to bias the sample and measure its electric properties.

#### **Measurements description**

With the exception again of the magnetotransport measurements presented in Chapter 6, all the transport and magnetotransport measurements in this Thesis have been performed on the Hall bars fabricated according to the procedure illustrated in Section 3.2. The notations and polarity conventions chosen for four terminal transport and magnetotransport measurements are shown in Fig. 3.2.

---

<sup>4</sup>A different equipment was used to perform the magnetotransport measurements presented in Chapter 6, but its description will be given in the Chapter itself for convenience.

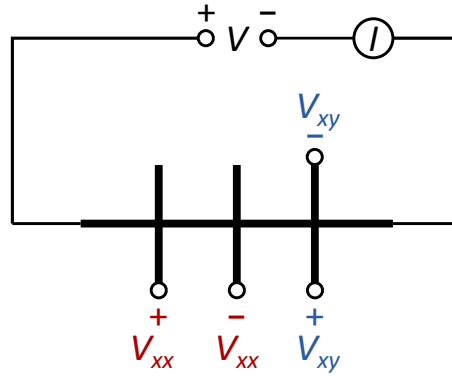


Figure 3.2: Notations and polarity conventions used for the four terminal transport and magnetotransport measurements described in this Thesis.  $V$  is the bias voltage,  $I$  is the current that flows across the Hall bar,  $V_{xx}$  and  $V_{xy}$  are the longitudinal and transverse voltages, respectively.

Four terminal transport measurements were performed in zero magnetic field by biasing the Hall bar with 1 V and measuring the longitudinal voltage  $V_{xx}$  while cooling the Hall bar from room temperature down to 1.5 K, usually at a rate of  $\sim 0.1$  K per second. The longitudinal resistance is calculated as  $R_{xx} = V_{xx}/I$ . Since the dimensions of the Hall bar are known, the longitudinal resistivity  $\rho_{xx}$  is easily derived from  $R_{xx}$ . Besides providing information on the quality of the wafer, transport measurements are a simple way to roughly identify the Curie temperature. In fact, as explained in Section 2.3, the temperature at which  $d\rho_{xx}/dT$  shows a singularity is a good approximation of the Curie temperature [86].

Four terminal magnetotransport measurements were performed at constant temperature by biasing the Hall bar with 1 V as above, and measuring the longitudinal  $V_{xx}$  and transverse  $V_{xy}$  voltages while either varying the intensity of the magnetic field or its direction. When the magnetic field is applied along the perpendicular-to-plane direction the transverse resistance  $R_{xy}$ , which is calculated as  $V_{xy}/I$ , provides information on the component of the magnetization along the field direction, since it is proportional to it via the AHE coefficient (see Eq. 2.12). When instead the magnetic field is applied in the plane of the sample,  $R_{xx}$  and  $R_{xy}$  provide information about the longitudinal and transverse AMR, respectively, and can then be used to extract the value of various AMR coefficients:  $C_I, C_U, C_C$  and  $C_{I,C}$  (see Eq. 2.10 and Eq. 2.11).

### 3.3.3 Magneto-optical Kerr effect imaging equipment

#### System description

The magneto-optical Kerr effect (MOKE) consists in the rotation of the plane of polarization of a linearly polarized light beam upon reflection from a mag-

netized material. This effect is a consequence of the spin-orbit interaction and can be qualitatively understood as follows. Right-handed and left-handed circularly polarized light incident on a material cause its carriers to rotate in the corresponding senses, each providing a contribution to the orbital angular momentum  $\mathbf{L}$  of equal magnitude but opposite sign. Since a magnetic field induces the spins of the carriers to be polarized along its direction, the spin-orbit interaction modifies the energy associated with the two polarizations in opposite ways. The magnetized material will then respond with different refractive indices to the two polarizations. Hence, when a linearly polarized light beam is reflected from a magnetized material, given that it can be considered as the superposition of right-handed and left-handed circularly polarized light beams, its plane of polarization will be rotated because the two polarizations will be phase-delayed with respect to each other. Since the rotation of the plane of polarization is proportional to the magnetization, the MOKE can be used to study magnetic properties of materials and, in particular, to image magnetic domains. The MOKE can be performed with  $\mathbf{M}$  perpendicular to the sample plane (polar configuration) or with  $\mathbf{M}$  parallel to the sample plane and parallel (longitudinal configuration) or perpendicular (transverse configuration) to the incidence plane of the light beam. Being stronger than the in-plane MOKE [100], the polar MOKE is more often used in experiments.

The MOKE imaging presented in this Thesis was carried out using the MOKE microscope of the Hitachi laboratory in the University of Cambridge. This system combines an Oxford Instruments MicroStatHiRes2 optical cryostat with a Neoark BH-7850CS Domain Observation Device. In this continuous-He-flow cryostat cooling is achieved by constantly pumping liquid helium from an helium storage dewar along a transfer tube to the heat exchanger, on top of which the sample is placed. The minimum temperature achievable is  $\sim 4.2$  K. The heat exchanger is fitted with a heater and a temperature sensor, used to measure the temperature of the sample. As for the cryostat described in the previous Section, good temperature control is achieved balancing the helium flow and the power dissipated in the heater via the Oxford Instruments ITC503 temperature controller. The Neoark equipment includes a microscope, fitted with an high-pressure 100 W mercury lamp and a  $\times 20$  magnifying lens, an high-resolution 800,000 pixel CCD camera and two polarisers. Light from the lamp is linearly polarized passing through the first polariser and, after being reflected from the sample, eventual changes in its polarisation plane are detected as changes in its intensity after exiting the second polariser. Once the light reaches the CCD camera the information it contains is converted into an image. The spatial resolution achieved is 1  $\mu\text{m}$ . The system is equipped with Helmholtz coils, able to generate magnetic fields up to 200 mT and 50 mT for polar and in-plane configurations, respectively.

### **Measurements description**

In this Thesis the MOKE microscope was used to image the magnetic domain structure of sample Mn591 at a constant temperature of 4.2 K and for a specific value of the magnetic field.

# Chapter 4

## Properties of (Ga,Mn)(As,P)

### 4.1 Introduction

Most of the research on III–V DMS has been devoted to the study of (Ga,Mn)As but robust hole-mediated ferromagnetism, which is the most remarkable aspect of these systems, has been observed also in other (III,Mn)V DMS. This circumstance has led researchers to investigate the possibility of alloying GaAs with different III–V semiconductors in order to achieve an “optimal” Mn-doped DMS with a Curie temperature higher than (Ga,Mn)As. GaP, in particular, has been suggested as a good candidate for this purpose [101]. Indeed, the fact that GaP has a smaller lattice constant than GaAs indicates that the exchange interaction acting between holes and local magnetic moments in (Ga,Mn)As might be stronger when P atoms substitute for As atoms. On the other hand, GaP has a wider energy band gap than GaAs which results in the holes in (Ga,Mn)P being more strongly localized than in (Ga,Mn)As and therefore less effective at mediating the exchange interaction. The consequences of the interplay between these two competing effects on the properties of (Ga,Mn)(As,P) have been investigated both theoretically and experimentally.

A theoretical work based on the double exchange model of ferromagnetism<sup>1</sup> predicted a small, almost-linear, decrease of  $T_C$  upon increasing the P concentration [102], whereas a different theoretical study based on the indirect exchange model of ferromagnetism predicted an increase in  $T_C$  up to a factor of  $\simeq 1.5$  with increasing the P concentration [103]. Moreover, according to the latter study, (Ga,Mn)(As,P) should show a significantly weaker tendency to incorporate interstitial Mn atoms during growth than (Ga,Mn)As, as a consequence of the reduced size of the interstitial space. Due to the different models of ferromagnetism used in the two studies it might be reasonable to think that they would

---

<sup>1</sup>This model is typically used to describe the onset of ferromagnetism in III–V DMS systems with carriers localized in a narrow impurity band, as for (Ga,Mn)As with low Mn concentration or wider band gap semiconductors.

be more appropriate for higher and lower P concentrations, respectively.

Preliminary experiments performed on (Ga,Mn)(As,P) samples synthesized using the combination of ion implantation and pulsed-laser melting showed a decrease of  $T_C$  by roughly a factor of 2 and a correspondent metal-to-insulator transition upon increasing the P concentration from 0 to just 3.1% [104, 105]. This result was attributed by the authors to alloy-disorder scattering of the holes in the impurity band, but was later explained as a consequence of the presence of various defects introduced by the growth method [106]. As a matter of fact, (Ga,Mn)(As,P) samples grown via LT-MBE were found to have much better magnetic and transport properties, despite still showing a modest decrease of  $T_C$  with increasing the P concentration [107]. In any case, independently of the growth method, the predicted enhancement of  $T_C$  in (Ga,Mn)(As,P) samples [103] was not observed experimentally, suggesting that the effects of the increased hole localization on the magnetic properties of these samples overcome those due to the increased exchange interaction. Despite these unsuccessful results regarding  $T_C$ , studies on (Ga,Mn)(As,P) have revealed a different interesting property of this material, that of being characterized by perpendicular magnetic anisotropy for large enough P concentrations [104, 107, 108].

Magnetic materials with perpendicular anisotropy are advantageous in data recording technologies because they allow for much higher storage densities than magnetic materials with in-plane anisotropy [109]. Perpendicular magnetic anisotropy has also been shown to be favourable over in-plane magnetic anisotropy in experiments of current-induced domain wall motion, given that it enables to reduce the critical current density needed to trigger the motion of domain walls [110, 111]. Furthermore, perpendicular magnetic anisotropy is convenient from an experimental point of view since it allows to detect the orientation of the magnetization via anomalous Hall effect and polar MOKE. For a long time perpendicular magnetic anisotropy was obtained in (Ga,Mn)As samples grown on relaxed (Ga,In)As buffer layers in turn grown on GaAs(001) substrates [31, 39, 70]. In fact, as explained in Chapter 2, growing (Ga,Mn)As on relaxed (Ga,In)As results in the former being under in-plane tensile strain, a circumstance that induces perpendicular magnetic anisotropy for large enough hole concentrations [71]. However it was found that the strain relaxation in (Ga,In)As occurs via the formation of a high density of dislocations which thread through to the (Ga,Mn)As layer on top and lead to high coercive fields and strong pinning of domain walls [112, 113]. Whereas, given that P atoms are smaller than As atoms, in-plane tensile strain, and consequently perpendicular magnetic anisotropy, can be achieved in (Ga,Mn)(As,P) samples without the need of relaxed buffer layers. The resulting much lower density of defects in these samples leads to smaller coercive fields, thus allowing for easier switching of the magnetization to be possible,

and a reduced number of pinning centres, so that domain wall motion can take place at smaller current densities and in a wider range of temperatures compared to (Ga,Mn)As samples grown on (Ga,In)As [114, 115].

This Chapter presents the results of structural, magnetometry, transport and magnetotransport measurements performed on a series of (Ga,Mn)(As,P) samples with different P concentrations, both as-grown and annealed. In particular, it will be shown how the magnetic anisotropy in (Ga,Mn)(As,P) samples can be controlled upon varying the P concentration, the temperature and the annealing time. Similar or complementary investigations have been carried out in numerous other experimental works [107, 108, 116, 117, 118]. Most of the results discussed in this Chapter were published in [119].

## 4.2 Growth

The 25 nm thick  $(\text{Ga}_{1-x},\text{Mn}_x)(\text{As}_{1-y},\text{P}_y)$  layers used to perform the investigations contained in this Chapter are Mn403, Mn491, Mn492 and Mn498, with nominal Mn concentration  $x = 6\%$  and nominal P concentration  $y = 10\%, 6\%, 3\%$  and  $9\%$ , respectively (see Tab. 3.1). They were grown at a temperature of  $\sim 230^\circ\text{C}$  on buffer layers and semi-insulating GaAs(001) substrates, using LT-MBE with As dimers, as in standard (Ga,Mn)As growth. The incorporation of phosphorus in the desired amount was achieved reducing the  $\text{As}_2$  flux from the stoichiometry condition by that amount and then evaporating phosphorus with a beam equivalent pressure (BEP) slightly in excess of it [107].

A 50 nm thick buffer layer of  $\text{Ga}(\text{As}_{0.9},\text{P}_{0.1})$  for Mn403 and GaAs for Mn491, Mn492 and Mn498 was grown before the corresponding magnetic layer at a temperature of  $\sim 230^\circ\text{C}$  and  $\sim 580^\circ\text{C}$ , respectively. The choice of growing a low temperature buffer layer was initially made to ensure a good temperature stability during the growth of the magnetic layer, but improvements in the growth technique later allowed this to be possible also via growing a high temperature buffer layer, which is desirable to hinder the formation of defects. This would then suggest that Mn491, Mn492 and Mn498 should be characterized by better crystal quality and magnetic properties than Mn403. No significant difference should instead be present in the in-plane strain experienced by the magnetic layers since the  $\text{Ga}(\text{As}_{0.9},\text{P}_{0.1})$  buffer layer is not relaxed and therefore its in-plane lattice constant  $a_{\parallel}$  is equal to that of GaAs.

For both Mn403 and the Mn491–Mn492–Mn498 series, control samples without phosphorus were grown on GaAs buffer layers, in exactly the same conditions as the corresponding phosphide samples.

### 4.3 In-built growth strain

GaP crystallizes in the zinc-blende structure with a smaller lattice constant than GaAs. Hence Ga(As,P) also has a smaller lattice constant than GaAs. On the other hand, (Ga,Mn)As has a larger lattice constant than GaAs, due to the presence of both substitutional and interstitial Mn atoms [58], as explained in Section 2.2, and is therefore under in-plane compressive strain when grown on GaAs. It is then crucial to know how many P atoms, for a given Mn concentration, have to substitute for As atoms in order to grow (Ga,Mn)(As,P) layers on GaAs under in-plane tensile strain. According to the empirical Vegard's law, the relaxed lattice constant of  $(\text{Ga}_{1-x}, \text{Mn}_x)(\text{As}_{1-y}, \text{P}_y)$  can be determined as:

$$a_{(\text{Ga}_{1-x}, \text{Mn}_x)(\text{As}_{1-y}, \text{P}_y)} = (1 - x_s)(1 - y) \cdot a_{\text{GaAs}} + (1 - x_s)y \cdot a_{\text{GaP}} + x_s(1 - y) \cdot a_{\text{MnAs}} + x_sy \cdot a_{\text{MnP}}, \quad (4.1)$$

where  $x_s$  is the substitutional Mn concentration corresponding to the nominal Mn concentration  $x$ , and  $a_{\text{AB}}$  is the lattice constant of the AB compound in the zinc-blende structure. In the literature it can be easily found that  $a_{\text{GaAs}} = 5.65325 \text{ \AA}$  and  $a_{\text{GaP}} = 5.4505 \text{ \AA}$ . Assuming once more the validity of Vegard's law,  $a_{\text{MnAs}}$  can be derived extrapolating the lattice constant of (Ga,Mn)As samples with known Mn concentration, measured with XRD [120], and  $a_{\text{MnP}}$  can be calculated from  $a_{\text{GaP}}$ , using the same gradient obtained for the  $\text{GaAs} \rightarrow (\text{Ga,Mn})\text{As} \rightarrow \text{MnAs}$  extrapolation.  $a_{\text{MnAs}} = 5.95 \text{ \AA}$  and  $a_{\text{MnP}} = 5.7366 \text{ \AA}$  are thus obtained. Given that Eq. 4.1 does not take into account the effect of interstitial Mn atoms on the lattice constant, it should not be used for the as-grown samples. On the other hand, assuming that all interstitial Mn atoms are removed upon annealing and that  $x_s = 5\%$ , which is reasonable for  $x = 6\%$ , then Eq. 4.1 can be used to derive how the lattice constant of the annealed samples varies with  $y$ , which is plotted in Fig. 4.1. Looking at this figure, it can then be easily understood that Vegard's law predicts annealed  $(\text{Ga}_{0.94}, \text{Mn}_{0.06})(\text{As}_{1-y}, \text{P}_y)$  layers grown on GaAs to be under in-plane compressive (tensile) strain for P concentration smaller (larger) than 7.3%.

XRD measurements were performed using a Philips X'Pert Materials Research diffractometer by Dr. Nicola R. S. Farley and Dr. Peter Wadley on all (Ga,Mn)(As,P) samples and control samples, to accurately measure their perpendicular lattice constant  $a_{\perp}$  (since these samples are fully strained, their in-plane lattice constant  $a_{\parallel}$  is equal to that of GaAs) and establish the magnitude and sign of the in-built growth strain. XRD  $\omega - 2\theta$  scans at the GaAs (004) peak are shown for Mn403 and control sample in Fig. 4.2 and for the Mn491–Mn492–Mn498 series and control sample, in Fig. 4.3. All samples were measured both as-grown and annealed. In both figures, the sharp peaks represent the reflection

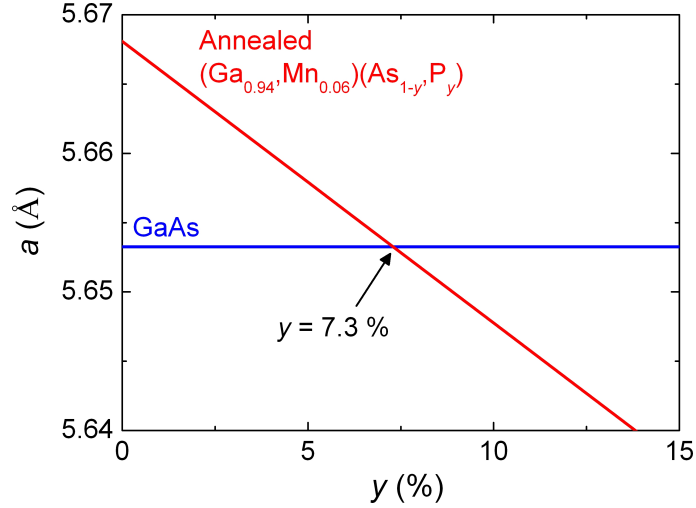


Figure 4.1: Lattice constant  $a$  of GaAs (blue) and annealed  $(\text{Ga}_{0.94}, \text{Mn}_{0.06})(\text{As}_{1-y}, \text{P}_y)$  (red) as a function of  $y$ . The latter is derived using Eq. 4.1 with  $x_s = 5\%$ . The two lattice constants match for  $y = 7.3\%$ .

from the GaAs substrates, while the broader peaks, marked with dashed vertical lines, represent the reflection from the magnetic layers. Unlike Fig. 4.3, in Fig. 4.2 it is not straightforward to visually distinguish the peak associated with the  $(\text{Ga},\text{Mn})(\text{As},\text{P})$  layer from the thickness fringes associated with the  $\text{Ga}(\text{As},\text{P})$  buffer layer, but the fitting procedure allows nonetheless to determine the former with good accuracy. Peaks located at lower (higher) angles than the sharp GaAs peaks are associated with magnetic layers under in-plane compressive (tensile) strain. Hence, the fact that the  $(\text{Ga},\text{Mn})(\text{As},\text{P})$  peak moves towards higher angles with increasing  $y$  indicates a corresponding decrease of  $a_{\perp}$ , as expected. Moreover, it is evident from both figures that  $a_{\perp}$  substantially decreases also upon annealing, due to the out diffusion of interstitial Mn atoms [58].

The experimental data were fitted using the Philips X'pert Smoothfit software to extract the values of the effective phosphorus concentration  $y_{eff}$  and  $a_{\perp}$  for each sample. This was done assuming that the concentration of substitutional and interstitial Mn atoms in Mn403 and the Mn491–Mn492–Mn498 series is the same as in the respective control samples. From the value of  $a_{\perp}$  is then easy to calculate the magnitude and sign of the in-built growth strain  $\epsilon$ :

$$\epsilon = \frac{a_{\perp} - a_{\text{GaAs}}}{a_{\text{GaAs}}}. \quad (4.2)$$

$y_{eff}$ ,  $a_{\perp}$  and  $\epsilon$  thus derived are listed in Tab. 4.1 for each sample, both as-grown and annealed. Overall,  $y_{eff}$  is in reasonable agreement with  $y$ , apart from the Mn492 sample where  $y_{eff}$  is almost twice as large as  $y$ . Concerning the values of  $a_{\perp}$  and  $\epsilon$ , all the annealed samples seem to be characterized by in-plane tensile

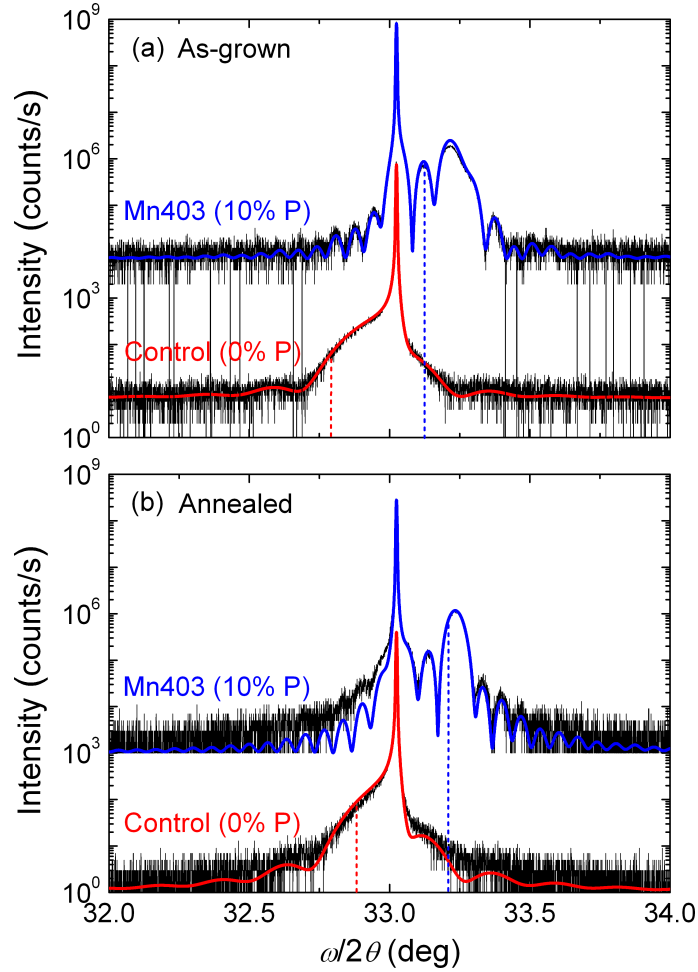


Figure 4.2: XRD  $\omega - 2\theta$  scans at the GaAs (004) peak for as-grown (a) and annealed (b) Mn403 and control sample. The black lines are the experimental data, while the solid coloured lines are their fittings: blue for Mn403 and red for the control sample. The dashed coloured lines mark the approximate position of the magnetic layers (004) reflection. The Mn403 data and fitting curve are vertically offset for clarity.

strain, according to these fitting results, which is in disagreement with what is predicted by Vegard's law in Fig. 4.1. Nonetheless, it is necessary to remark that values of  $x_s$  different from the 5% assumed in Fig. 4.1 were estimated for the control samples and thus used in the fitting procedures to derive the values of  $a_{\perp}$  and  $\epsilon$ .

## 4.4 SQUID magnetometry results

SQUID magnetometry measurements were performed on all  $(\text{Ga},\text{Mn})(\text{As},\text{P})$  samples and control samples to investigate their magnetic properties, in particular their magnetic anisotropy. These measurements were carried out using the magnetometry system described in Section 3.3.1 and following the procedures pre-

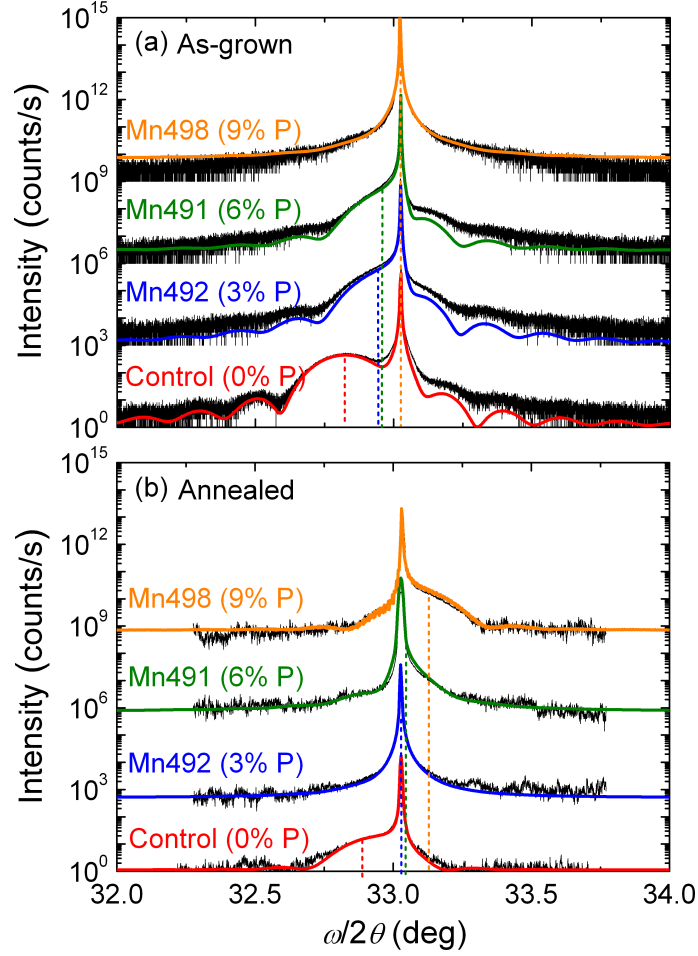


Figure 4.3: XRD  $\omega - 2\theta$  scans at the GaAs (004) peak for as-grown (a) and annealed (b) Mn491, Mn492, Mn498 and control sample. The black lines are the experimental data, while the solid coloured lines are their fittings: green, blue, orange and red for Mn491, Mn492, Mn498 and control sample, respectively. The dashed coloured lines mark the approximate position of the magnetic layers (004) reflection. The Mn491, Mn492 and Mn498 data and fitting curves are vertically offset for clarity, in order of increasing the P concentration.

sented there.

Fig. 4.4 shows  $M$  vs  $H$  loops measured at  $T = 2$  K for the as-grown and annealed samples, with  $H$  applied along in-plane and perpendicular-to-plane directions. These measurements show that all the as-grown samples are characterized by in-plane magnetic anisotropy at  $T = 2$  K, since the remanent magnetization  $M_R$  is large along the in-plane directions and almost zero along the perpendicular-to-plane direction<sup>2</sup> (Fig. 4.4 (a, c, e, g)). This is consistent with the sign of the in-plane strain extracted from XRD measurements for Mn492, Mn491 and Mn498 but might appear surprising for Mn403 that experiences a large in-plane tensile

<sup>2</sup>Even if the perpendicular-to-plane direction has not been measured for Mn492 and Mn491, it is nonetheless possible to establish that they have in-plane magnetic anisotropy from the  $M_R$  vs  $T$  measurements of Fig. 4.5, that will be described in the following.

Wafer No.	$y$ (%)	$y_{eff}$ (%)	Annealing	$a_{\perp}$ (Å)	$\epsilon$ (%)
Mn403	10	12.4	No	5.63742	-0.28
	10	12.4	Yes	5.62442	-0.51
Mn491	6	5.9	No	5.66569	0.22
	6	5.9	Yes	5.64986	-0.06
Mn492	3	5.5	No	5.66738	0.25
	3	5.5	Yes	5.65268	-0.01
Mn498	9	9.2	No	5.65325	0
	9	9.2	Yes	5.63629	-0.3

Table 4.1: Nominal  $y$  and effective  $y_{eff}$  phosphorus concentrations, perpendicular lattice constant  $a_{\perp}$  and strain  $\epsilon$  are listed for the different phosphide samples in both their as-grown and annealed state. A positive (negative) sign for  $\epsilon$  indicates in-plane compressive (tensile) strain.  $y_{eff}$  and  $a_{\perp}$  were extracted by fitting to the experimental XRD data.

strain according to XRD measurements. Nonetheless it must be remembered that the magnetic anisotropy depends not only on strain but also on hole concentration [71] which, as it will be shown in the next Section, is very low in this highly compensated as-grown sample.

The non-linear behaviour of  $M$  vs  $H$  in the [001] loop of Mn498 and Mn403, with two open sections at large values of  $|H|$  is caused by the competition between magnetocrystalline, strain and shape anisotropy: upon increasing  $|H|$ ,  $M$  reversibly rotates out of the plane until when it reaches an angle at which the magnetocrystalline anisotropy becomes dominant and leads to a sudden switch of  $M$  into the [001] direction. A similar behaviour for [001]  $M$  vs  $H$  loops has been previously observed in (Ga,Mn)As samples with low Mn concentration [121, 122].

Upon annealing the hole concentration increases, inducing the expected perpendicular magnetic anisotropy for all the samples, since they now are all under tensile-in-plane strain, as deduced from XRD results. A sign change in the strain anisotropy is indeed predicted in III–V DMS by the mean-field model of ferromagnetism based upon the Zener indirect exchange mechanism, for the hole concentration being increased above a certain threshold, typically  $\sim 10\%$  of  $x_{eff}$  [77], and has been experimentally observed in (Ga,Mn)As samples [73]. But, looking as above at the values of  $M_R$  along the different directions in Fig. 4.4, it is clear that just Mn498 and Mn403 are characterized by perpendicular magnetic anisotropy at  $T = 2$  K, while Mn492 and Mn491 still show in-plane magnetic anisotropy. For Mn492 this might be due to the fact that the sample is actually under in-plane compressive strain even after annealing: given the extremely small value of the strain extracted from XRD fittings it is not unreasonable to guess so. For Mn491 the same argument cannot apply since it is visually noticeable from Fig. 4.3 (b),

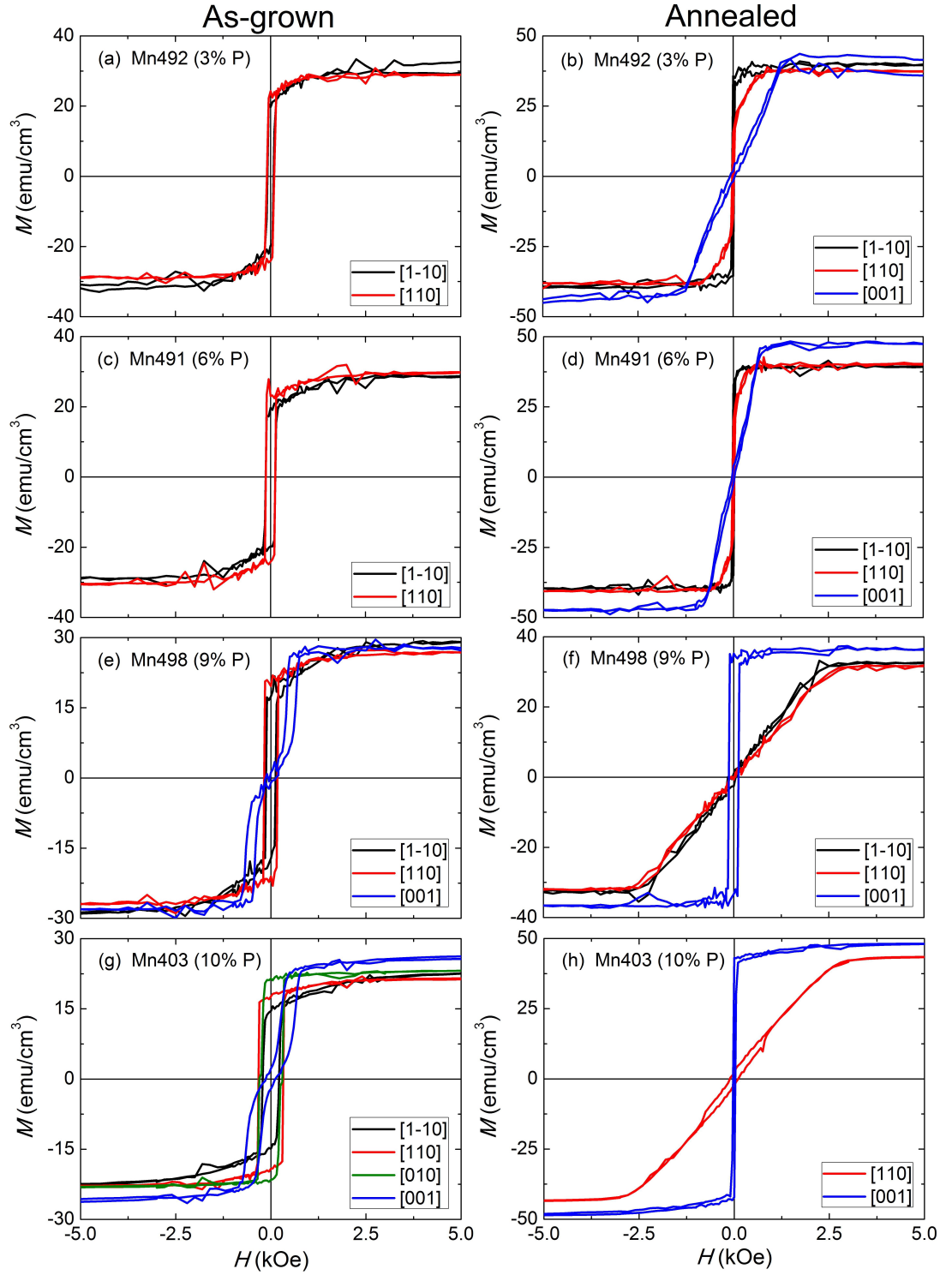


Figure 4.4:  $M$  vs  $H$  loops measured at  $T = 2$  K for the as-grown (a, c, e, g) and annealed (b, d, f, h) samples, with  $H$  applied along the in-plane  $[1\bar{1}0]$  (black),  $[110]$  (red) and  $[010]$  (green) directions and the perpendicular-to-plane  $[001]$  (blue) direction.

without the need of fitting to it, that the sample is indeed under in-plane tensile strain. The in-plane magnetic anisotropy for annealed Mn491 is difficult to ex-

plain, unless it is assumed that the small in-built growth strain experienced by the sample changes sign upon cooling from room temperature (where the XRD measurements were performed) down to 2 K.

The lowest-order strain-induced uniaxial perpendicular anisotropy field can be estimated as:  $H_{U\perp} = [M_S/(dM/dH)_{H=0} - H_d]$ , where  $(dM/dH)_{H=0}$  is the gradient of the M vs H loop around  $H = 0$ , while  $H_d = 4\pi M_S$  is the demagnetizing field due to the shape anisotropy. It is interesting to notice that, consistently with the variation of the in-plane strain across the annealed samples,  $H_{U\perp}$  increases upon increasing the P concentration, with  $H_{U\perp} = -981$  Oe,  $-271$  Oe,  $+3175$  Oe and  $+3530$  Oe for Mn492, Mn491, Mn498 and Mn403, respectively (a negative sign for  $H_{U\perp}$  has been used for the in-plane compressively strained samples). The fact that the coercive field  $H_c$  along the [001] direction is much larger in annealed Mn498 ( $H_c \sim 125$  Oe) than in annealed Mn403 ( $H_c \sim 30$  Oe) would suggest a larger number of pinning sites in the former, in disagreement with what could be expected from the different conditions used to grow the two wafers.

Finally, it is important to remark that the reason why loops measured with  $H$  applied along different directions show different values of  $M_S$  for the same sample (up to a factor of  $\sim 20\%$  for annealed Mn491) is probably just an artefact due to the point-form approximation used by the SQUID providing different results for different samples orientation with respect to the detection coils.

Fig. 4.5 shows  $M_R$  vs  $T$  curves measured for the as-grown and annealed samples, along in-plane and perpendicular-to-plane directions. These measurements confirm the sign of  $H_{U\perp}$  obtained from  $M$  vs  $H$  loops at  $T = 2$  K for all the samples, and moreover show that this sign does not change across the whole temperature range up to  $T_C$ .

For both as-grown and annealed samples  $T_C$  decreases upon increasing the P concentration, with a rate that is higher for as-grown than for annealed samples. The dependence of  $T_C$  on  $y_{eff}$  for as-grown and annealed samples is summarized for convenience in Fig. 4.6. The figure also shows the dependence of  $T_C/x_s$  on  $y_{eff}$  for the annealed samples, which is a more meaningful way to represent the effects of the P incorporation on  $T_C$ , since  $T_C$  is obviously affected also by the Mn concentration. Assuming that all interstitial Mn atoms are removed upon annealing,  $x_s$  is calculated for each sample using the value of  $M_S$  at  $T = 2$  K shown in Fig. 4.5 and the value of the magnetic moment per Mn atom obtained from XMCD measurements [118]. The decrease of  $T_C$  for the annealed samples upon increasing the P concentration is much more pronounced once the  $x_s$  correction is taken into account.

Finally, Fig. 4.5 is useful to examine how the uniaxial and cubic anisotropy terms compete in the samples with in-plane magnetic anisotropy.  $M_{[010]}$  vs  $T$  was measured just for as-grown Mn403 but can be easily derived for all the other sam-

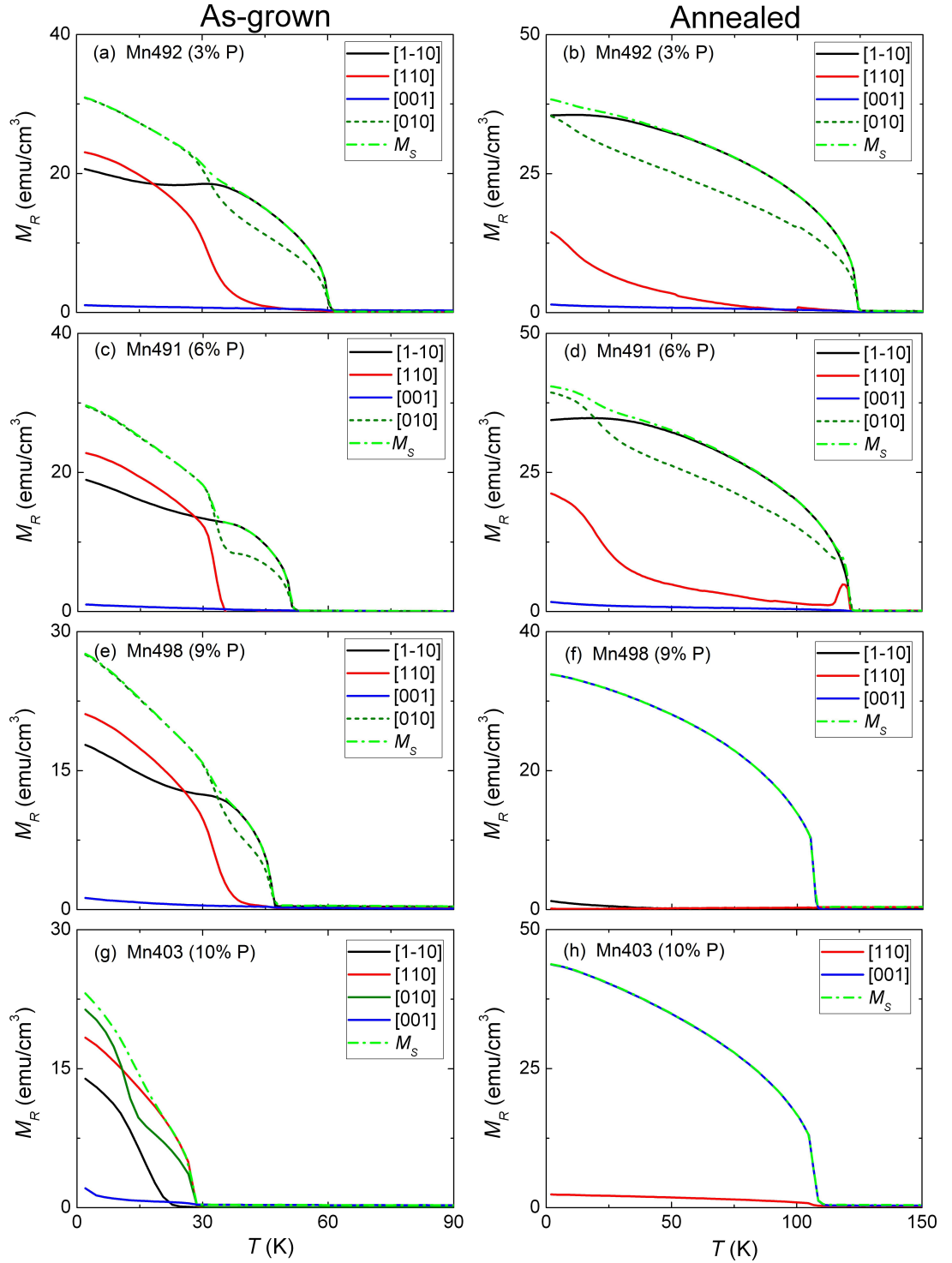


Figure 4.5:  $M_R$  vs  $T$  curves measured for the as-grown (a, c, e, g) and annealed (b, d, f, h) samples along the in-plane  $[1\bar{1}0]$  (black),  $[110]$  (red) and  $[010]$  (solid dark green) directions and the perpendicular-to-plane  $[001]$  (blue) direction. The saturation magnetization  $M_S$  (dashed light green) and the remanent magnetization  $M_{[010]}$  (dashed dark green) are calculated ( $M_{[010]}$  is measured just for as-grown Mn403) according to the Stoner-Wohlfarth single-domain model described in Sections 2.5.3 and 3.3.1.

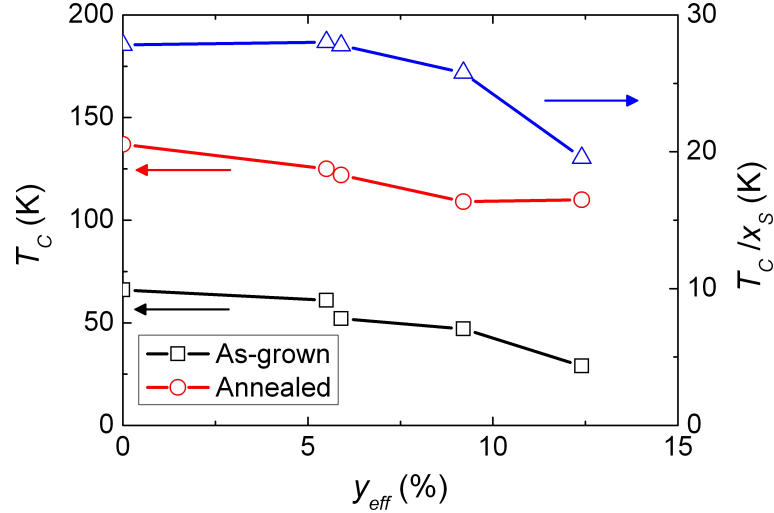


Figure 4.6:  $T_C$  vs  $y_{eff}$  for the as-grown (black squares) and the annealed (red circles) samples, and  $T_C/x_s$  vs  $y_{eff}$  for the annealed samples (blue triangles). Given the similarity between the properties of the two control samples, the data points for just one of them are shown.

ples with in-plane magnetic anisotropy using the Stoner-Wohlfarth single-domain model that has been described in Sections 2.5.3 and 3.3.1:  $M_{[010]} \equiv M_{[100]} = M_S \cdot \cos[\pi/4 - \arctan(M_{[110]}/M_{[1\bar{1}0]})]$ , where  $M_S$  is calculated according to Eq. 3.1. Both  $M_S$  vs  $T$  and  $M_{[010]}$  vs  $T$  thus derived are shown in Fig. 4.5 with dashed lines. Comparing the values of  $M_{[010]}$  with the values of  $M_{[1\bar{1}0]}$  and  $M_{[110]}$  it is evident that at low temperatures the cubic term prevails over the uniaxial term, with the easy axes lying generally closer to the cubic directions than to the uniaxial ones (apart from annealed Mn492, where the easy axes lie halfway between them), while the uniaxial term becomes dominant at higher temperatures. This is similar to what is commonly observed in  $(\text{Ga},\text{Mn})\text{As}$  samples, except for the fact that here, for the as-grown samples, the uniaxial term favours the  $[110]$  direction rather than the  $[1\bar{1}0]$ , at low temperatures. For the as-grown samples the  $[1\bar{1}0]$  uniaxial term becomes dominant upon increasing the temperature (apart from Mn403) while for the annealed samples the  $[1\bar{1}0]$  uniaxial term is dominant over the whole temperature range up to  $T_C$  (the fact that  $M_{[110]} \sim M_{[1\bar{1}0]}$  for annealed Mn491 at  $T \sim 120$  K is probably just a consequence of a small trapped magnetic flux in the SQUID superconducting magnet). A reorientation of the easy axis upon annealing between the two uniaxial directions has been previously observed in  $(\text{Ga},\text{Mn})\text{As}$  samples and ascribed to an increase in the hole concentration [80]. As explained in Section 3.3.1, the ratio between the uniaxial  $K_U$  and cubic  $K_C$  magnetic anisotropy constants can be derived, when the latter prevails over the former, as:  $K_U/K_C = \cos[2 \arctan(M_{[110]}/M_{[1\bar{1}0]})]$ . Fig. 4.7 shows the dependence of  $K_U/K_C$  on  $y_{eff}$  at  $T = 2$  K for all the samples characterized by in-plane

magnetic anisotropy. For the as-grown samples the ratio  $K_U/K_C$  increases in ab-

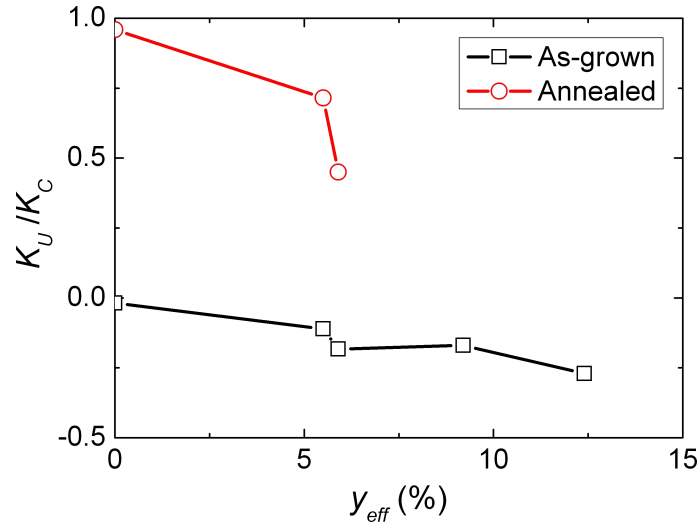


Figure 4.7:  $K_U/K_C$  vs  $y_{eff}$  for as-grown (black squares) and annealed (red circles) samples with in-plane magnetic anisotropy, at  $T = 2$  K. A negative sign in  $K_U$  indicates a preference for the  $[110]$  direction over the  $[1\bar{1}0]$  direction. Given the similarity between the properties of the two control samples, the data points for just one of them are shown.

solute value with increasing  $y_{eff}$ , while an opposite trend is observed for annealed samples.

## 4.5 Transport results

Four terminal transport measurements were performed on as-grown Mn498 and on as-grown, partially and fully annealed Mn403. These measurements were carried out using the transport system described in Section 3.3.2 and following the procedures presented there.

Fig. 4.8 shows the dependence of the longitudinal resistivity  $\rho_{xx}$  on temperature for as-grown Mn498 and Mn403. As it is immediately noticeable looking at the figure, the magnitude of  $\rho_{xx}$  is extremely different for the two samples, especially at low temperatures, where  $\rho_{xx}$  for Mn403 becomes almost four orders of magnitude larger than  $\rho_{xx}$  for Mn498. Also the behaviour of  $\rho_{xx}$  vs  $T$  is different for the two samples. In fact, while  $\rho_{xx}$  vs  $T$  is characterized by features typical of metallic ferromagnetic (Ga,Mn)As [32, 84] for Mn498, with  $\rho_{xx}$  initially increasing for decreasing  $T$  from above  $T_C$  and then decreasing as  $T$  is decreased below  $T_C$ , for Mn403  $\rho_{xx}$  increases monotonically with decreasing  $T$ , as usual for insulating samples<sup>3</sup>. For as-grown Mn491 and Mn492  $\rho_{xx}$  was measured just at room

<sup>3</sup>The large values of  $\rho_{xx}$  for as-grown Mn403, especially at low temperatures, are consistent with the sample being characterized by in-plane magnetic anisotropy despite being under in-

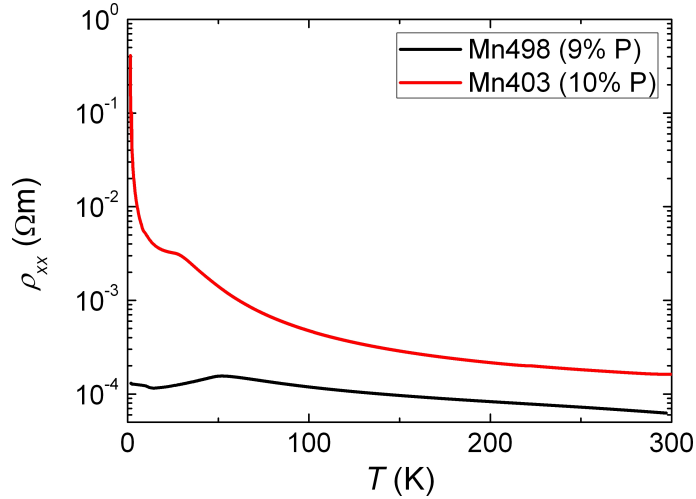


Figure 4.8:  $\rho_{xx}$  vs  $T$  curves for as-grown Mn498 and Mn403.

temperature and found to be similar to that of as-grown Mn498. The difference in both magnitude and behaviour of  $\rho_{xx}$  vs  $T$  observed in Fig. 4.8 could then be ascribed either to the different conditions used to grow the two samples or, more likely, to the occurrence of a metal-to-insulator transition for  $y_{\text{eff}} \gtrsim 9\% - 12\%$ . Moreover, it is worth noticing that the values of  $\rho_{xx}$  measured for as-grown Mn498 are not dissimilar to the values of  $\rho_{xx}$  typical of as-grown  $(\text{Ga},\text{Mn})\text{As}$  samples with the same nominal concentration [54], indicating that the incorporation of P in  $(\text{Ga},\text{Mn})\text{As}$  does not dramatically affect its transport properties for  $y_{\text{eff}} \lesssim 9\%$ .

Fig. 4.9 (a) shows the dependence of  $\rho_{xx}$  on  $T$  for Mn403 as-grown and annealed for increasing amounts of time at 180 °C.

Annealing results in a marked decrease in the magnitude of  $\rho_{xx}$  and in a transition towards a metallic temperature dependence. This is accompanied by an increase in  $T_C$ , as deduced from the position of the peak in  $d\rho_{xx}/dT$  [86], which is shown in Fig. 4.9 (b). These trends are consistent with the fact that annealing causes interstitial Mn atoms to be out diffused towards the surface, where they are then passivated by oxidation [55], leading to an increase in the hole concentration.

## 4.6 Magnetotransport results

Four terminal magnetotransport measurements were performed on as-grown Mn498 and on as-grown, partially and fully annealed Mn403. These measurements were carried out using the magnetotransport system described in Section 3.3.2 and following the procedures presented there.

Fig. 4.10 shows the dependence of the (normalized) transverse resistance  $R_{xy}$  plane tensile strain, as it was previously pointed out.

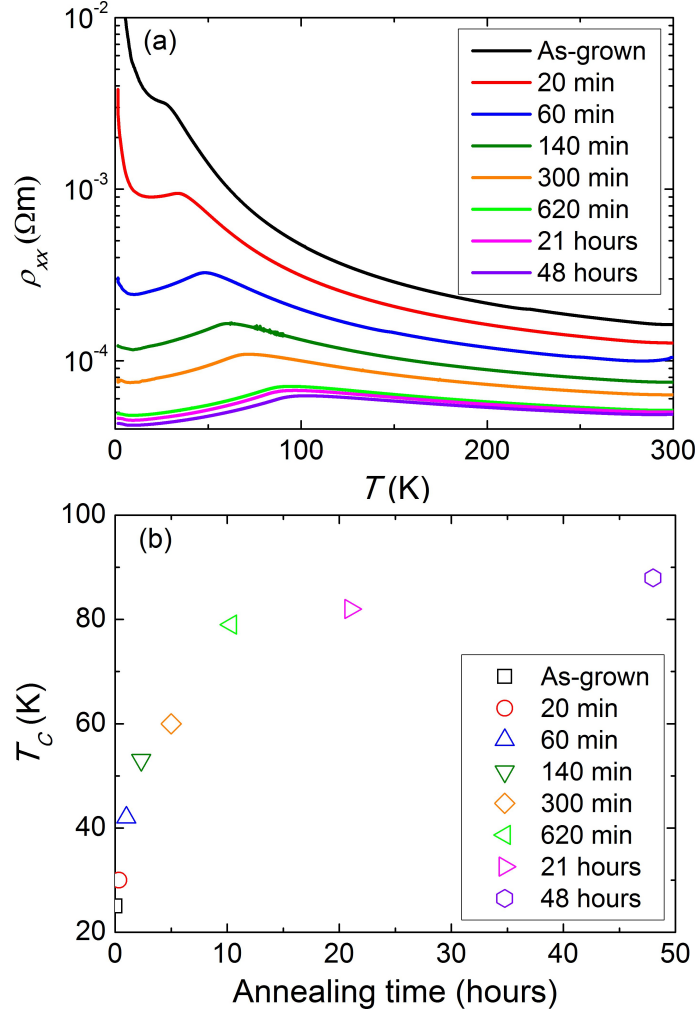


Figure 4.9: (a)  $\rho_{xx}$  vs  $T$  curves for Mn403 as-grown and annealed for increasing amounts of time at 180 °C. (b)  $T_C$  deduced from  $d\rho_{xx}/dT$  as a function of annealing time.

on  $H$  measured at  $T = 1.5$  K for Mn403 as-grown and annealed for increasing amounts of time.  $H$  is applied along the perpendicular-to-plane direction, which means that  $R_{xy}$  provides information on the component of the magnetization along this direction, since it is proportional to it via the AHE coefficient, as explained in Section 2.7.2. In the as-grown state  $R_{xy}$  could not be measured due to the very large  $\rho_{xx}$ . However, after only 20 minutes of annealing, the decrease in  $\rho_{xx}$  was sizeable enough to allow for  $R_{xy}$  to be measured and, as visible in Fig. 4.10, the resulting  $R_{xy} \sim M$  vs  $H$  loop closely resembles the loop obtained from SQUID magnetometry measurements for the as-grown sample (see Fig. 4.4 (g)), confirming the in-plane magnetic anisotropy. Annealing induces a transition from in-plane to perpendicular-to-plane magnetic anisotropy, as can be deduced from the  $R_{xy} \sim M$  vs  $H$  loop acquiring a square shape, again consistent with the  $M$  vs  $H$  loop obtained from SQUID magnetometry measurements for the

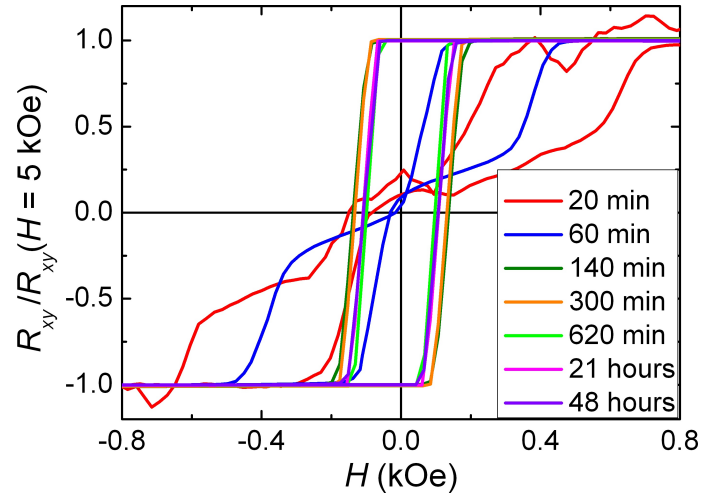


Figure 4.10:  $R_{xy}$  (normalized to  $R_{xy}$  at  $H = 5$  kOe) vs  $H$  measured at  $T = 1.5$  K for Mn403 as-grown and annealed for increasing amounts of time.  $H$  is applied along the perpendicular-to-plane direction.

fully annealed sample (see Fig. 4.4 (h)). Indeed after annealing for only 140 minutes the easy axis is fully aligned along the perpendicular-to-plane direction and further annealing steps simply result in a small decrease of the coercive field, possibly due to a decrease in the number of defects or to an increase in the hole concentration.

$R_{xy}$  vs  $H$  loops, with  $H$  applied again along the direction perpendicular to the film plane, have also been measured after each annealing step at various temperatures up to  $T_C$  and a change of the magnetic anisotropy from in-plane to perpendicular-to-plane was found to occur at  $T \sim 20$  K for Mn403 annealed for 60 minutes, as can be seen in Fig. 4.11. Further annealing and temperature increase

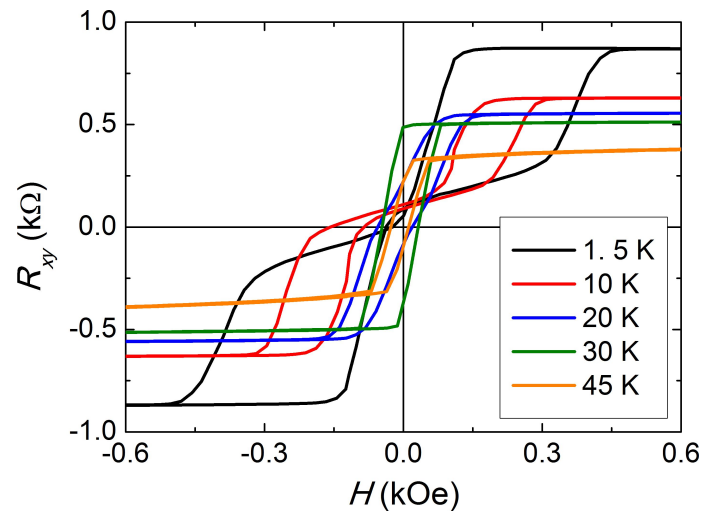


Figure 4.11:  $R_{xy}$  vs  $H$  measured at various temperatures for Mn403 annealed for 60 minutes.  $H$  is applied along the perpendicular-to-plane direction.

seem then to have similar effects on the magnetic anisotropy of this partially annealed Mn403. No change of the magnetic anisotropy with temperature was instead observed for Mn403 annealed for shorter or longer amounts of time.

Finally, the results of four terminal magnetotransport measurements performed on as-grown Mn498 at  $T = 1.5$  K are here briefly summarized. The in-plane AMR was investigated measuring  $R_{xx}$  and  $R_{xy}$  while rotating the saturating magnetic field in the plane of the sample. The data obtained were then fit using Eq. 2.10 and Eq. 2.11 to extract  $C_I$  and  $C_C$  (the other AMR coefficients could not be obtained for the Hall bar configuration chosen).  $C_C/C_I$  was found to be  $\sim 12\%$ , consistently with what expected for (Ga,Mn)As [93]. The value of the in-plane AMR (see Eq. 2.6) was found to be  $\sim -3.5\%$ , indicating that the lowest resistive state is the one in which  $M$  and  $I$  are parallel, as typical of (Ga,Mn)As too. The value of the perpendicular AMR (see Eq. 2.5) was measured to be  $\sim -4.1\%$ . The fact that  $|\text{AMR}_{\text{op}}| > |\text{AMR}_{\text{ip}}|$  indicates that the state in which  $M$  is perpendicular to the plane is characterized by a higher resistance than the state in which  $M$  is perpendicular to  $I$ , but in the plane of the sample. This circumstance normally occurs for in-plane compressively strained (Ga,Mn)As samples [90, 91], and might therefore suggest that a small in-plane compressive strain might be present also in as-grown Mn498.

## 4.7 Conclusions

This Chapter has shown some appealing properties of the ferromagnetic semiconductor (Ga,Mn)(As,P). Even if the predicted enhancements of  $T_C$  in (Ga,Mn)(As,P) [103] have not been observed, the fact that this material is characterized by transport properties and  $T_C$  values comparable to those of (Ga,Mn)As, with the added possibility of easily tuning its in-plane and perpendicular magnetic anisotropies via post-growth annealing and/or temperature, makes it not just a useful alternative to (Ga,Mn)As grown on relaxed (Ga,In)As for studies where perpendicular magnetic anisotropy is necessary, but also an extremely interesting type of III-V DMS in itself.

Structural, magnetometry, transport and magnetotransport measurements were performed on a series of  $(\text{Ga}_{0.94}, \text{Mn}_{0.06})(\text{As,P})$  samples grown on GaAs substrates with different P concentrations, both as-grown and annealed. Structural investigations showed that the perpendicular lattice constant  $a_{\perp}$  of these (Ga,Mn)(As,P) samples decreases upon increasing the P concentration and upon annealing, thus causing a transition in the in-plane growth strain either from larger to smaller values of compressive strain, or from compressive to tensile strain. Magnetometry measurements revealed that not all the samples under in-plane tensile strain are characterized by perpendicular magnetic anisotropy,

but just those with P concentrations  $\geq 9\%$ , that were annealed. This was explained taking into account the low hole concentrations for the as-grown samples and the uncertainties in establishing the sign of the small in-built growth strain for the annealed samples.  $T_C$  was found to decrease upon increasing the P concentration for both as-grown and annealed samples. Moreover, magnetometry measurements were used to investigate the competition between uniaxial and cubic anisotropy terms and its variation with temperature for samples with in-plane magnetic anisotropy. Transport measurements showed that the incorporation of P in (Ga,Mn)As does not dramatically affect its transport properties for  $y_{eff} \lesssim 9\%$ . The insulating behaviour reported for the sample with  $y_{eff} \sim 12\%$  could be ascribed either to the different conditions used to grow it or, more likely, to the occurrence of a metal-to-insulator transition for  $y_{eff} \gtrsim 9\% - 12\%$ . In any case, low resistivities with a metallic dependence on temperature could be obtained also in this sample via annealing. Finally, magnetotransport measurements demonstrated that a gradual transition from in-plane to perpendicular magnetic anisotropy occurs upon annealing and upon increasing the temperature, and were also used to provide preliminary information on the AMR in these samples.

# Chapter 5

## Manipulation of the magnetization in (Ga,Mn)As using a piezoelectric actuator

### 5.1 Introduction

The ability to manipulate the magnetization orientation of a ferromagnetic material with an electric field is an important goal for spintronics, since it would allow to improve the process of writing information in magnetic memories, which is currently performed, not very efficiently, with magnetic fields [42]. Magnetoelectric multiferroics, in which ferromagnetic and ferroelectric properties naturally coexist and interact [123, 124], represent an extremely promising class of materials in this respect and are currently being widely investigated. A different but equally attractive approach exploits the well understood circumstance that magnetic properties of DMS can be manipulated using non-magnetic parameters, including electric fields. In the past decade electric field control of ferromagnetism has in fact been achieved in several experiments involving ferromagnetic semiconductors like (In,Mn)As and (Ga,Mn)As [33, 34, 125, 126]. But since it relies on the possibility of varying the magnetic properties via hole depletion, this approach is effective only for ultra-thin samples with very low hole concentrations, a requirement that is typically fulfilled in as-grown materials with low Mn doping and consequently extremely low Curie temperatures  $T_C$ . The difficulty to obtain sizeable hole depletions in highly-doped ferromagnetic semiconductors has driven research to explore alternative routes to achieve electric manipulation of magnetism in these systems.

It is well known that the magnetic anisotropy in (Ga,Mn)As can be effectively tuned via strain, whether the latter is in-built due to growth on lattice-mismatched substrates [39, 119], as shown in the previous Chapter, or generated

by post-growth lithography [127, 40]. This is in fact a consequence of the large inverse magnetostrictive coefficients that are typical of materials characterized by strong spin-orbit coupling like (Ga,Mn)As. Taking this into account it becomes clear that an appealing prospect to achieve electric manipulation of magnetism in (Ga,Mn)As is that of using strain to mediate the coupling between its electric and magnetic properties. A work was published in 2003 [128] describing how sizeable strains can be generated in a non-magnetic GaAs film using a piezoelectric actuator, to which the film is bonded, and since then this technique has been applied to achieve strain-mediated electric control of the magnetization in (Ga,Mn)As in several experiments [129, 130, 131, 41]. These works have demonstrated that both reversible rotation of the magnetic easy axis by up to  $70^\circ$  and irreversible magnetization switching are possible in (Ga,Mn)As samples with relatively low Curie temperatures, for a range of temperatures up to 50 K. But in order to establish whether this method can overcome the issues encountered in the direct electric field control of magnetism its effectiveness should be tested in samples with high hole concentrations.

In this Chapter the effects of piezoelectric-induced strain on the magnetic properties of a highly-doped annealed (Ga,Mn)As sample (Mn437), with a high hole concentration and a  $T_C$  of 180 K, are investigated. The experiment is performed at a much higher temperature (150 K) than previous investigations, where larger strains can be generated by the actuator [128]. It will be shown through magnetotransport measurements that reversible rotations of the magnetic easy axis by roughly  $80^\circ$  can be achieved in this sample, thus demonstrating the clear advantage of strain-mediated control over direct electric field control of magnetism in samples with high hole concentrations. The results obtained from magnetotransport measurements will be moreover compared with those derived from SQUID magnetometry measurements, extracting the dependence of the piezo-induced uniaxial magnetic anisotropy constant upon strain in both cases and detailing the limitations encountered in the latter approach. Most of the results discussed in this Chapter can be found in [132].

## **5.2 Experimental method**

### **5.2.1 Piezoelectric actuator characteristics**

The piezoelectric actuators used for the magnetotransport and SQUID magnetometry measurements described in this Chapter are Part Nos. PSt 150/5 $\times$ 5/7 and PSt 150/2 $\times$ 3/5, respectively, from Piezomechanik. They are stacks of electroactive lead zirconate titanate (PZT) ceramic layers prepared with the on-stack-insulation technique. According to manufacturer specifications the two actuators

are characterized by the same physical properties and should generate the same strain, for the same applied voltage, to within 10%. They differ though in the dimensions: PSt 150/5×5/7 has an active length and a cross section of, respectively, 7 mm and 5 × 5 mm<sup>2</sup> while PSt 150/2×3/5 has an active length and a cross section of, respectively, 5 mm and 2 × 3 mm<sup>2</sup>.

The inverse piezoelectric effect, i.e. the variation of the dimensions of a crystal under the influence of an electric field, is usually described by the piezoelectric coefficients  $d_{ij}$ , defined as [133]:

$$d_{ij} = \left( \frac{\partial \epsilon_j}{\partial E_i} \right)^\sigma, \quad (5.1)$$

where  $\epsilon$  is the strain,  $E$  is the electric field,  $\sigma$  is the stress and the subscripts are  $i = 1 - 3$  and  $j = 1 - 6$ . For the piezoelectric actuators here considered,  $E$  is applied along the long axis direction, which is conventionally denoted with  $i = 3$ . According to manufacturer specifications, the PZT ceramic used for these actuators is characterized at room temperature by the following values of the  $d_{3j}$  piezoelectric coefficients:  $d_{33} = +640$  pm/V and  $d_{31} = d_{32} = -290$  pm/V. Hence, the application of a positive (negative) voltage to the actuator results in a tensile (compressive) strain along its poling direction, and in a compressive (tensile) strain, of roughly half magnitude, along the directions perpendicular to it. The Poisson ratio  $\nu = -d_{31}/d_{33} \equiv -d_{32}/d_{33}$  is 0.45 at room temperature, reasonably close to the value of 0.5 expected for a homogeneous isotropic material under uniaxial stress when the volume remains constant.

A detailed characterization of the longitudinal ( $\Delta L_3/L_3$ ) and transverse ( $\Delta L_1/L_1 = \Delta L_2/L_2$ ) strain as a function of voltage was carried out for PSt 150/5×5/7 in [128], for temperatures ranging between 4 K and 300 K. It was here shown that the maximum longitudinal (and consequently transverse) strain that can be generated by the actuator decreases substantially with decreasing the temperature, being  $\sim 1.2 \times 10^{-3}$  at  $T = 300$  K and more than a factor of ten smaller at  $T = 4$  K. This is a consequence of the fact that the PZT ceramic becomes piezoelectrically “hard” with decreasing the temperature, and the piezoelectric coefficients get correspondingly smaller.

Finally, it is important to mention that SQUID magnetometry measurements were performed on PSt 150/2×3/5, revealing that the magnetic response of the actuator is composed of a paramagnetic component and a ferromagnetic component with  $T_C > 300$  K. This could be ascribed to the presence of magnetic impurities in the wires and in the metallic sheets that separate the various ceramic layers in the actuator. Further details on the magnetic properties of PSt 150/2×3/5 will be given in Section 5.5.1.

## 5.2.2 Device fabrication

The material used in the experiment was a 25 nm thick layer of  $(\text{Ga}_{0.88},\text{Mn}_{0.12})\text{As}$  (Mn437), annealed in air for 48 hours at 180 °C. Two non adjacent pieces of this material, taken at a distance of 8.5 mm and 17.5 mm from the center of the wafer, were used for the measurements.<sup>1</sup> The former was patterned into the Hall bar geometry of Fig. 3.1 for magnetotransport measurements while the latter (of dimension  $2.5 \times 3 \text{ mm}^2$ ) was left unpatterned for SQUID magnetometry measurements. Following the procedure described in [128], the samples were then bonded to the piezoelectric actuators with a two-component epoxy<sup>2</sup>, after thinning their substrates down to  $190 \mu\text{m} \pm 10 \mu\text{m}$  by chemical etching. The thinning step is necessary to allow the strain to be transmitted effectively from the actuator to the  $(\text{Ga},\text{Mn})\text{As}$  layer. A strain gauge<sup>3</sup> was then glued with the same epoxy on top of the  $(\text{Ga},\text{Mn})\text{As}$  layer of the magnetotransport sample, next to the Hall bar. A strain gauge could not be glued on the SQUID magnetometry sample due to space constraints. Finally, both devices were cured in air for one hour at 80 °C to increase the bonding strength of the epoxy.

Fig. 5.1 shows a sketch of both devices. The current in the Hall bar flows along the  $[1\bar{1}0]$  direction. For both devices the  $[1\bar{1}0]$  direction was chosen to be along the poling direction of the actuator, although a small misalignment  $\delta$  was unavoidably introduced.  $\delta$  was measured with a high-resolution optical microscope and found to be  $2^\circ \pm 0.5^\circ$  for the magnetotransport device and  $1.5^\circ \pm 0.5^\circ$  for the SQUID magnetometry device. For any given combination of cubic and uniaxial magnetic anisotropies the sign of  $\delta$  determined the sense of rotation of the uniaxial easy axis induced by the strain. For this material the easy axis is along the  $[1\bar{1}0]$  direction and is expected to rotate anticlockwise for tensile strain (positive voltage) and clockwise for compressive strain (negative voltage). The strain gauge was also aligned along the  $[1\bar{1}0]$  direction and four terminal measurements of its resistance allowed to evaluate the uniaxial strain experienced by the  $(\text{Ga},\text{Mn})\text{As}$  layer<sup>4</sup> along the  $[1\bar{1}0]$  direction at different values of applied  $V$ . This uniaxial strain  $\epsilon \equiv \Delta L_3/L_3$  is in fact proportional to the variation of the

---

<sup>1</sup>The difference in  $T_C$  expected for these two pieces of  $(\text{Ga},\text{Mn})\text{As}$  is of about 4 K, the maximum ( $T_C = 183 \text{ K}$ ) occurring at a distance of  $\sim 8 \text{ mm}$  from the center of the wafer. Studies of the variation of  $T_C$  across the wafer used in this experiment were published in [43], in which Mn437 is labelled “wafer 3”.

<sup>2</sup>Part No. 45640, plus endfest 300, from UHU.

<sup>3</sup>Part No. WK-06-062TT-350, Karma alloy (Ni 74%, Cr 20%, Al 3%, Fe 3%), from Vishay Micro-Measurements.

<sup>4</sup>The strain generated by the piezoelectric actuator might be larger than the strain experienced by the  $(\text{Ga},\text{Mn})\text{As}$  layer, because of the presence of the GaAs substrate and the epoxy layer between them.

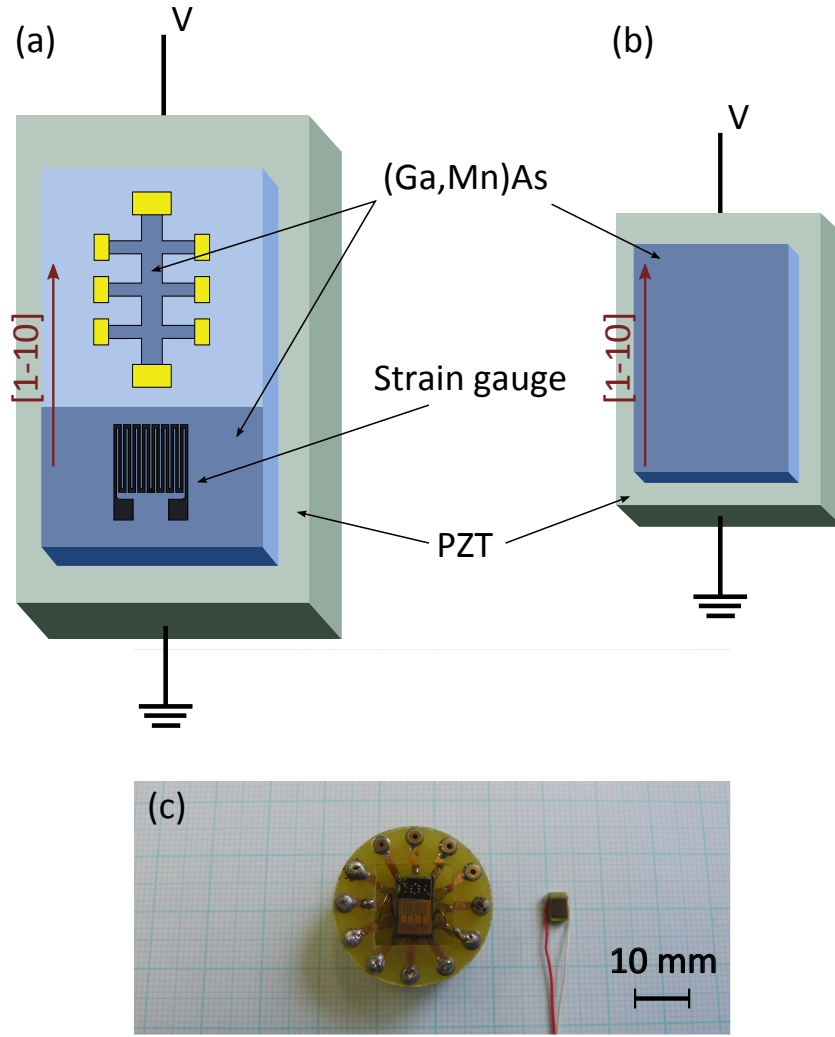


Figure 5.1: Sketch of the devices used for (a) magnetotransport measurements and (b) SQUID magnetometry measurements. The picture of both devices is shown in (c). One of the two strain gauges glued on the magnetotransport device did not work.

strain gauge resistance  $\Delta R$  according to:

$$\epsilon = \frac{1}{G_F} \left( \frac{\Delta R}{R_0} \right), \quad (5.2)$$

where  $G_F$  is the gauge factor and  $R_0$  is the resistance of the strain gauge in the absence of strain, both known from Vishay Micro-Measurements technical data. The dependence of  $\epsilon$  on  $V$  at  $T = 150$  K, which is the temperature at which the experiments were performed, is plotted in Fig. 5.2 for  $V$  going from 0 V to +85 V to -70 V and back to 0 V. The presence of hysteresis in the  $\epsilon$  vs  $V$  loop is a well

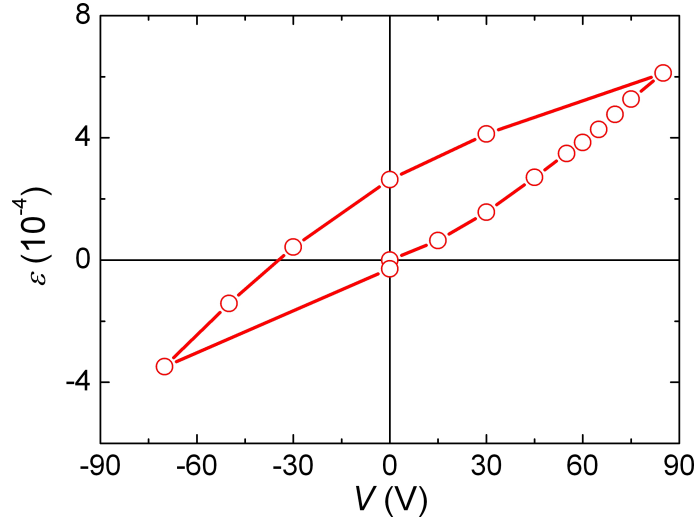


Figure 5.2:  $\epsilon$  vs  $V$  measured at  $T = 150$  K by the strain gauge glued on top of the (Ga,Mn)As layer, along the poling direction of the actuator, for  $V$  going from 0 V to +85 V to  $-70$  V and back to 0 V. The size of the error bars in  $\epsilon$  is smaller than the size of the symbols. As discussed in the text, this figure just provides the variation of the value of  $\epsilon$  relative to its initial state at  $V = 0$ , since the absolute value of the latter could not be measured.

known property of PZT ceramics [134] and was shown to be quite large for PSt 150/5 $\times$ 5/7 also in [128], both at 300 K and at 77 K. The range of  $V$  for which the strain was measured is the same as that used in magnetotransport measurements while a smaller range of  $V$  was used in SQUID magnetometry measurements. Larger values of negative  $V$  were avoided to prevent the piezoelectric actuator from depoling. An important point to raise, that does not emerge from Fig. 5.2, is that the strain experienced by the (Ga,Mn)As layer at  $T = 150$  K is non-zero even for  $V = 0$ . The different thermal contraction coefficients of the sample and the piezoelectric actuator, combined with the anisotropic nature of the thermal contraction of the latter are in fact probably responsible for the creation of an in-plane biaxial tensile strain and of a small in-plane uniaxial tensile strain on the (Ga,Mn)As layer when cooling the device from room temperature down to  $T = 150$  K. These strains could not be measured with the strain gauge, since the resistance of the latter varies not only with strain but clearly also with temperature. For this reason in the following the symbol  $\epsilon$  will be replaced with the more meaningful symbol  $\Delta\epsilon$ , which will be arbitrarily set to 0 for  $V = 0$  V.

### 5.3 Material characterization

SQUID magnetometry measurements were performed on annealed Mn437, without the actuator, to investigate its magnetic properties, in particular its magnetic

anisotropy. These measurements were carried out using the magnetometry system described in Section 3.3.1 and following the procedures presented there.

Fig. 5.3 shows  $M_R$  vs  $T$  curves along different in-plane directions. It can

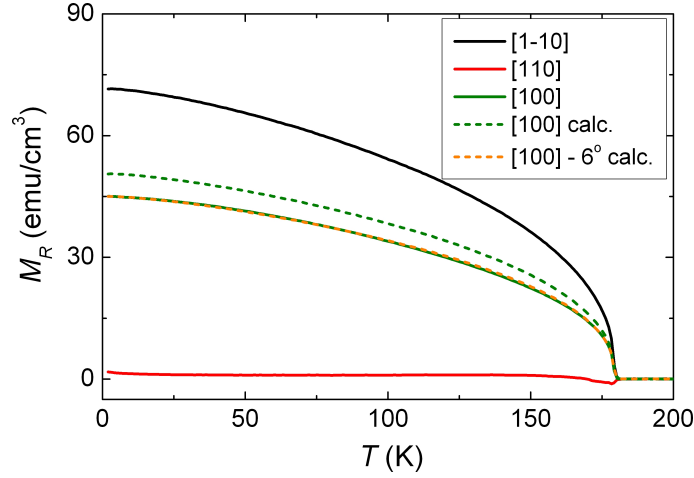


Figure 5.3:  $M_R$  vs  $T$  curves measured for annealed Mn437 along the in-plane  $[1\bar{1}0]$  (black),  $[110]$  (red) and  $[100]$  (solid green) directions.  $M_R$  along the  $[100]$  direction (dashed green) and along the direction at  $6^\circ$  to it (dashed orange) are calculated according to the Stoner-Wohlfarth single-domain model described in Sections 2.5.3 and 3.3.1.

be clearly seen that for the whole temperature range up to  $T_C = 180$  K the uniaxial magnetic anisotropy, that favours the  $[1\bar{1}0]$  direction, dominates over the cubic magnetic anisotropy, that instead favours the  $[100]$  and  $[010]$  directions. Hence at all temperatures the  $[1\bar{1}0]$  and  $[110]$  directions are the magnetic easy and hard axis orientations, respectively. The fact that  $M_{[100]}$  is slightly smaller than the value expected from the Stoner-Wohlfarth single-domain model  $M_{[100]} = M_{[1\bar{1}0]} \cdot \cos(\pi/4)$  represented by the dashed green curve in Fig. 5.3 is probably just due to a small misalignment of the sample in the SQUID. In fact, it can be seen that the measured  $M_{[100]}$  vs  $T$  curve can be predicted by this model when allowing for the presence of a misalignment of  $6^\circ$  to the  $[100]$  direction. This suggests that the sample remains in a single-domain state, with dominant uniaxial magnetic anisotropy, at all temperatures.

Fig. 5.4 shows  $M$  vs  $H$  loops measured at  $T = 150$  K, with  $H$  applied along the magnetic easy and hard axis directions. As expected, the remanent magnetization is large along the easy axis direction  $[1\bar{1}0]$  and almost zero<sup>5</sup> along the hard axis direction  $[110]$ . The hard axis loop was fitted numerically using the Stoner-Wohlfarth single-domain model [81] to extract the values of the in-plane uniaxial  $K_U$  and cubic  $K_C$  magnetic anisotropy constants at  $T = 150$  K. It was thus obtained  $K_U = 144.6 \text{ J/m}^3 \pm 4\%$  and  $K_C = 45 \text{ J/m}^3 \pm 30\%$ .

<sup>5</sup>The presence of a small hysteresis along the hard axis direction is again due to a small misalignment of the sample in the SQUID.

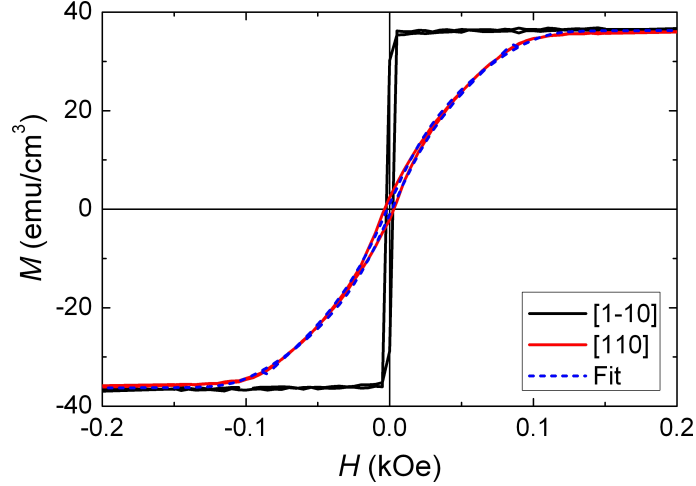


Figure 5.4:  $M$  vs  $H$  loops measured at  $T = 150$  K for annealed Mn437, with  $H$  applied along the in-plane  $[1\bar{1}0]$  (black) and  $[110]$  (red) directions. The dashed blue loop is the result of the fitting to the  $[110]$  loop using the Stoner-Wohlfarth single-domain model described in Sections 2.5.3 and 3.3.1.

## 5.4 Magnetotransport results

Four terminal magnetotransport measurements were performed at  $T = 150$  K on the Hall bar of the device shown in Fig. 5.1 (a) using the magnetotransport system described in Section 3.3.2. Both longitudinal  $R_{xx}$  and transverse  $R_{xy}$  resistances were measured for different voltages  $V$  applied to the piezoelectric actuator, while either varying the intensity of the magnetic field  $H$  or its direction. As for previous works [129, 130, 131, 41], these measurements allowed to investigate the effects of the piezoelectric actuator on the magnetic anisotropy of the sample. Given that measurements of the longitudinal AMR contain the contribution of the IMR, which is difficult to evaluate at small values of  $H$ , it was chosen to use the transverse AMR to extract the desired information from the experimental data. For this reason, just the results obtained from measurements of  $R_{xy}$  are presented in this Section.

### 5.4.1 Transverse AMR in saturating magnetic field

Fig. 5.5 shows the dependence of  $R_{xy}$  on the angle  $\gamma$  that  $H$  forms with the  $[1\bar{1}0]$  direction, for  $H = 6$  kOe and for two different values of the voltage applied to the piezoelectric actuator:  $V = 0$  V and  $V = 85$  V. In Chapter 2 it has been shown that  $R_{xy}$  can be expressed as:

$$R_{xy} = C_I \sin 2\phi - C_{I,C} \sin(4\psi - 2\phi), \quad (5.3)$$

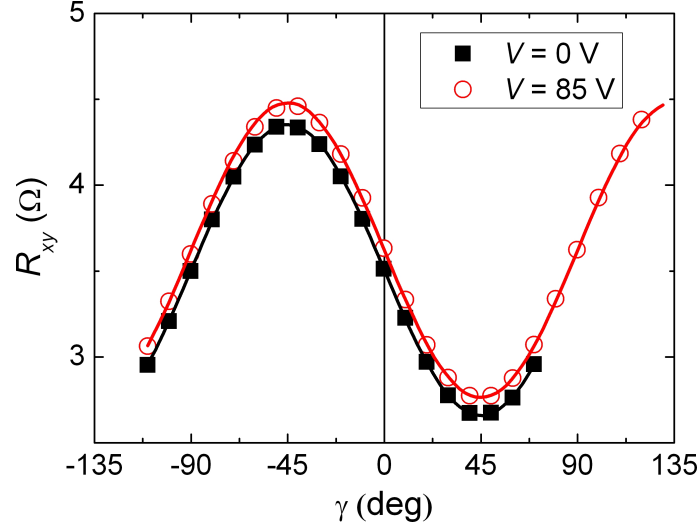


Figure 5.5:  $R_{xy}$  vs  $\gamma$  at  $T = 150$  K and  $H = 6$  kOe, for  $V = 0$  V and  $V = 85$  V. The symbols are the experimental data while the solid lines are the results of their fitting with  $R_{xy} = R_{xy}^0 + \Delta R \sin 2\gamma$  (see text for fitting details).

where  $\phi$  is the angle between  $M$  and  $I$ ,  $\psi$  is the angle between  $M$  and the  $[110]$  direction,  $C_I$  and  $C_{I,C}$  are the non-crystalline term and crossed non-crystalline/crystalline term, respectively. Since in the Hall bar the current flows along the  $[\bar{1}10]$  direction it can be easily proven that  $\psi = \phi - \pi/2$ . Thus Eq. 5.3 can be rewritten as:

$$R_{xy} = \Delta R \sin 2\phi, \quad (5.4)$$

where  $\Delta R = C_I - C_{I,C}$ . Given that  $H = 6$  kOe is much larger than the anisotropy field  $H_K \sim 0.2$  kOe (see Fig. 5.4), the magnetization is always saturated along the field direction, even when the latter is applied along the hard axis. Any variation of the magnetic anisotropy induced by the strain does not then modify the measured data. Hence  $\phi = \gamma$  and Eq. 5.4 can be used to fit to the experimental data in Fig. 5.5, provided that a fitting parameter  $R_{xy}^0$  is added to it, to account for the offset from zero of the average value of  $R_{xy}$ . This vertical shift in the  $R_{xy}$  experimental data is caused by the appearance of a component of the longitudinal resistance in the measurement of  $R_{xy}$ , arising from imperfections in the sample geometry. Given that  $R_{xx}$  is roughly 4.6 k $\Omega$ , this component is actually rather small. The results of the fittings are:  $R_{xy}^0 = 3.5$   $\Omega$  and  $\Delta R = -0.85$   $\Omega$  for the  $V = 0$  V measurement;  $R_{xy}^0 = 3.62$   $\Omega$  and  $\Delta R = -0.86$   $\Omega$  for the  $V = 85$  V measurement. The values of  $R_{xy}^0$  and  $\Delta R$  vary by a few percent between the measurements at  $V = 0$  V and  $V = 85$  V. Similar variations were observed also in measurements of  $R_{xx}$  (not shown here) and are ascribable to the effects of strain on the resistance of the material, in a similar way as a strain gauge is affected by it.

For the remainder of this Section the experimental data will be shown after subtraction of the offset  $R_{xy}^0$ .

### 5.4.2 Dependence of $\Delta R$ on the magnetic field

As a result of the working temperature being close to  $T_C$ , the amplitude  $\Delta R$  of the transverse AMR was found to be significantly dependent on the intensity of the magnetic field  $H$ . This circumstance can be explained as follows. In a ferromagnet for temperature close to  $T_C$  the polarization induced by  $H$  on the magnetic moments is non negligible and results in a dependence of the saturation magnetization  $M_S$  at that temperature on  $H$  [69]. Since  $\Delta R$  is influenced by the value of  $M_S$  [135], the dependence of  $M_S$  on  $H$  gives rise to a dependence of  $\Delta R$  on  $H$ .

Fig. 5.6 shows the dependence of  $R_{xy}$  on  $H$  for  $\gamma = -45^\circ$  and  $\gamma = +45^\circ$  at  $V = 0$  V.  $H$  is swept from +6 kOe to -6 kOe and back to +6 kOe. For

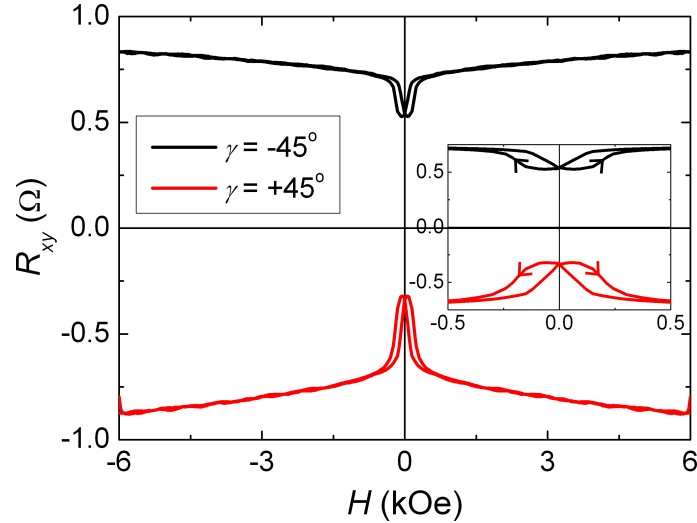


Figure 5.6:  $R_{xy}$  vs  $H$  loops at  $T = 150$  K and  $V = 0$  V for  $\gamma = -45^\circ$  and  $\gamma = +45^\circ$ .  $H$  is swept from +6 kOe to 6 kOe and back to 6 kOe. The portion of the curves around  $H = 0$  is zoomed-in in the inset, where the arrows indicate the sweep direction of  $H$ .

saturation magnetic fields  $\gamma = -45^\circ$  and  $\gamma = +45^\circ$  are those angles at which  $R_{xy}$  is respectively maximum and minimum, as can be seen in Fig. 5.5. It is then clear from Fig. 5.6 that  $\Delta R$  depends on  $H$  even when the direction of  $M$  does not. In fact, if this was not the case, both  $R_{xy}$  vs  $H$  loops would be flat for saturating magnetic fields (i.e. for  $|H| \gtrsim 0.2$  kOe), given that  $M$  would be constantly lying along the direction of  $H$  at either  $-45^\circ$  or  $+45^\circ$ <sup>6</sup>. The dependence of the

<sup>6</sup>The behaviour of  $R_{xy}$  vs  $H$  loops for  $|H| \lesssim 0.2$  kOe will be explained in the next Section, where it will become clear that the two loops in Fig. 5.6 should meet at  $H = 0$ . The fact

amplitude of the AMR on the applied magnetic field,  $\Delta R(H)$ , can be derived for saturating magnetic fields by averaging the upper and lower branches for each of the two loops in Fig. 5.6, taking their difference and dividing it by 2.  $\Delta R(H)$  thus obtained is shown in Fig. 5.7 for  $|H| > 0.45$  kOe, along with the curve  $\Delta R(H) = \Delta R_0 + a|H| + b|H|^{1/3}$  used to fit to it, with  $\Delta R_0 = -0.575 \Omega$ ,  $a = -0.029 \Omega$  and  $b = -0.312 \Omega$ . This expression of  $\Delta R(H)$ , which fits very well

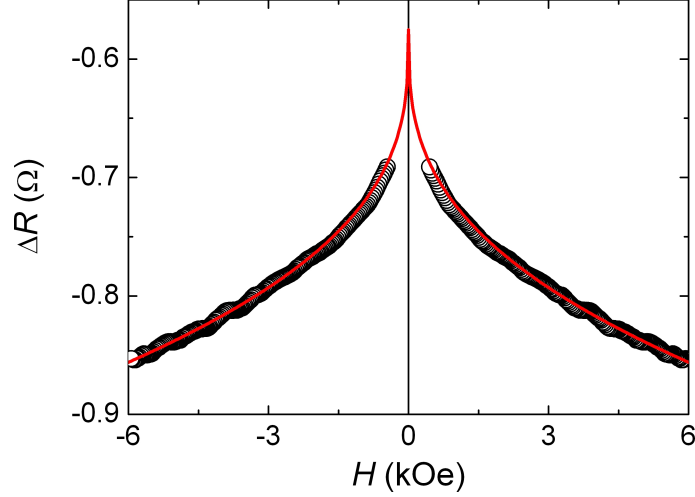


Figure 5.7:  $\Delta R$  vs  $H$  at  $T = 150$  K. The symbols are the experimental data obtained from  $[\overline{R_{xy}}(\gamma = +45^\circ) - \overline{R_{xy}}(\gamma = -45^\circ)]/2$  for  $|H| > 0.45$  kOe ( $\overline{R_{xy}}$  is used to indicate the average between the upper and lower branches), while the solid line is the result of their fitting with  $\Delta R(H) = \Delta R_0 + a|H| + b|H|^{1/3}$  (see text for fitting details).

to the experimental data, is used for the analysis of the magnetotransport results discussed in the following.

### 5.4.3 Effects of the piezoelectric actuator on the magnetic anisotropy

The position of the magnetic easy axis for the different voltages  $V$  applied to the piezoelectric actuator was inferred from measurements of the transverse AMR. It has been shown that, to a very good approximation,  $R_{xy}$  can be expressed as:

$$R_{xy} = \Delta R \sin 2\phi, \quad (5.5)$$

where  $\phi$  is the angle between  $M$  and  $I$ . Since at zero magnetic field  $M$  lies along the magnetic easy axis, the orientation of the latter with respect to the  $[1\bar{1}0]$  direction can be deduced from the value of  $R_{xy}$  at  $H = 0$ .

---

that this does not happen is just due to the fast rate at which  $H$  was swept during these measurements.

Measurements of  $R_{xy}$  vs  $H$  with  $H$  applied along different in-plane directions were performed for a series of positive and negative values of  $V$ . In each measurement  $H$  was swept from  $+0.6$  kOe to  $-0.6$  kOe and back to  $+0.6$  kOe.  $V$  was initially increased from  $0$  V to  $+85$  V, then decreased to  $-70$  V, and finally increased back to  $0$  V. Fig. 5.8 shows the result of some of these measurements, for the initial ( $0$  V), the maximum ( $+85$  V) and the minimum ( $-70$  V) value of  $V$ . The behaviour of  $R_{xy}$  vs  $H$  in these loops is clearly strongly dependent on the direction of  $H$ . When  $H$  is applied along a direction close enough to the magnetic easy axis direction  $R_{xy}$  has similar values at saturation and remanence, since  $M$  does not rotate much away from the direction of  $H$  when this is reduced from saturating values to zero. This is the case of the black loops in Fig. 5.8. On the other hand, when  $H$  is applied along a direction away from the magnetic easy axis direction significant variations in  $R_{xy}$  occur, corresponding to large rotations of  $M$ . This is the case of the red loops in Fig. 5.8, in which  $H$  is applied along a direction close to the magnetic hard axis direction.

Even if the lack of significant  $M$  rotations in the black loops of Fig. 5.8 would already suggest that they were measured, to a good approximation, along the magnetic easy axis direction, the latter was more precisely derived, for each applied  $V$ , from the value of  $R_{xy}(H = 0)$  for all the measured  $H$  directions. Since a small variation of  $R_{xy}(H = 0)$  with  $\gamma$  was found to occur<sup>7</sup>, the orientation of the magnetic easy axis was extracted from these data with an uncertainty of  $\pm 1^\circ$ . Both the variation of  $R_{xy}^0$  and  $\Delta R$  with  $V$  discussed in Section 5.4.1 and the variation of  $\Delta R$  with  $H$  discussed in Section 5.4.2 were taken into account in this evaluation. The magnetic easy axis orientation for the  $V = 0$  V,  $V = +85$  V and  $V = -70$  V cases is displayed in the diagrams next to the experimental data in Fig. 5.8. The easy axis was thus found to have already rotated by  $-5.5^\circ$  from the “intrinsic”  $[1\bar{1}0]$  direction (see SQUID magnetometry characterization in Section 5.3) when no voltage was applied to the actuator. This circumstance is due to the creation of a small in-plane uniaxial strain when cooling the device from room temperature down to  $T = 150$  K which, as previously explained, probably arises from the anisotropic nature of the thermal contraction of the piezoelectric actuator<sup>8</sup>. Upon application of a positive  $V$  the easy axis rotated further anticlockwise towards the  $[110]$  direction and reached an angle of  $-81^\circ$  for  $V = +85$  V, while it rotated clockwise upon application of a negative  $V$ , reaching an angle of  $-3^\circ$  for  $V = -70$  V (the easy axis angles are all referred to the  $[1\bar{1}0]$  direction). Overall then it was proven that the piezoelectric actuator can generate a reversible rotation of the uniaxial easy axis by  $\sim 78^\circ$  in this device.

<sup>7</sup>In principle, as already mentioned,  $R_{xy}(H = 0)$  should not depend on  $\gamma$ , since for  $H = 0$   $M$  lies along the (only) magnetic easy axis.

<sup>8</sup>Although more unlikely, this small in-plane uniaxial strain could in principle be induced also by the epoxy layer.

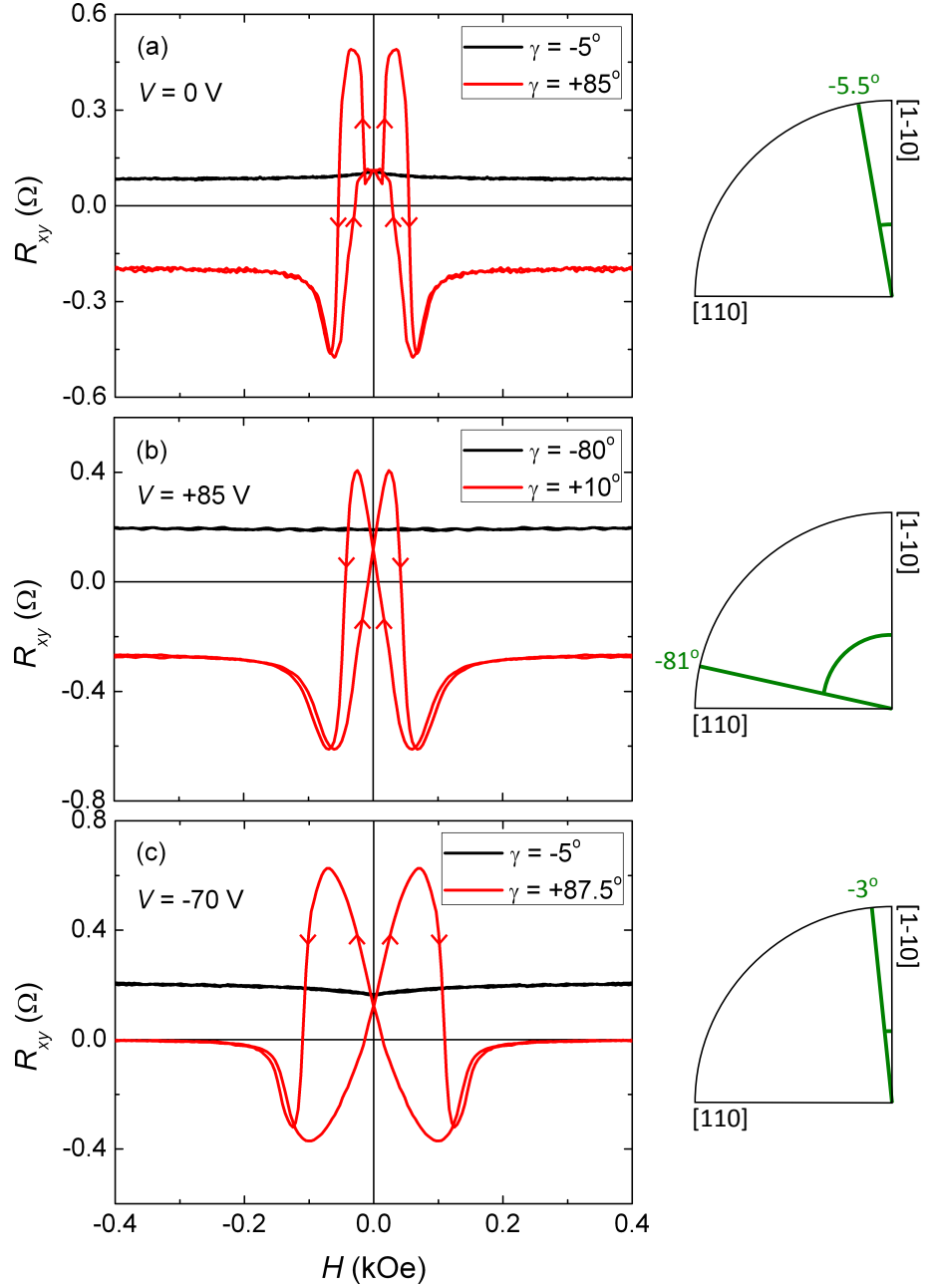


Figure 5.8:  $R_{xy}$  vs  $H$  loops at  $T = 150$  K with  $H$  applied along different in-plane directions for (a)  $V = 0$  V, (b)  $V = +85$  V and (c)  $V = -70$  V. In each measurement  $H$  is swept from  $+0.6$  kOe to  $-0.6$  kOe and back to  $+0.6$  kOe. The arrows on the loops indicate the sweep direction of  $H$ . The diagrams to the right display the orientation of the magnetic easy axis in each case, extracted from the correspondent  $R_{xy}$  vs  $H$  loops.

Fig. 5.9 shows the dependence of the easy axis orientation on the strain  $\Delta\epsilon$  generated by the actuator. The relationship between  $V$  and  $\Delta\epsilon$  was shown in Fig. 5.2. It can be seen that the most rapid variations in the orientation of the easy axis are obtained for  $\Delta\epsilon$  values roughly between  $1 \times 10^{-4}$  and  $4 \times 10^{-4}$ , whereas large changes in  $\Delta\epsilon$  are necessary to vary the orientation of the easy axis

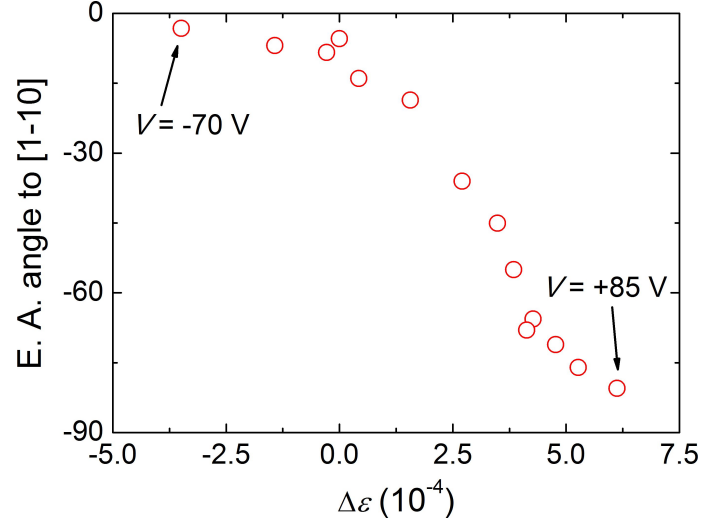


Figure 5.9: Easy axis (E. A.) orientation (with respect to the  $[1\bar{1}0]$  direction) vs  $\Delta\epsilon$  at  $T = 150$  K.  $\Delta\epsilon = 6.12 \times 10^{-4}$  and  $\Delta\epsilon = -3.49 \times 10^{-4}$  are respectively generated applying  $V = +85$  V and  $V = -70$  V to the piezoelectric actuator. The size of the error bars in both the easy axis orientation and in  $\Delta\epsilon$  is smaller than the size of the symbols.

by a small amount when this is close to either the  $[110]$  direction (large positive  $V$ ) or the  $[1\bar{1}0]$  direction (small positive  $V$  and negative  $V$ ).

The effects of the piezoelectric actuator on the magnetic properties of (Ga,Mn)-As can be modelled via an in-plane uniaxial magnetic anisotropy term, with anisotropy constant  $K_{Up}$ , that favours the  $[110]+\delta$  direction for  $K_{Up} > 0$  ( $\Delta\epsilon > 0$ ) and the  $[1\bar{1}0]+\delta$  direction for  $K_{Up} < 0$  ( $\Delta\epsilon < 0$ ). By varying  $V$ , the sign and strength of  $K_{Up}$  are varied and the easy axis rotates correspondingly. It has been shown theoretically that uniaxial magnetic anisotropy constants depend linearly on the strain from which they originate, unless strains larger than 1% are being considered [77]. A linear dependence of  $K_{Up}$  on  $\Delta\epsilon$  should then be expected in this experiment. The remainder of this Section is devoted to describe how the dependence of  $K_{Up}$  on  $\Delta\epsilon$  can be extracted from the experimental data.

According once more to the Stoner-Wohlfarth single-domain model [81], the magnetic energy of this (Ga,Mn)As-piezoelectric actuator hybrid system can be phenomenologically expressed as:

$$E = -\frac{K_C}{4} \sin^2 2\phi + K_U \sin^2 \phi - K_{Up} \sin^2(\phi - \delta) - M_S H \cos(\gamma - \phi), \quad (5.6)$$

where the first, second and third terms are respectively the in-plane “intrinsic” cubic, “intrinsic” uniaxial and piezo-induced uniaxial magnetic anisotropy energies, while the last term is the magnetic field-dependent Zeeman energy.  $\phi$  and  $\gamma$  are, as usual, the angles formed by  $M$  and  $H$ , respectively, with the  $[1\bar{1}0]$  direction

(which is also the direction of  $I$ ).

It was initially thought that the most accurate way to extract the value of  $K_{Up}$  for each  $V$  from the experimental data would be that of fitting numerically the  $R_{xy}$  vs  $H$  loops closest to the hard axis direction.  $M$  vs  $H$  loops can in fact be derived from  $R_{xy}$  vs  $H$  loops via Eq. 5.5, and Eq. 5.6 with the condition  $dE/d\phi = 0$  can then be used to fit them in the same way as it was done for the  $M$  vs  $H$  hard axis loop in Section 5.3. However, some difficulties, which are here briefly addressed, were encountered in this approach. Fig. 5.10 shows the  $R_{xy}$  vs  $H$  loops closest to the hard axis direction for  $V = 0$  V,  $V = +85$  V,  $V = -70$  V (i.e. the same  $R_{xy}$  vs  $H$  loops shown in Fig. 5.8),  $V = +45$  V and  $V = +55$  V, together with the minimum and maximum values expected for  $R_{xy}$  vs  $H$  according to the variation of  $\Delta R$  with  $H$  derived in Section 5.4.2. The

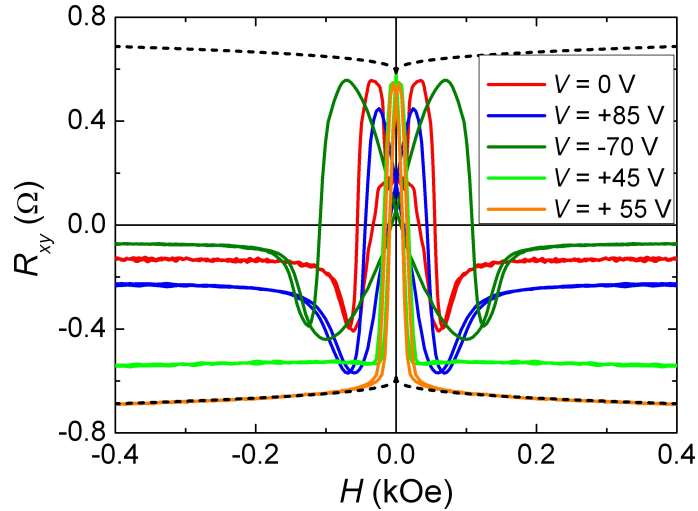


Figure 5.10:  $R_{xy}$  vs  $H$  loops at  $T = 150$  K for  $V = 0$  V,  $V = +85$  V,  $V = -70$  V,  $V = +45$  V and  $V = +55$  V. In each measurement  $H$  is swept from  $+0.6$  kOe to  $-0.6$  kOe and back to  $+0.6$  kOe. The minimum and maximum values of  $R_{xy}$  vs  $H$  are shown by the dashed black lines.

minimum and maximum values of the  $R_{xy}$  vs  $H$  loops for  $V = 0$  V,  $V = +85$  V and  $V = -70$  V should correspond to those expected from the variation of  $\Delta R$  with  $H$ , since  $M$  should rotate through the angles at which  $R_{xy}$  becomes minimum or maximum when  $H$  is decreased from saturation to zero. But this is not the case, as can be clearly seen in Fig. 5.10<sup>9</sup>. On the other hand, the fact that the minimum and maximum values of the  $R_{xy}$  vs  $H$  loops for, respectively,  $V = +55$  V and  $V = +45$  V match the expected ones for a wide range of values of  $H$ , including  $H = 0$ , would suggest that the cause of this behaviour is physical rather than an artefact due to a wrong functional form of  $\Delta R(H)$ . It could then be deduced that the variations of  $R_{xy} \sim M$  with  $H$  observed in the experimental

<sup>9</sup>This was found to occur not only in hard axis loops but also in most other loops.

data are influenced by multidomain effects. Since the Stoner-Wohlfarth model is valid only in single-domain samples, it could not be used to fit to these loops and this approach was then abandoned.

It was next chosen to extract the dependence of  $K_{Up}$  on strain from the easy axis orientation previously derived from  $R_{xy}(H = 0)$  for each  $V^{10}$ . This was done using Eq. 5.6 with  $H = 0$  and imposing the condition  $dE/d\phi = 0$ . It was thus obtained:

$$K_{Up} = \frac{K_U - K_C \cos 2\phi}{\cos 2\delta - \frac{\sin 2\delta}{\tan 2\phi}}, \quad (5.7)$$

where  $\phi$  here represents the angle between the easy axis and the  $[1\bar{1}0]$  direction, because  $H = 0$ . Beside being useful to extract the desired information on the dependence of  $K_{Up}$  on strain, Eq. 5.7 can be used to investigate how the dependence of the easy axis orientation on  $K_{Up}$  is expected to vary by varying some of the parameters in Eq. 5.7. This is shown in Fig. 5.11. Essentially, this Figure

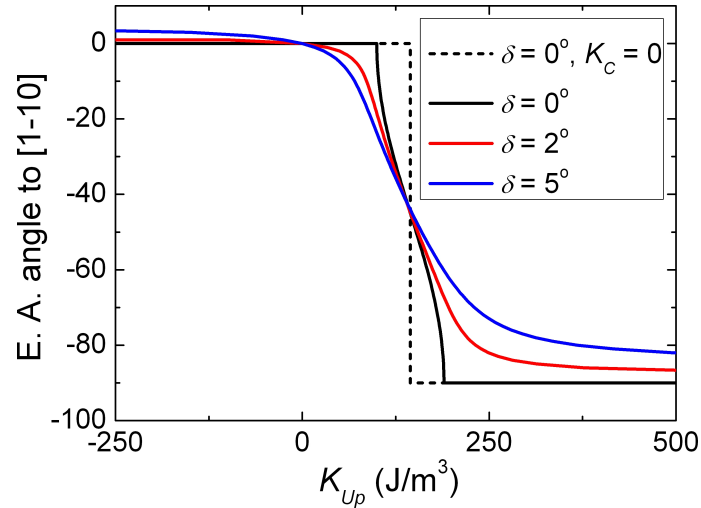


Figure 5.11: Easy axis (E. A.) orientation (with respect to the  $[1\bar{1}0]$  direction) vs  $K_{Up}$  derived from Eq. 5.7 for different values of  $\delta$ . All the curves are derived with  $K_U = 144.6 \text{ J/m}^3$  and  $K_C = 45 \text{ J/m}^3$ , a part from the dashed curve, which is derived with  $K_U = 144.6 \text{ J/m}^3$  and  $K_C = 0$ .

is the theoretical counterpart of Fig. 5.9, with  $K_{Up}$  replacing its experimental analogue  $\Delta\epsilon$  ( $K_{Up} \leq 0$  for  $\Delta\epsilon \leq 0$ ). As a matter of fact, the dependence of the easy axis orientation on  $K_{Up}$  for  $\delta = 2^\circ$  in Fig. 5.11 is similar to the dependence of the easy axis orientation on  $\Delta\epsilon$  in Fig. 5.9, with the most rapid variations in the orientation of the easy axis occurring when the latter is lying at angles roughly

<sup>10</sup>It is important to notice that even if  $M$  changes direction via the formation of magnetic domains, extracting the easy axis orientation from the value of  $R_{xy}$  at  $H = 0$  is a valid approach, because this value does not depend on the fact that  $M$  might be lying along the positive  $[1\bar{1}0]$  direction in some domains and the negative  $[1\bar{1}0]$  direction in others ( $R_{xy}(\mathbf{M}) = R_{xy}(-\mathbf{M})$ ).

in the middle of the range between the  $[110]$  and  $[1\bar{1}0]$  directions. It can also be seen from Fig. 5.11 that the reorientation of the easy axis from the  $[1\bar{1}0]+\delta$  direction to the  $[110]+\delta$  direction is more abrupt for smaller values of  $\delta$ . In the limit of  $\delta = 0$  and  $K_C = 0$ , this reorientation becomes a switch, which occurs for  $K_{Up} = K_U$ , as can be deduced from Eq. 5.7.

Finally, the dependence of  $K_{Up}$  on strain derived from Eq. 5.7 is plotted in Fig. 5.12. The experimental data obtained for negative voltages were not included

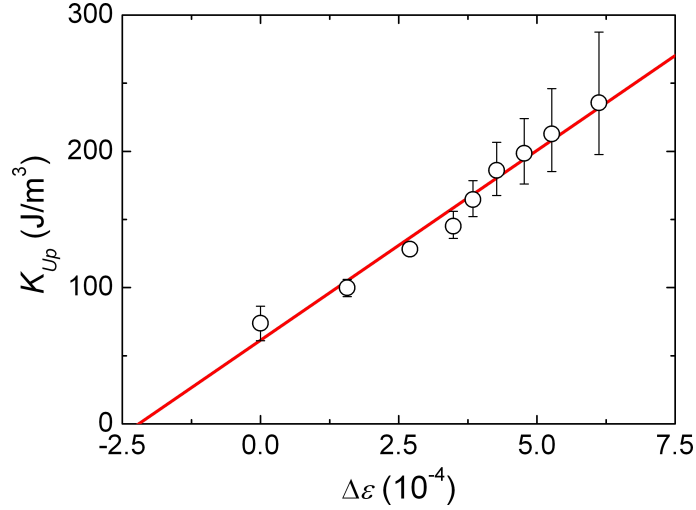


Figure 5.12:  $K_{Up}$  vs  $\Delta\epsilon$  at  $T = 150$  K. The symbols are the values extracted from the easy axis orientation, while the solid line is their linear fitting with slope of  $\sim 28$  J/m<sup>3</sup> per  $10^{-4}$  strain. The size of the error bars in  $\Delta\epsilon$  is smaller than the size of the symbols.

in Fig. 5.12 because of the large uncertainties associated with deriving  $K_{Up}$  from the easy axis orientation for these voltages. The error bars in  $K_{Up}$  are due to the combined uncertainties in  $K_U$ ,  $K_C$ , the easy axis orientation and the value of  $\delta$ , the latter being dominant. The dependence of  $K_{Up}$  on strain is linear within the errors, as expected [77], and the best straight line through the points has a slope of  $\sim 28$  J/m<sup>3</sup> per  $10^{-4}$  strain.

## 5.5 SQUID magnetometry results

SQUID magnetometry measurements were performed at  $T = 150$  K on the device shown in Fig. 5.1 (b) using the SQUID magnetometer described in Section 3.3.1.  $M$  vs  $H$  loops were measured with  $H$  applied along the  $[1\bar{1}0]$  direction for different voltages  $V$  applied to the piezoelectric actuator to explore the effects of the latter on the magnetic anisotropy of the sample. Differently from magnetotransport measurements, magnetometry measurements are a direct way to evaluate the magnetic properties of a material, thus in principle being more reliable to

investigate inverse magnetostrictive effects.

### 5.5.1 Magnetic properties of the piezoelectric actuator

As mentioned in Section 5.2.1, SQUID magnetometry measurements were performed on the piezoelectric actuator PSt 150/2×3/5 before the (Ga,Mn)As piece of wafer was bonded to it. Fig. 5.13 (a) shows  $m$  vs  $H$  loops measured at  $T = 150$  K with  $H$  applied along the poling direction of the actuator. It is evident

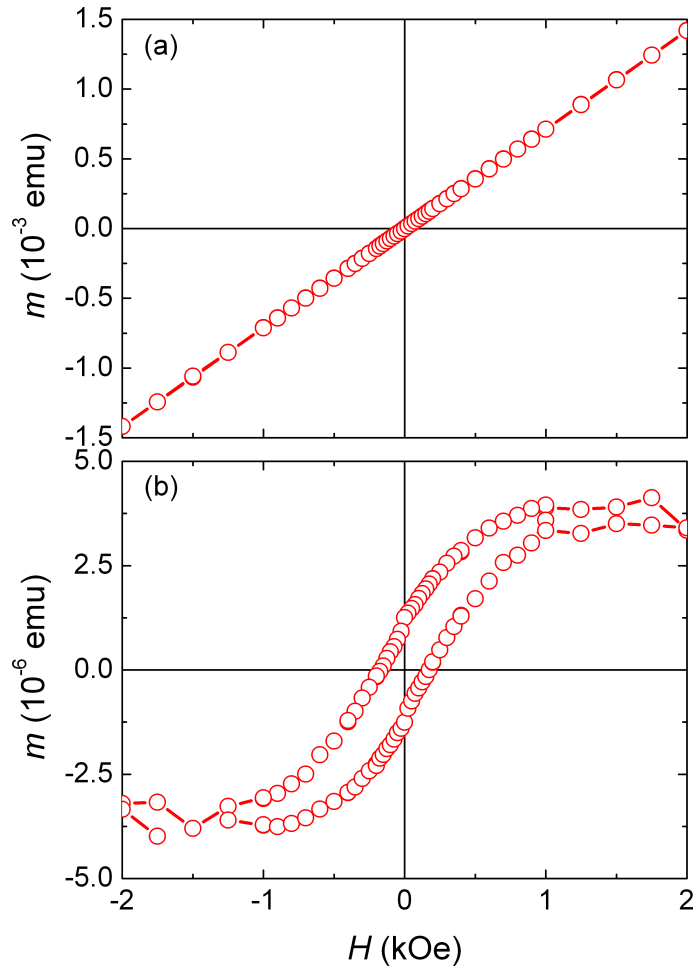


Figure 5.13: (a)  $m$  vs  $H$  loop measured at  $T = 150$  K for the piezoelectric actuator PSt 150/2×3/5 with  $H$  applied along its poling direction. (b)  $m$  vs  $H$  loop obtained from the loop in (a) after subtraction of the linear paramagnetic background.

that the magnetic response of the actuator is characterized by a strong paramagnetic component, with  $m/H \sim 7.5 \times 10^{-4}$  emu/kOe. By fitting linearly this component and subtracting it from the measured loop, the  $m$  vs  $H$  loop shown in Fig. 5.13 (b) is obtained, revealing the presence of a ferromagnetic component. This component does not vanish at  $T = 300$  K and is likely to be caused by the presence of a small amount of ferromagnetic metal impurities in the wires and

in the metallic sheets that separate the various ceramic layers in the actuator. Since at  $T = 150$  K the remanent magnetic moment of the piezoelectric actuator is non negligible if compared to the saturation moment of the piece of (Ga,Mn)As wafer cemented to it<sup>11</sup>, the magnetic properties of the latter had to be determined by carefully subtracting from the magnetic moment of the composite device not only the linear paramagnetic background generated by the actuator but also its ferromagnetic moment. This apparently straightforward procedure was found to be rather difficult, probably due to different positioning of the actuator in the measurements with and without (Ga,Mn)As. It was in fact found that, in order to obtain sensible  $M$  vs  $H$  loops for (Ga,Mn)As, it was necessary to subtract the ferromagnetic moment of the actuator corrected by a multiplying factor of value 0.75.

### 5.5.2 Effects of the piezoelectric actuator on the magnetic anisotropy

The position of the magnetic easy axis for the different voltages applied to the piezoelectric actuator was inferred from  $M$  vs  $H$  loops.  $H$  was applied along the  $[1\bar{1}0]$  direction for these measurements, although a misalignment of  $\sim 5^\circ - 10^\circ$  was found to have been accidentally introduced. Fig. 5.14 shows the  $M$  vs  $H$  loops of the (Ga,Mn)As sample for different values of  $V$ , obtained after subtracting the magnetic contribution of the actuator. It is firstly important to notice that the value of  $M_S$  in these loops is comparable to that obtained from SQUID magnetometry measurements of (Ga,Mn)As alone (see Fig. 5.4), thus conferring more credibility to the subtraction procedure used to obtain these loops. It can moreover be seen in Fig. 5.14 that the remanent magnetization along the direction of  $H$  decreases with increasing the (positive) voltage applied to the piezoelectric actuator, indicating that the magnetic easy axis rotates away from the  $[1\bar{1}0]$  direction, consistently with what observed in the magnetotransport device.

Both the orientation of the magnetic easy axis and the value of  $K_{Up}$  were obtained by fitting numerically to the regions of the  $M$  vs  $H$  loops less likely to involve magnetic domain processes<sup>12</sup> using Eq. 5.6 with the condition  $dE/d\phi = 0$ . The results of these fittings are plotted in Fig. 5.14 for some values of  $V$ , while Fig. 5.15 and Fig. 5.16 show respectively the dependence of the easy axis orientation (with respect to the  $[1\bar{1}0]$  direction) and of  $K_{Up}$  on the strain  $\Delta\epsilon$  generated by the actuator.

The strain induced by the piezoelectric actuator on the sample could not be measured, since it was not possible, due to space constraints, to glue a strain gauge

<sup>11</sup>Given that  $M_S = 36.3$  emu/cm<sup>3</sup> (see Fig. 5.4) and that the piece of wafer has dimensions  $0.25 \times 0.3 \times 25 \times 10^{-7}$  cm<sup>3</sup>, its saturation moment is  $m_S = 6.8 \times 10^{-7}$  emu.

<sup>12</sup>These regions are  $M(H = 0.5 \text{ kOe} \rightarrow 0 \text{ kOe})$  and  $M(H = -0.5 \text{ kOe} \rightarrow 0 \text{ kOe})$ .

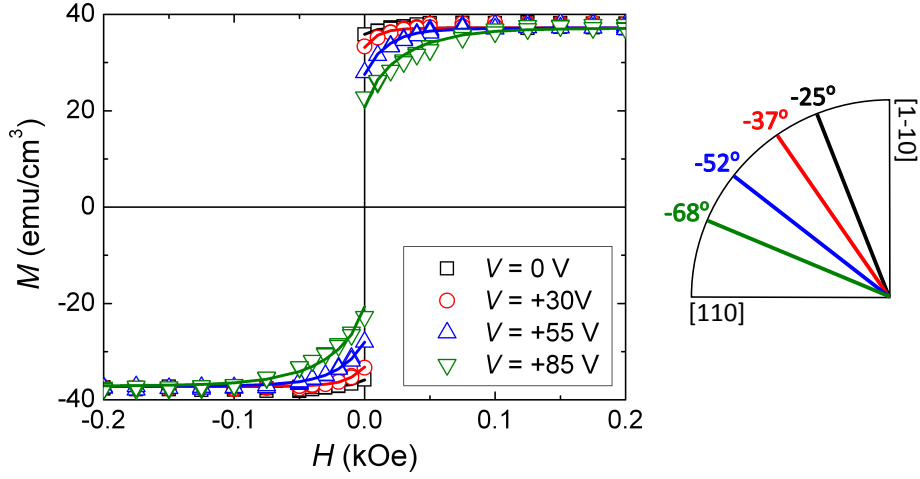


Figure 5.14:  $M$  vs  $H$  loops at  $T = 150 \text{ K}$  with  $H$  applied along the  $[1\bar{1}0]$  direction ( $\pm 5^\circ - 10^\circ$ ) for  $V = 0 \text{ V}$ ,  $V = +30 \text{ V}$ ,  $V = +55 \text{ V}$  and  $V = +85 \text{ V}$ . The symbols are the experimental data, obtained after subtracting the magnetic contribution of the actuator from the measured loops, while the solid lines are the result of their fitting with Eq. 5.6 (see text for fitting details). The diagram to the right displays the orientation of the magnetic easy axis in each case, extracted from the fittings.

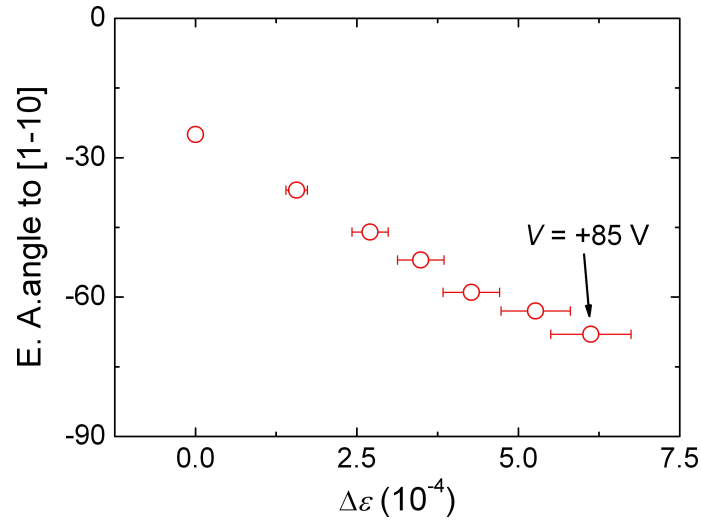


Figure 5.15: Easy axis (E. A.) orientation (with respect to the  $[1\bar{1}0]$  direction) vs  $\Delta\epsilon$  at  $T = 150 \text{ K}$ .  $\Delta\epsilon = 6.12 \times 10^{-4}$  is generated applying  $V = +85 \text{ V}$  to the piezoelectric actuator. The size of the error bars in the easy axis orientation is smaller than the size of the symbols.

on it. It was then assumed, as indicated in manufacturer specifications, that the strain generated by this piezoelectric actuator could be considered the same to within 10%, for the same applied  $V$ , to the strain generated by the piezoelectric actuator used in the magnetotransport measurements (the two samples have the same nominal thickness). This explains the large ( $\sim 10\%$ ) error bars in  $\Delta\epsilon$  that

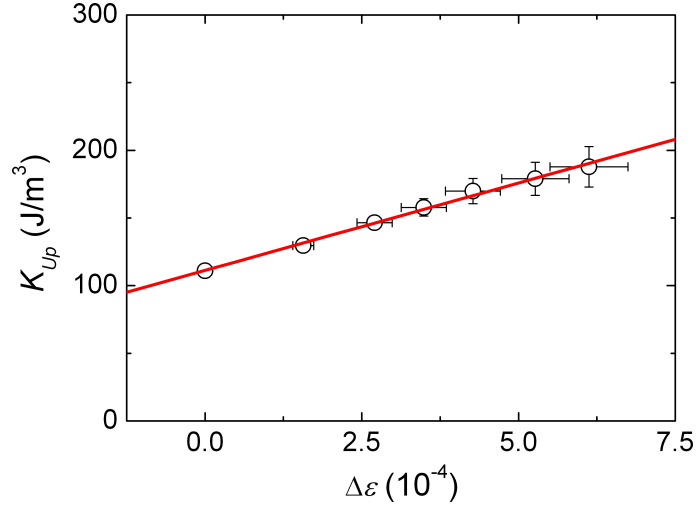


Figure 5.16:  $K_{Up}$  vs  $\Delta\epsilon$  at  $T = 150$  K. The symbols are the values extracted from the fittings of the  $M$  vs  $H$  loops, while the solid line is their linear fitting with slope of  $\sim 13$  J/m<sup>3</sup> per  $10^{-4}$  strain.

can be seen in Fig. 5.15 and Fig. 5.16. The error bars in  $K_{Up}$  are due to the combined uncertainties in  $K_U$ ,  $K_C$ , the easy axis orientation and the value of  $\delta$ , the latter being dominant, as in the magnetotransport results.

The dependence of the easy axis orientation on  $\Delta\epsilon$  is fairly linear, in evident contrast with that observed in Fig. 5.9. The magnetic easy axis rotates from  $\sim -25^\circ$  for  $V = 0$  V to  $\sim -68^\circ$  for  $V = +85$  V, a much smaller amount than that observed in the magnetotransport device. Correspondingly, the variation of  $K_{Up}$  with  $\Delta\epsilon$  is also significantly smaller: the best straight line through the points has a slope of  $\sim 13$  J/m<sup>3</sup> per  $10^{-4}$  strain, which is about half of the value obtained from the magnetotransport measurements.

## 5.6 Results comparison

The results obtained from magnetotransport and SQUID magnetometry measurements regarding the dependence of  $K_{Up}$  on strain are compared in Fig. 5.17 for convenience. The discrepancy between them is clearly rather large and this Section is devoted to describe the several factors that could be its cause.

Firstly it is important to remark that the two devices measured are different under several aspects. Not only different piezoelectric actuators and different pieces of wafer were used, but also one piece of wafer underwent a series of fabrication steps to be patterned into an Hall bar while the other one was left unpatterned. Besides, the samples might differ in the thickness by up to  $\sim 20$   $\mu\text{m}$  and this circumstance, together with the possible inhomogeneities in thickness of both the samples and the glue used to bond them to the respective actuators

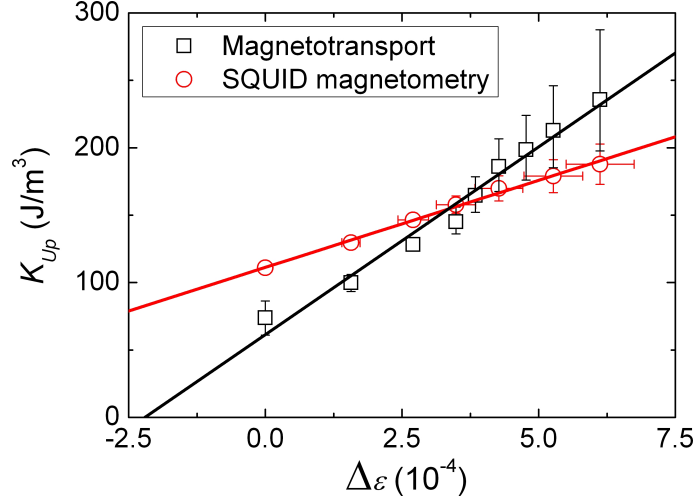


Figure 5.17:  $K_{Up}$  vs  $\Delta\epsilon$  at  $T = 150$  K. The symbols are the values derived from magnetotransport and SQUID magnetometry measurements, while the solid lines are their linear fittings with slopes of  $\sim 28$  J/m<sup>3</sup> and  $\sim 13$  J/m<sup>3</sup> per  $10^{-4}$  strain, respectively.

could account for rather different transmissions of strain from the actuators to the samples. Secondly, inhomogeneities in the generation of strain from the actuator and in its transmission to the sample result in the large SQUID sample ( $2.5 \times 3$  mm<sup>2</sup>) experiencing a much more inhomogeneous strain than the small Hall bar region ( $20 \times 50$   $\mu$ m<sup>2</sup>). In unpublished works (D. A. Allwood and P. Nemeč, private communications) polarized light microscopy has been used to show that Piezomechanik actuators are characterized by a well defined pattern of ferroelectric domains and it has been observed that the scale length of the variation of the strain induced by these actuators on a (Ga,Mn)As sample is typically quite large, thus suggesting that the inhomogeneous strain induced in the SQUID sample could be on average less than that induced in the Hall bar. This circumstance could then account for the reduction of the inverse magnetostrictive effect observed in the SQUID sample, although it would not explain why the strain induced while cooling the devices from room temperature down to  $T = 150$  K is larger in the SQUID sample than in the Hall bar. Indeed, these two aspects are difficult to reconcile. Finally, the presence of magnetic impurities in the actuator leads to some degree of experimental uncertainty in analysing the SQUID magnetometry results. After all these factors have been taken into account, the discrepancy between the two results might appear less surprising and it could be concluded that, even if SQUID magnetometry measurements are a direct way to investigate the magnetic properties of a material, the magnetotransport measurements provide a more accurate evaluation of the inverse magnetostriction effects in (Ga,Mn)As-piezoelectric actuator hybrid systems.

Further support to this conclusion was sought in the comparison of these re-

sults with those obtained from theoretical calculations. Theoretical calculations were performed by Dr. Jan Zemen using the  $\mathbf{k} \cdot \mathbf{p}$  description of the GaAs host valence band and the kinetic-exchange model of its coupling to the local Mn moments [70, 71]. Predictions of similar calculations were found to be in semiquantitative agreement with the experimental results obtained in an earlier work [41], in which the effects of a piezoelectric actuator were investigated at  $T = 50$  K on a sample of as-grown (Ga,Mn)As with nominal Mn concentration of 6%. However, the same agreement could not be obtained for the results presented in this Chapter since this theoretical model predicts a perpendicular-to-plane magnetic easy axis [77] for hole densities as high as those occurring in this (Ga,Mn)As sample ( $p \sim 1.8 \times 10^{21} \text{ cm}^{-3}$ ), which has never been observed experimentally. The only agreement that could be found between the experimental results and the theory is the linear dependence of  $K_{Up}$  with strain [77], which has though been obtained in both magnetotransport and SQUID magnetometry measurements. Hence, unfortunately, theoretical calculations could not help in confirming the supposed higher reliability of the magnetotransport technique over the SQUID magnetometry technique in interpreting the results of this Chapter.

## 5.7 Conclusions

This Chapter has shown that effective electrical control of the magnetic properties in the ferromagnetic semiconductor (Ga,Mn)As is possible using the strain induced by a piezoelectric actuator, even in the limit of high doping levels and high Curie temperatures, where direct electric gating is not possible.

SQUID magnetometry measurements were initially performed on the material alone to characterize it magnetically. It was found that its  $T_C$  is as high as 180 K and that its magnetic anisotropy is dominated by the uniaxial contribution, resulting in the magnetic easy axis lying along the  $[1\bar{1}0]$  direction at all temperatures. Two devices were prepared for magnetotransport and SQUID magnetometry measurements. They consisted of two (Ga,Mn)As samples, one patterned into a Hall bar and one left unpatterned, respectively, that were glued on top of two piezoelectric actuators, after thinning their substrate down to roughly 190  $\mu\text{m}$ . The measurements were all performed at a much higher temperature (150 K) than previous investigations, where larger strains can be generated by the actuators [128]. Both measurements revealed that large and reversible rotations of the magnetic easy axis can be achieved in this material by varying the voltage applied to the piezoelectric actuators, i.e. the strain that they induce on the samples. This result demonstrates the clear advantage of strain-mediated control over direct electric field control of magnetism in samples with high hole concentrations, for which the latter is ineffective.

The reorientation of the easy axis upon variation of the actuator voltage and the corresponding variation of the piezo-induced uniaxial magnetic anisotropy constant  $K_{Up}$  with strain were found to be larger in the Hall bar sample than in the SQUID sample. In particular, after careful analysis of both sets of data, it was found that  $K_{Up}$  varies by  $\sim 28 \text{ J/m}^3$  and  $\sim 13 \text{ J/m}^3$  per  $10^{-4}$  strain in, respectively, the Hall bar sample and the SQUID sample. This large discrepancy could be ascribed to several factors, including the possible presence of differences between the two samples and actuators used, as well as possible larger inhomogeneity in strain experienced by the larger SQUID sample. The latter circumstance alone would in fact result in a reduction of the inverse magnetostrictive effect, which is indeed observed experimentally. Taking this into account, together with the uncertainty derived from the presence of magnetic impurities in the actuator, it would appear that magnetotransport measurements provide a more accurate evaluation of the inverse magnetostriction effects in (Ga,Mn)As-piezoelectric actuator hybrid systems. Unfortunately theoretical calculations performed to try to support this conclusion did not prove useful as they failed to reproduce the dominant magnetic anisotropy of the samples at this high temperature.

# Chapter 6

## Fast switching of the magnetization in (Ga,Mn)(As,P) using phonon pulses

### 6.1 Introduction

As discussed throughout this Thesis, one of the most appealing aspects of DMS is represented by the opportunity that they offer to use non-magnetic parameters to manipulate their magnetic state, thus potentially allowing to overcome the problems currently encountered in the use of magnetic fields to write information in magnetic memories [42]. The use of electric fields [33, 34], electric currents [35, 36], light [37, 38] and strain [39, 40, 41] have indeed all been proven to be successful strategies to manipulate the magnetization in DMS. However, in order for these strategies to acquire technological relevance, a crucial requirement is that the manipulation of the magnetization has to be realized on ultrashort time scales, as is the case for metallic-based spintronic devices [136, 137].

In the past decade fast magnetization dynamics have been widely investigated in (Ga,Mn)As samples using ultrashort light pulses and both magnetic anisotropy modulation [138, 139, 140] and magnetization switching [141] have been demonstrated to be possible. This approach relies on the light-induced variation of the hole concentration (non-thermal effect) and/or of the lattice temperature (thermal effect), that in turn modifies the magnetic anisotropy. But even when the faster non-thermal effect is dominant, the magnetic system is normally found to respond relatively slowly, the cooling down process of the photoexcited holes being the limiting factor [139]. For this reason, using strain pulses rather than optical pulses to avoid the direct involvement of the holes in the process, could in principle allow for faster manipulation of the magnetic anisotropy of (Ga,Mn)As. Adding to this the fact that (Ga,Mn)As is characterized by large inverse mag-

netostriction coefficients, as it has been evidenced throughout this Thesis, the reasoning behind using this approach becomes even stronger.

The interaction between lattice vibrations and spin waves was predicted in 1958 by Kittel [142] and since then it has been experimentally investigated in a range of ferromagnetic metals [143], with a focus on the effects encountered when magnetoacoustical resonance occurs ( $\omega_{\text{phonon}} = \omega_{\text{magnon}}$  and  $\lambda_{\text{phonon}} = \lambda_{\text{magnon}}$ ). Propagation of acoustic waves has been long studied also in DMS [144, 145] but not with the aim of analysing the effects of these waves on the magnetic properties of DMS. Indeed the strain applied to control the magnetization in DMS has always been static until very recently (2010), when the first two time-resolved experiments on the use of ultrashort strain pulses to change the magnetic properties of (Ga,Mn)(As,P) and (Ga,Mn)As were published [146, 147]. While in the work by Thevenard *et al.* [146] the experimental observations were interpreted as a consequence of the strain-modulated reflectivity of the magnetic layer, ruling out the presence of any inverse magnetostriction phenomenon, the work by Sherbakov *et al.* [147] clearly proved that ultrashort strain pulses can be effectively used to induce a coherent precession of the magnetization at a frequency of  $\sim 10$  GHz. These results were ascribed to the strain-pulse-induced transient variation of the magnetic anisotropy of (Ga,Mn)As. A following experimental work [148] showed that ultrashort strain pulses can also be used to selectively excite single spin wave modes, a circumstance occurring for phonon and magnon wavefunctions spatially overlapping. Finally, a theoretical study was published [149] describing how the effects of the ultrashort strain pulses on the magnetic anisotropy of (Ga,Mn)As depend on the material parameters, the strain pulse parameters and the magnetic field direction and strength.

Despite the undoubted importance of the results already achieved with this novel technique, it would be favourable from a technological point of view to use ultrashort strain pulses to trigger a switch rather than a precession of the magnetization. Strain-pulse-driven magnetization switching has been successfully reported on an array of  $\mu\text{m}$ -wide Co bars using a surface acoustic wave (SAW) transducer [150], but has not been obtained in DMS yet.

This Chapter presents the results of an experimental investigation attempting to use ultrashort strain pulses to switch the magnetization direction of an as-grown 100 nm thick layer of  $(\text{Ga}_{0.94}\text{Mn}_{0.06})(\text{As}_{0.91}\text{P}_{0.09})$  (Mn591). Even though it will be shown that the magnetization does indeed switch between two different easy axis orientations as a consequence of the acoustic excitation, time-resolved measurements will prove that the switching is triggered by incoherent phonons (heat pulses) rather than the more desirable coherent phonons (strain pulse), and is a relatively slow process. Most of the results discussed in this Chapter were published in [151].

## 6.2 Experimental method

### 6.2.1 Overview

Methods using phonons as a spectroscopic tool have long been well known. Measurements of heat capacity and thermal conductivity [152] were among the first ones to provide information relating to phonon spectroscopy, especially in non-metallic systems, in which the conduction of heat occurs exclusively via phonons. But given the broad thermal distribution of the phonon energies and the static nature of the measurements, the information that could thus be obtained was unavoidably averaged over the different phonons frequencies and polarisations. Time- and space-resolved measurements of nonequilibrium phonons became possible thanks to the introduction of the heat-pulse method in 1964 [153].

Heat pulses are nonequilibrium phonon pulses of nanosecond duration with typical frequency components between 1 GHz and 1 THz and random phase. They are usually generated by fast (1–100 ns) electrical or optical excitation of a thin metal film deposited on a polished face of the sample under investigation. The temperature of the film raises rapidly ( $\sim 1$  ns) and its excited electrons relax by radiating phonons into the sample along all direction. If complete thermalisation between electrons and phonons in the metal film occurs, as it is often the case, then the frequency spectrum of the emitted phonons has a thermal Planck distribution [154], approximately centred around the frequency  $k_B T/h$ , where  $k_B$  and  $h$  are the Boltzmann constant and the Planck constant, respectively. At low temperatures and in a crystal sufficiently free of defects these phonons can travel ballistically<sup>1</sup> over millimetre distances [155], thus exceeding the normal sample length. The rise in temperature due to the arrival of the phonons on the opposite face of the sample is monitored via the corresponding change in resistance of, typically, a thin film superconducting detector (a bolometer or a tunnel junction) deposited on it. These detectors are characterized by extremely small heat capacities, thus allowing for rapid variations of temperature to be registered. If the sample is long enough, several sharp peaks delayed in time after the excitation pulse can be distinguished, each followed by long tails due to the phonons that reach the detector only after having been scattered. These peaks correspond to the different phonon polarisations that, due to the anisotropic nature of the elasticity in crystals, travel through the sample with different group velocities: compression and shear phonon waves travel with the longitudinal and transverse sound velocity, respectively. Phonon focussing<sup>2</sup> and polarisation-dependent scattering cause the relative magnitudes of the different peaks to depend on the

---

<sup>1</sup>The phonon propagation becomes instead diffusive at high temperatures as a consequence of the phonon-phonon scattering mechanism.

<sup>2</sup>Ballistic phonons generated from a localized heat source are channelled along preferential crystal directions due to elastic anisotropies.

propagation direction with respect to the crystallographic axes [156]. When the excitation of the metal film occurs via a pulsed laser, it is then possible to obtain a spatial map of the distribution of the phonons flux in the sample by scanning the laser spot on the metal film. Since its development in 1979 [157] this technique, known as phonon imaging, has played a major role in heat-pulse experiments.

With the advent of picosecond and femtosecond pulsed lasers, phonon pulse experiments have been extended into the picosecond temporal region through the development of picosecond ultrasonics [158]. This method, that was first proposed by Thomsen *et al.* in 1984 [159], is similar to the heat-pulse method in that it also consists of the excitation of a thin metal film deposited on a polished face of the sample. In this case though, the excitation occurs via ps or fs laser pulses and the corresponding raise in temperature of the metal film occurs in  $\sim 1$  ps. As a result, a strain pulse of picosecond duration with typical frequency components up to 200 GHz is launched into the sample. Differently from heat pulses, strain pulses are coherent nonequilibrium phonon pulses. Moreover, when generated in this way, they do not propagate in all directions within the sample but just along the direction perpendicular to the metal film surface. If this direction is a high symmetry crystallographic direction, strain pulses contain only longitudinal components and thus travel with the longitudinal sound velocity. At low temperatures and in a crystal sufficiently free of defects strain pulses travel ballistically, as heat pulses, over millimetre distances [160]. Since strain pulses modulate the dielectric constant and hence the reflectivity of the sample, they are conventionally detected measuring the intensity of a laser beam (the probe) incident on the sample surface opposite the metal film with a time-delay with respect to the generating pulse (the pump). This optical detection technique is known as pump-probe spectroscopy.

The picosecond ultrasonics technique was used for the experiment described in this Chapter. Intense 60 fs laser pulses were incident on a 120 nm thick Al film deposited on the back of the 350  $\mu\text{m}$  thick GaAs(001) substrate of (Ga,Mn)(As,P) sample Mn591, and a picosecond-duration strain pulse followed by nanosecond-duration heat pulses were thus generated. In GaAs there are three acoustic phonon branches<sup>3</sup>, one longitudinal and two transverse. Along high symmetry crystallographic directions, as the (001) of the experiment, the strain pulse contains only longitudinal components, while the two transverse heat pulses are degenerate. Since the experiment was performed at superfluid He temperatures, both the strain pulse and the heat pulses travel ballistically through the GaAs substrate with the longitudinal and transverse sound velocities, respectively  $v_l = 4.8$  km/s and  $v_t = 3.4$  km/s. The arrival of the pulses at the (Ga,Mn)(As,P)

---

<sup>3</sup>In GaAs there are also three optical phonon branches, but they do not propagate since they decay quickly after being generated.

film on the other side of the substrate was detected electrically by measuring the change in resistance of the film, patterned into a Corbino disk geometry.

### 6.2.2 Strain pulse characteristics

The spatial-temporal functional form of a strain pulse  $\epsilon(t, z)$  generated via the picosecond ultrasonics technique described above can be approximated as [161]:

$$\epsilon(t, z) = \frac{\sqrt{e}\epsilon^{\max}}{\tau} \operatorname{sgn}(t - z/v_l) \exp\left(-\frac{(t - z/v_l)^2}{2\tau^2}\right), \quad (6.1)$$

where  $e$  is the base of the natural logarithm,  $\epsilon^{\max}$  is the pulse amplitude,  $\tau$  is the pulse duration and  $\hat{z}$  is the propagation direction, perpendicular to the metal film. The values of  $\epsilon^{\max}$  and  $\tau$  depend on the parameters of the optical excitation and on the type of metal film that generates the pulse. For  $\sim 100$  fs laser pulses and Al films they have typical values of  $\sim 10^{-3}$  and  $\sim 10$  ps, respectively. The temporal profile of the strain pulse  $\epsilon(t, z)$  with these values of  $\epsilon^{\max}$  and  $\tau$  is showed in Fig. 6.1 for  $z = 0$  (although it is the same for any other value of  $z$ ). It is easy to understand from Fig. 6.1 that a strain pulse is composed of a

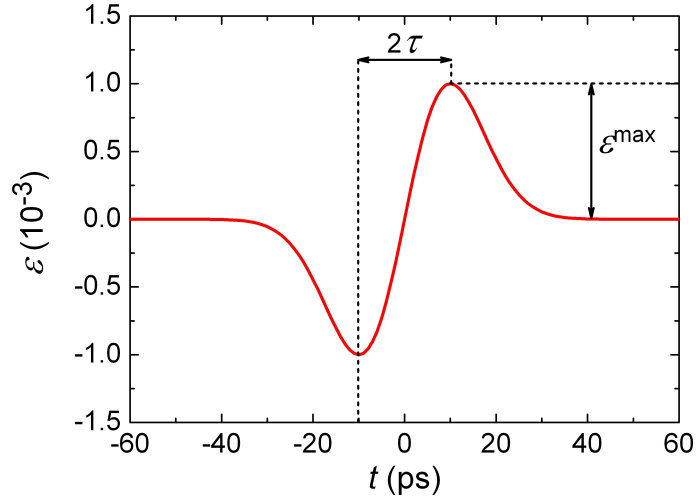


Figure 6.1: Temporal profile of the strain pulse  $\epsilon(t, z)$  with  $\epsilon^{\max} = 10^{-3}$ ,  $\tau = 10$  psec and  $z = 0$ .

compressive component followed by a tensile component. Hence, if the sample under investigation is a thin film deposited on the surface of a substrate material opposite the metal film, its thickness  $d$  will be modulated by the strain pulse travelling through it. This modulation  $\Delta d(t)/d$ , which corresponds to the strain

profile averaged over  $d$ ,  $\epsilon_{\text{ave}}(t)$ , can be evaluated as:

$$\frac{\Delta d(t)}{d} \equiv \epsilon_{\text{ave}}(t) = \frac{1}{d} \int_0^d \epsilon(t, z) dz = \frac{\sqrt{\epsilon} \epsilon^{\text{max}}}{\tau d} \int_0^d \left[ (t - z/v_l) \exp\left(-\frac{(t - z/v_l)^2}{2\tau^2}\right) - (t + (z - 2d)/v_l) \exp\left(-\frac{(t + (z - 2d)/v_l)^2}{2\tau^2}\right) \right], \quad (6.2)$$

where  $z = 0$  corresponds to the interface between the substrate and the sample. The first term in Eq. 6.2 represents the strain pulse propagating towards the open surface, while the second term represents the strain pulse propagating back towards the substrate, after having been reflected at the open surface with a  $\pi$ -phase shift. Non-linear effects, which would modify the shape of the strain pulse during propagation, have not been taken into account.  $\epsilon_{\text{ave}}(t)$  obtained using  $\epsilon^{\text{max}} = 10^{-3}$ ,  $\tau = 10$  ps and  $v_l = 4.8$  km/s, the latter being valid in GaAs, is plotted in Fig. 6.2 for different values of  $d$ . Looking at Fig. 6.2, it can be

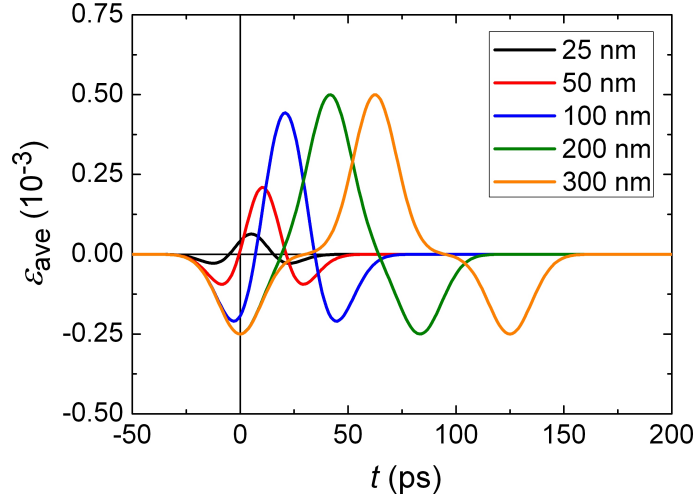


Figure 6.2: Temporal profile of the average strain  $\epsilon_{\text{ave}}$  with  $\epsilon^{\text{max}} = 10^{-3}$ ,  $\tau = 10$  psec and  $v_l = 4.8$  km/s, for different values of the sample thickness  $d$ .

seen that the strain pulse results in an initial compression of the sample, followed by an expansion of it, of roughly double amplitude, in turn followed by a final compression, of identical amplitude to the first one. It is moreover evident that the amplitude of this compressive-tensile-compressive train of perturbations is dramatically reduced for sample thicknesses  $\lesssim 100$  nm, as a consequence of the destructive interference between the strain pulse travelling towards the open surface and back away from it. When probing the possible variation of the magnetic properties of a sample as a consequence of the strain pulse travelling through it, the result provides information averaged over the sample thickness, since it is not possible to detect the magnetization orientation at a specific value of  $z$ . For this reason the relevant experimental parameter is the average strain  $\epsilon_{\text{ave}}$ , rather

than the strain  $\epsilon(t, z)$ , and in order to maximize its amplitude it is important to work with samples at least 100 nm thick. In this way, according to Fig. 6.2,  $\epsilon_{\text{ave}}$  values up to  $\sim 4 \times 10^{-4}$  can be obtained in GaAs, large enough to manipulate the magnetic anisotropy in (Ga,Mn)As, as it has been shown in Chapter 5.

### 6.3 Experimental set-up and details

The diagram of the set-up used in the experiment is shown in Fig. 6.3. 60 fs

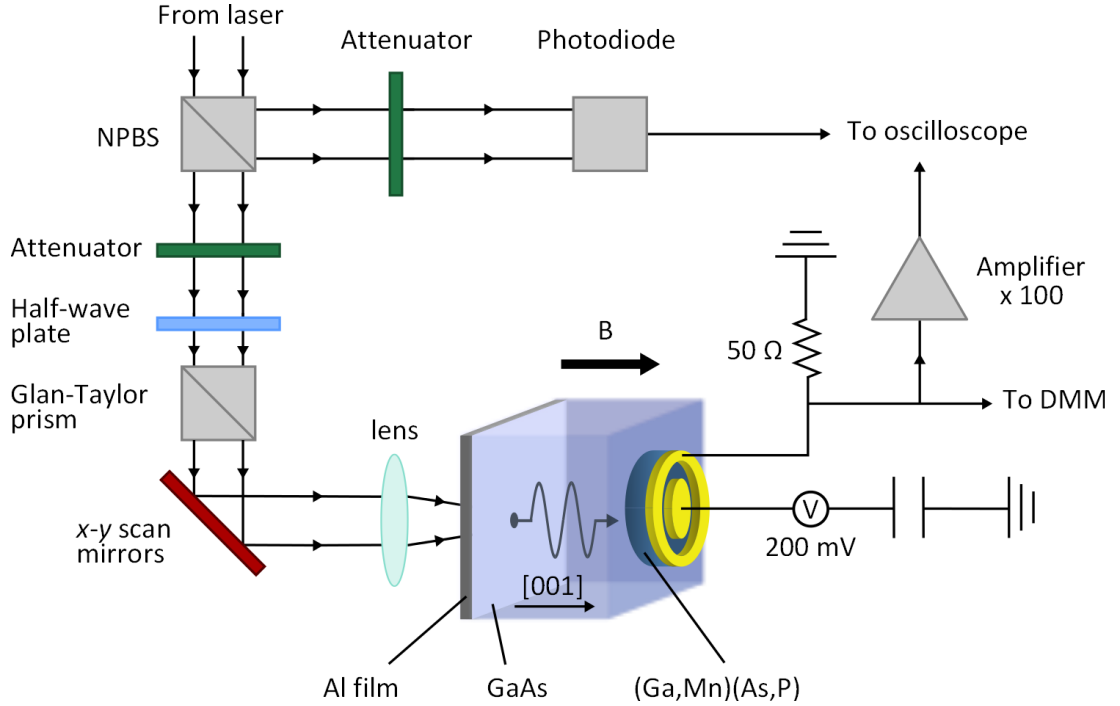


Figure 6.3: Diagram of the experimental set-up used: strain and heat pulses were generated optically and detected electrically. The resulting signal was read by a digital multimeter (DMM) or an oscilloscope, depending on whether static or time-resolved measurements, respectively, were performed.

optical pulses of  $\lambda = 800$  nm were generated by a Spectra-Physics amplified Ti:Sapphire laser, which can be operated either in single pulse or continuous pulses mode, with repetition rate up to 5 kHz. A non-polarizing beam splitter (NPBS) placed at the laser exit split the laser beam in two. One beam passed through a neutral density filter and reached a photodiode, which correspondingly sent a trigger signal to the oscilloscope. The second beam, after having been attenuated by a neutral density filter too, travelled through a half-wave plate and a Glan-Taylor prism, the combination of which was used as a further variable attenuator, and was then focussed to a spot of radius of about 100  $\mu\text{m}$  on the Al film. The position of the excitation spot on the film was set using galvanometer  $x-y$  scanning mirrors. The measurements were mostly performed with an energy

density per pulse  $J$  of about  $12 \text{ mJ/cm}^2$ , since higher values were found to damage the Al film. The sample was mounted in the Oxford Instruments Spectromag 3 (MD-10) optical-access cryostat of the School of Physics and Astronomy in the University of Nottingham, which functions similarly to the Oxford Instruments He-4 Variox cryostat described in Section 3.3.2. During the measurements the sample was immersed in superfluid liquid He at a constant temperature of about 1.7 K. Superfluid liquid He was used to both prevent the formation of bubbles in the optical path and to provide good temperature stability during optical excitation. In fact, the increase in the sample temperature is expected to be no more than a few mK [155] with the laser in continuous pulses mode at 5 kHz and negligible for single pulses. The temperature was kept constant using a manostat, that works by keeping the pressure constant in the sample space, and was measured using an Allen-Bradley resistor. The cryostat is equipped with an Oxford Instruments Spectromag-3 7 Tesla superconducting magnet. In the experiment this magnet was used to generate magnetic fields up to 100 mT along the direction perpendicular to the sample plane. The sample was lithographically patterned into a Corbino disk geometry with inner  $r_1$  and outer  $r_2$  contact radii of 90  $\mu\text{m}$  and 97  $\mu\text{m}$ , respectively (see Fig. 3.1). The direction of the magnetization in the sample was inferred measuring the resistance of the Corbino disk, biased with a DC voltage of 200 mV. The signal thus obtained was sent either to a digital multimeter (DMM) or, after having been amplified, to the oscilloscope, depending on whether static or time-resolved measurements, respectively, were performed. The oscilloscope is a Tektronix DPO71254 oscilloscope, characterized by a 12.5 GHz bandwidth and a 50 GS/s sampling rate. Sourcemeater, multimeter and oscilloscope were all controlled by a Visual Basic interface.

The Corbino disk geometry with a small annulus was chosen to obtain a small value of the resistance, which is a key requirement to achieve good temporal resolution in electrical detection measurements<sup>4</sup>. The relationship between the Corbino resistance  $R$  and the material longitudinal resistivity  $\rho_{xx}$  is given by [162]:

$$R = \frac{\rho_{xx}}{2\pi d} \ln \frac{r_2}{r_1}, \quad (6.3)$$

where  $d = 100 \text{ nm}$  is the sample thickness. Then, by choosing a  $r_2/r_1$  ratio close to 1, it was possible to obtain a Corbino resistance of a few tens of  $\Omega$ , despite the typically high values of the longitudinal resistivity of as-grown (Ga,Mn)As (and (Ga,Mn)(As,P)) samples, particularly at low temperatures.

Since in a Corbino disk the current flows radially across the annulus, the non-crystalline contribution to the in-plane AMR of Eq. 2.10 is averaged to zero [93].

---

<sup>4</sup>Preliminary experiments performed on samples patterned into standard-size Hall bars (see Fig. 3.1), in which the direction of the magnetization was inferred from AHE measurements, had poor temporal resolution due to the large values of the Hall bars resistance.

It follows that changes in the in-plane AMR in a Corbino disk geometry are intrinsically difficult to detect, because they are determined only by the crystal-line contributions, that roughly represent 10% of the total in-plane AMR [93]. The Corbino disk geometry is instead more appropriate to detect changes in the out-of-plane AMR (see Eq. 2.5). For this reason it was decided to work with (Ga,Mn)(As,P) rather than (Ga,Mn)As. Moreover, from symmetry considerations it can be understood that the resistance of a Corbino disk is the same when  $M$  is parallel or anti-parallel to the perpendicular-to-plane direction. Hence a Corbino disk cannot be used to detect switching of the magnetization between these two states that occur in (Ga,Mn)(As,P) samples with perpendicular magnetic anisotropy, like annealed Mn498 and Mn403. It can though be used to detect switching of the magnetization from an (almost) in-plane direction to the perpendicular-to-plane direction and vice-versa that occur in as-grown Mn498 and Mn403, due to the peculiar shape of their [001] magnetic hysteresis loop (see Fig. 4.4). Given the small thickness of their (Ga,Mn)(As,P) layer, neither Mn498 nor Mn403 were appropriate for the present experiment, as explained in the previous section, and 100 nm thick Mn591 was then grown, with nominal Mn and P concentrations  $x = 6\%$  and  $y = 9\%$ , respectively, as for Mn498.

The alignment between the laser excitation spot on the Al film and the Corbino disk sample on the other side of the substrate was obtained monitoring the amplitude of the induced  $R$  variation while scanning the spot over the Al film with the  $x - y$  mirrors.

## 6.4 Material characterization

### 6.4.1 XRD measurements

XRD  $\omega - 2\theta$  scans at the GaAs (004) peak were performed on as-grown Mn591 by Dr. Peter Wadley and are shown in Fig. 6.4 with the corresponding fittings. The sharp peak in Fig. 6.4 represents the reflection from the GaAs substrate, while the broader peak, marked with the dashed vertical red line, represents the reflection from the (Ga,Mn)(As,P) film. Since the latter is located at a higher angle than the former, it can be concluded that the (Ga,Mn)(As,P) film is under in-plane tensile strain, as it has been explained in Chapter 4. The experimental data were fitted to extract the values of the effective phosphorus concentration  $y_{eff}$  and of the perpendicular lattice constant  $a_{\perp}$ . Since no control sample was grown for Mn591, the fitting was done assuming that the concentration of substitutional and interstitial Mn atoms in Mn591 is the same as in the control sample of the Mn491–Mn492–Mn498 series. In this way  $y_{eff} = 11.1\%$ , close to the nominal  $y = 9\%$ , and  $a_{\perp} = 5.64606 \text{ \AA}$  were obtained, and using Eq. 4.2 the in-built growth

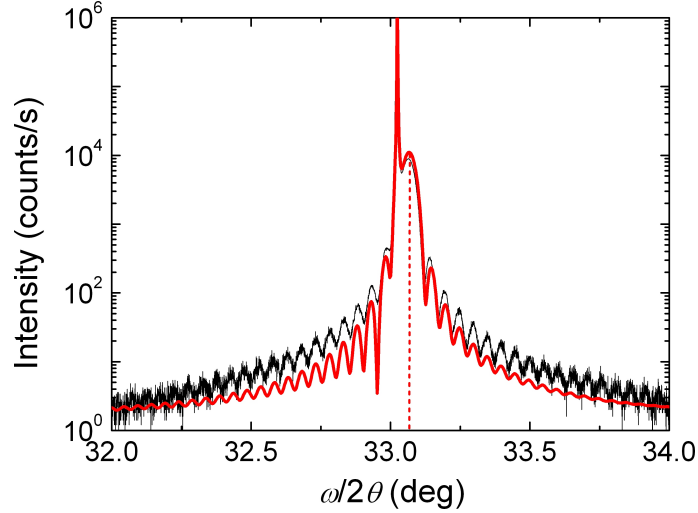


Figure 6.4: XRD  $\omega - 2\theta$  scans at the GaAs (004) peak for as-grown Mn591. The black and red line are the experimental data and their fittings, respectively. The dashed vertical red line marks the approximate position of the  $(\text{Ga},\text{Mn})(\text{As},\text{P})$  (004) reflection.

strain  $\epsilon$  was then estimated to be  $\sim -0.13\%$ .

### 6.4.2 SQUID magnetometry measurements

SQUID magnetometry measurements were performed on both as-grown and annealed Mn591 using the magnetometry system described in Section 3.3.1 and following the procedures presented there.

Fig. 6.5 shows  $M_R$  vs  $T$  curves measured for as-grown Mn591 along in-plane and perpendicular-to-plane directions. These measurements show that as-grown Mn591 is characterized by in-plane magnetic anisotropy over the whole temperature range up to  $T_C = 51$  K. This is consistent with what is expected in samples under in-plane tensile strain with a very low hole concentration [71], and it was also found to occur in as-grown Mn403 (see Fig. 4.5). Moreover, it can be seen from Fig. 6.5 that the temperature dependence of the various in-plane anisotropy contributions is the same as that observed for the  $(\text{Ga},\text{Mn})(\text{As},\text{P})$  samples with in-plane magnetic anisotropy and  $y < 10\%$  investigated in Chapter 4, with the dominant anisotropy contribution changing from cubic to uniaxial upon increasing the temperature, and with the uniaxial anisotropy contribution favouring the  $[110]$  and  $[1\bar{1}0]$  direction at low and high temperatures, respectively.

Fig. 6.6 shows  $M$  vs  $H$  loops measured at  $T = 2$  K for as-grown Mn591, with  $H$  applied along in-plane and perpendicular-to-plane directions. Beside confirming the occurrence of in-plane magnetic anisotropy in as-grown Mn591 at  $T = 2$  K, these measurements show that the hard axis  $[001]$   $M$  vs  $H$  loop is characterized by the non-linear behaviour already observed in as-grown Mn498 and Mn403, which

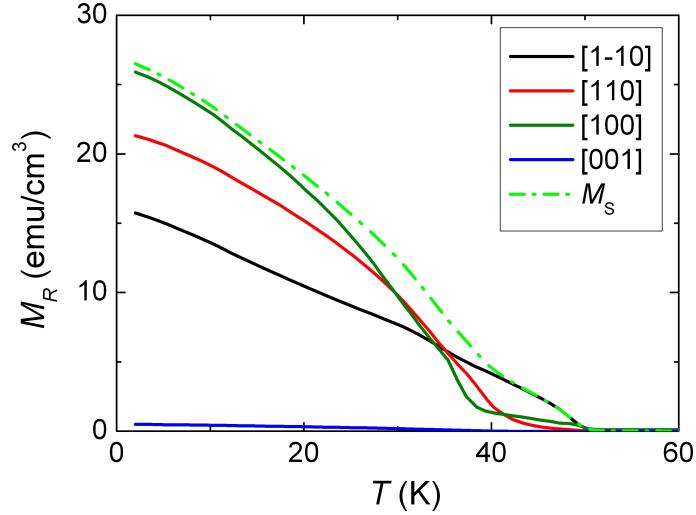


Figure 6.5:  $M_R$  vs  $T$  curves measured for as-grown Mn591 along the in-plane  $[1\bar{1}0]$  (black),  $[110]$  (red) and  $[100]$  (solid dark green) directions and the perpendicular-to-plane  $[001]$  (blue) direction. The saturation magnetization  $M_S$  (dashed light green) is calculated according to the Stoner-Wohlfarth single-domain model (Eq. 3.1).

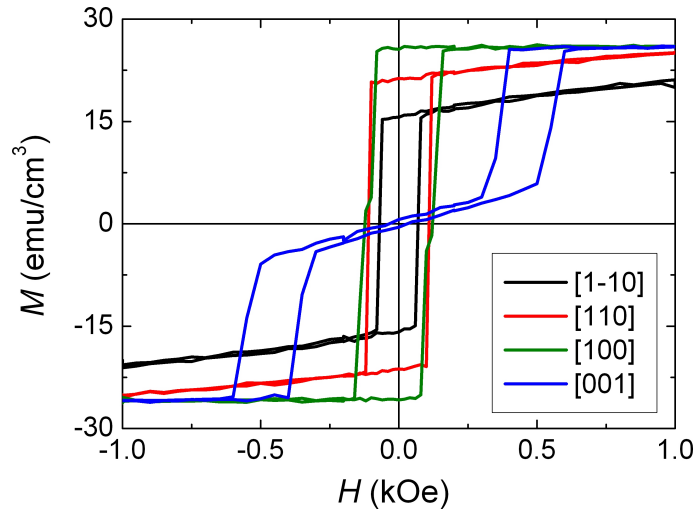


Figure 6.6:  $M$  vs  $H$  loops measured at  $T = 2$  K for as-grown Mn591, with  $H$  applied along the in-plane  $[1\bar{1}0]$  (black),  $[110]$  (red) and  $[100]$  (green) directions and the perpendicular-to-plane  $[001]$  (blue) direction.

can be explained in terms of the competition between magnetocrystalline, strain and shape anisotropy. Of particular importance for the experiment described in this Chapter is the presence in the  $[001]$  loop of the two open sections at large values of  $|H|$ , where the magnetization switches from an almost in-plane direction to the perpendicular-to-plane direction and vice-versa. These switches can in fact be detected measuring the resistance of the Corbino disk, as already explained.

Even if not strictly relevant for the present experiment, it is nonetheless good

to mention for completeness that SQUID magnetometry measurements performed on annealed Mn591 revealed that the sample is characterized by perpendicular-to-plane magnetic anisotropy over the whole temperature range up to  $T_C = 110$  K, as expected, and  $M_S$  at  $T = 2$  K was found to be  $37.9 \text{ emu/cm}^3$ .

### 6.4.3 Transport measurements

Four terminal transport measurements were performed on as-grown Mn591 using the transport system described in Section 3.3.2 and following the procedures presented there. For these measurements the sample was patterned into the Hall bar geometry of Fig. 3.1.

Fig. 6.7 shows the dependence of the longitudinal resistivity  $\rho_{xx}$  on temperature for as-grown Mn591. As for as-grown Mn498, this dependence is character-

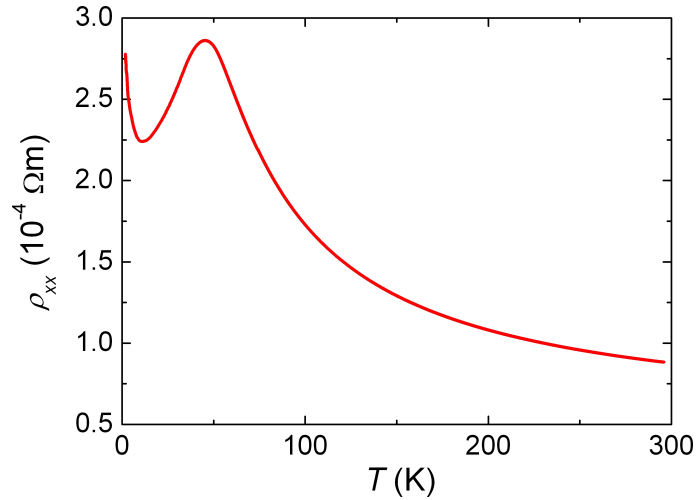


Figure 6.7:  $\rho_{xx}$  vs  $T$  curve for as-grown Mn591.

ized by features typical of metallic ferromagnetic (Ga,Mn)As [32, 84]: the initial increase of  $\rho_{xx}$  for decreasing  $T$  from room temperature is followed by a peak at  $T \simeq 45$  K, then by a decrease as  $T$  is decreased below  $\simeq 45$  K, and finally by a further increase for  $T \lesssim 11$  K due to weak localization effects [87]. Not only its dependence on  $T$ , but also the magnitude of  $\rho_{xx}$  of as-grown Mn591 is comparable to that of as-grown Mn498, being higher than the latter by just a factor of 1.3–2.1. Even without reaching the extremely high values observed for as-grown Mn403,  $\rho_{xx}$  of as-grown Mn591 is high enough to account for its in-plane magnetic anisotropy. At  $T = 1.7$  K  $\rho_{xx} = 2.8 \times 10^{-4} \Omega\text{m}$  and the corresponding Corbino disk resistance  $R$ , estimated using Eq. 6.3, is of just  $\sim 33 \Omega$ . Such a small value of  $R$  has allowed the achievement of a good temporal resolution in the detection of strain and heat pulses, as it will be shown in the next Sections.

Since in a Corbino disk geometry only two terminal transport and magneto-transport measurements can be performed, any measurement of the resistance

of a Corbino disk will always include a contribution from the interface between the ferromagnetic semiconductor and the metal contacts. As will become clear in the following, in order to correctly interpret the experimental results it is important to establish whether and to what extent this contribution changes with temperature. Fig. 6.8 shows the dependence of the resistance of the Corbino disk of as-grown Mn591 on temperature. The fact that this dependence closely

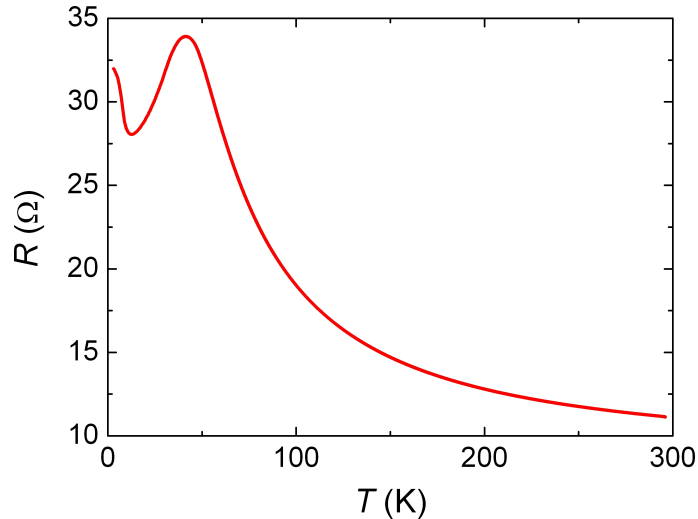


Figure 6.8:  $R$  vs  $T$  curve for the Corbino disk of as-grown Mn591.

resembles the dependence of the longitudinal resistivity on temperature shown in Fig. 6.7 suggests that the resistance of the interface with the metal contacts represents just a small contribution to the resistance of the Corbino disk and consequently that its dependence on temperature is negligible. This is indeed reasonable, given that the the area of the interface between (Ga,Mn)(As,P) and the metal contacts is much larger than the area of the annular region and has also been shown to be the case for metal contacts deposited on (Ga,Mn)As Corbino disks [93].

#### 6.4.4 MOKE imaging measurements

MOKE imaging measurements were performed on as-grown Mn591 using the MOKE imaging system described in Section 3.3.3 and following the procedures presented there.

Fig. 6.9 shows polar MOKE images of different regions of a Hall bar of as-grown Mn591 taken at  $T = 4.2$  K and at  $H = -0.5$  kOe along the upper branch of the hysteresis loop (the [001] loop in Fig. 6.6). The magnetic contrast in Fig. 6.9 was enhanced by digitally subtracting from the original image, an image taken on the same area of the Hall bar at  $H = +1$  kOe, i.e. at saturating field. The dark and light grey stripes 3 – 4  $\mu\text{m}$  wide that can be seen in the Hall bar in Fig. 6.9

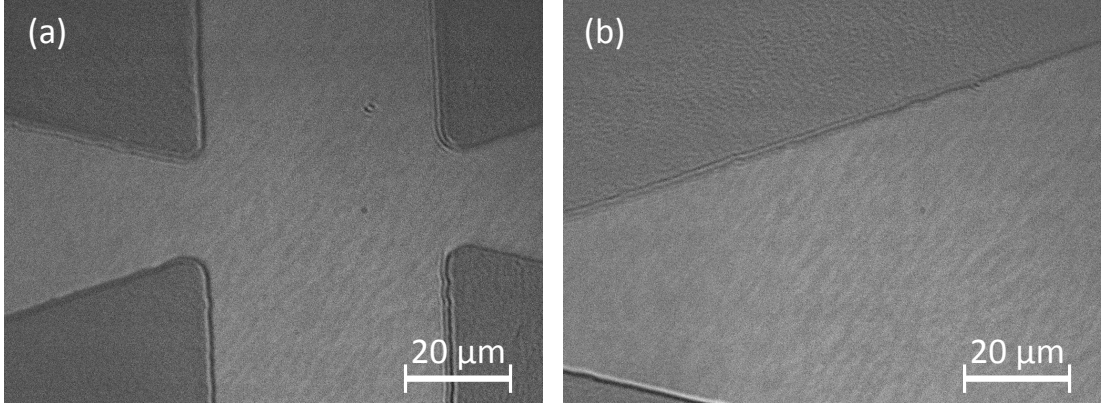


Figure 6.9: Polar MOKE images of (a) the channel and (b) a voltage probe of a Hall bar of as-grown Mn591 taken at  $T = 4.2$  K and at  $H = -0.5$  kOe along the upper branch of the [001] hysteresis loop shown in Fig. 6.6.

are magnetic domains respectively characterized by  $M$  lying at a small angle to the plane and perpendicular to it, along the direction of  $H$ . Magnetic domains could not be clearly observed in the Corbino disk used in the experiment due to the small dimension of its annular region, but it is reasonable to assume their presence in the Corbino disk too, given its macroscopic dimensions. As it has already been pointed out,  $H = \pm 0.5$  kOe is the field at which the magnetization switches from an almost in-plane direction to the perpendicular-to-plane direction and vice-versa, and the finding that these transitions occur via the formation of domains will help to understand the temporal dynamics of the switching of the magnetization triggered by heat pulses.

## 6.5 Static magnetotransport results

Two terminal static magnetotransport measurements were performed on as-grown Mn591 using the experimental set-up described in Section 6.3. The resulting signal was read by a DMM. For these measurements the sample was patterned into the Corbino disk geometry of Fig. 3.1.

Fig. 6.10 (a) shows the dependence of the Corbino disk resistance  $R$  on  $H$  at  $T = 1.7$  K, measured while the laser was either not used or continuously emitting 60 fs pulses with  $J = 12$  mJ/cm<sup>2</sup> at a rate of 5 kHz. The contribution of the IMR was fitted linearly and subtracted from the loops.  $H$  was applied along the perpendicular-to-plane [001] direction, which means that  $R$  provides information on the component of the magnetization  $M$  along this direction thanks to the out-of-plane AMR (see Eq. 2.5). The lowest and highest values of  $R$  respectively correspond to  $M$  lying in-plane and along the perpendicular-to-plane direction, as typical of (Ga,Mn)As samples. Since the Corbino disk geometry cannot be used to

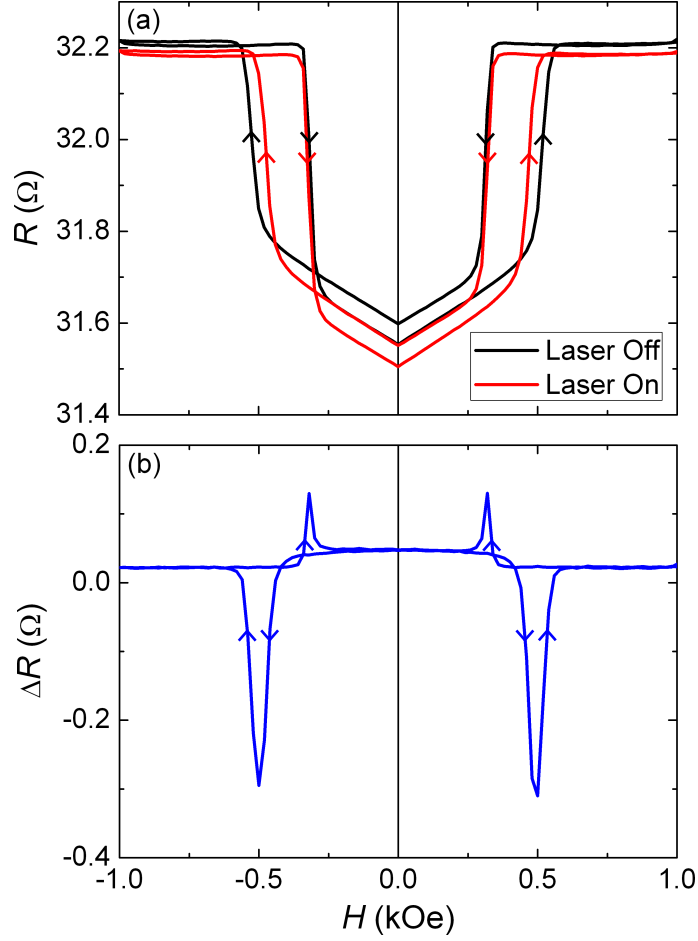


Figure 6.10: (a)  $R$  vs  $H$  loops measured at  $T = 1.7$  K for as-grown Mn591, with  $H$  applied along the perpendicular-to-plane  $[001]$  direction, while the laser is either not used (black) or continuously emitting 60 fs pulses with  $J = 12$  mJ/cm<sup>2</sup> at a rate of 5 kHz (red). (b)  $\Delta R$  vs  $H$  loop obtained as the difference between the black and the red curve in (a). The arrows indicate the sweep direction of  $H$ .

distinguish between  $M$  states symmetric for  $\hat{z} \rightarrow -\hat{z}$ , the loops in Fig. 6.10 (a) are symmetric for  $M \rightarrow -M$ . With this in mind then it can be seen that both these loops, independently on the laser being used or not, closely resemble the  $[001]$  loop measured by SQUID magnetometry that is displayed in Fig. 6.6. In fact, they both show that as-grown Mn591 is characterized by in-plane magnetic anisotropy and that the reversal of  $M$  from the positive perpendicular-to-plane direction to the negative one, and vice versa, occurs in two switching steps, corresponding to the two open sections in the loops. Comparing the two loops it is evident that the acoustic excitation does have an effect on the magnetic anisotropy of the sample, since it does narrow the two open sections in the  $R \sim M$  vs  $H$  loop. The maximum effect occurs at  $H = \pm 0.5$  kOe, as indicated by the  $\Delta R$  vs  $H$  loop in Fig. 6.10 (b), that is obtained as the difference between the loops in Fig. 6.10 (a). This is reasonable since for these values of  $H$ , the magnetocrystalline anisotropy

becomes comparable with the strain and the shape anisotropy, causing  $M$  to be in a state of unstable equilibrium, hence more sensitive to external excitations. As a matter of fact,  $M$  suddenly switches into the [001] direction as soon as  $|H|$  is increased above 0.5 kOe, as can be observed from the black loop in Fig. 6.10 (a).

Having established that using the laser in continuous-pulse mode does change the magnetic properties of as-grown Mn591 and having found at which values of  $H$  the effect is maximized, the experiment was carried on using single laser pulses. It was chosen to work at  $H = -0.5$  kOe, i.e. on the edge of the transition of  $M$  from an almost in-plane direction to the negative [001] direction. The system was prepared in this “initial” magnetic state by firstly saturating  $M$  along the positive [001] direction, and by next ramping  $H$  to reach the desired  $-0.5$  kOe value, taking care to avoid overshooting. Sitting at this value of  $H$ , the Corbino disk resistance was then measured while emitting four single laser pulses with  $J = 12$  mJ/cm<sup>2</sup>, a few seconds apart from each other, followed by continuous laser pulses with the same  $J$  at a rate of 5 kHz. The result of this measurement is shown in Fig. 6.11. It can be seen that the effect of the laser pulses is that of

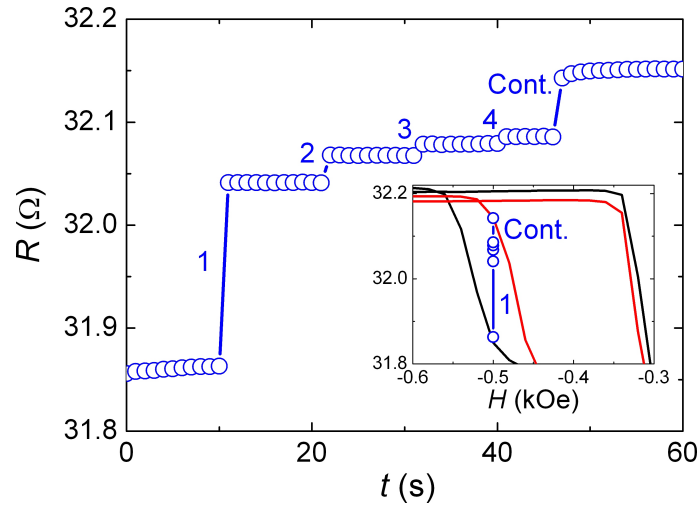


Figure 6.11:  $R$  vs  $t$  measured at  $T = 1.7$  K with  $H = -0.5$  kOe, applied along the [001] direction, while emitting four single laser pulses with  $J = 12$  mJ/cm<sup>2</sup>, a few seconds apart from each other, followed by continuous laser pulses with the same  $J$  at a rate of 5 kHz. The inset shows how the variation in  $R$  induced by this train of laser pulses relates to the  $R$  vs  $H$  loops of Fig. 6.10 (a), that have been zoomed around  $H = -0.5$  kOe.

increasing the value of  $R$  which, as explained earlier, corresponds to an increase in the component of  $M$  along the [001] direction. This can be more clearly understood looking at the inset in Fig. 6.11, that shows how the variation of  $R$  induced by this train of laser pulses relates to the  $R$  vs  $H$  loops of Fig. 6.10 (a). The first laser pulse induces the biggest variation in  $R$ ,  $\Delta R/R \sim 0.6\%$ , while

the effect of the following laser pulses rapidly decreases with their number and vanishes completely after a few thousand pulses are emitted, i.e. after the last step in  $R$  in Fig. 6.11. Each switching step in  $R \sim M$  is irreversible. The overall induced variation in  $R$  is  $\Delta R/R \sim 0.95\%$ , and corresponds to a transition of  $M$  from the state at  $H = -0.5$  kOe on the black loop (almost in-plane direction) to the state at  $H = -0.5$  kOe on the red loop (almost [001] direction). The fact that a single laser pulse is alone not enough to fully switch  $M$  into the [001] suggests that during the transition either magnetic domains are nucleated or pre-existing domain walls are moved between pinning sites, consistently with the results obtained from MOKE imaging.

## 6.6 Time-resolved magnetotransport results

Having found that a single laser pulse induces a sizeable variation in the resistance of the Corbino disk of as-grown Mn591, the experiment was next focussed on investigating the temporal evolution of this variation. For this purpose an oscilloscope, rather than a DMM, was used to read the resulting signal in the experimental set-up described in Section 6.3.

The system was initially prepared, as above, in the magnetic state at  $H = -0.5$  kOe. Sitting at this value of  $H$ , a train of six laser pulses with  $J = 12$  mJ/cm<sup>2</sup> was focused on the Al film and the temporal evolution of the Corbino disk resistance  $R$  induced by the first and the sixth of these pulses was measured. This cycle was repeated several times, in order to increase the signal-to-noise ratio of the measurement. The thus averaged  $R$  vs  $t$  traces for the first and sixth laser pulses are shown in Fig. 6.12 (a). Both  $R$  vs  $t$  traces show the arrival at the Corbino disk of three acoustic pulses: the coherent strain pulse that travels through GaAs with the longitudinal sound velocity  $v_l = 4.8$  km/s and reaches the sample in 72 ns, the longitudinal acoustic (LA) incoherent heat pulse whose peak arrives a few ns later, and the transverse acoustic (TA) incoherent heat pulse whose peak reaches the sample last, in 114 ns. The fact that  $R$  is found to decrease in both traces as a consequence of the arrival of these acoustic pulses at the Corbino disk can be explained as due to the holes in Mn591 absorbing the nonequilibrium phonons in the pulses and thus transiently heating-up. This is in fact consistent with the observed dependence of  $\rho_{xx}$  on  $T$  for  $T \lesssim 11$  K, illustrated in Fig. 6.7. On the other hand,  $R$  is expected to increase as a consequence of the switching of  $M$  towards the [001] direction, as it has been found in the previous Section. The contribution to the change in  $R$  due to the transient heating of the holes is the same for both traces in Fig. 6.12 (a), but just the first laser pulse trace contains the contribution to the change in  $R$  due to the switching of  $M$ , this being negligible by the sixth laser pulse, as previously observed. Hence

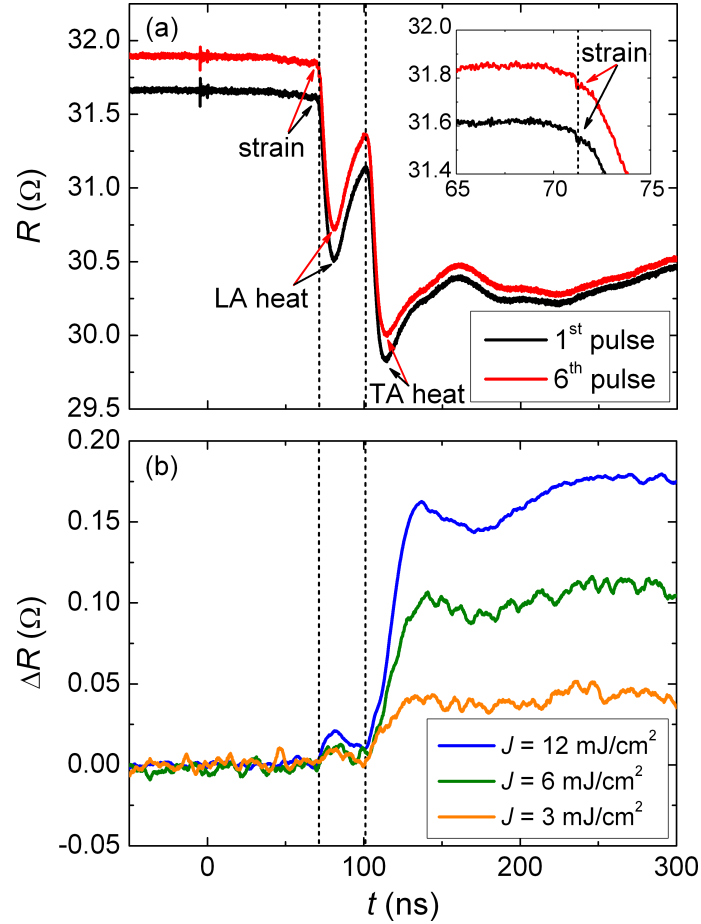


Figure 6.12: (a)  $R$  vs  $t$  measured at  $T = 1.7$  K with  $H = -0.5$  kOe, applied along the  $[001]$  direction, while emitting the first (black) and the sixth (red) pulse of a train of six laser pulses with  $J = 12$  mJ/cm<sup>2</sup>. The portion of the traces around the strain pulses is zoomed-in in the inset. (b)  $\Delta R$  vs  $t$  curve obtained as the difference between the first and sixth laser pulse traces for  $J = 12$  mJ/cm<sup>2</sup>, i.e. the traces in (a) (blue),  $J = 6$  mJ/cm<sup>2</sup> (green) and  $J = 3$  mJ/cm<sup>2</sup> (orange), where  $\Delta R$  is arbitrarily set to zero for  $t$  preceding the arrival of the acoustic pulses.  $t = 0$  corresponds to the time at which the laser pulses are emitted and the dashed vertical lines mark the arrival times of the LA and TA polarisations.

the change in  $R$  induced by the transition of  $M$  can be extracted by taking the difference between the first and sixth laser pulse traces. This was done using first and sixth laser pulse traces with three different values of  $J$  and the resulting  $\Delta R$  vs  $t$  curves are shown in Fig. 6.12 (b). It can be seen that the biggest variation in  $\Delta R$  is induced by the TA heat pulse, that this variation reaches a maximum shortly after the peak in the TA heat pulse and that its size decreases with decreasing  $J$ . For  $J = 12$  mJ/cm<sup>2</sup> the size of the variation in  $\Delta R$  is consistent with what observed in the static magnetotransport measurements shown in Fig. 6.11, suggesting that the value of  $\Delta R$  in Fig. 6.12 (b) does not decrease for  $t > 300$  ns, i.e. that the corresponding switching in  $M$  is irreversible. The much smaller,

and seemingly reversible, variation in  $\Delta R$  occurring before the switching takes place could in principle be caused by either the strain pulse or the LA heat pulse, since their arrival times at the sample are the same and both coincide with the time at which the small variation in  $\Delta R$  begins. However, the fact that such variation reaches a maximum at the time at which the LA heat pulse peaks,  $\sim 81$  ns, suggests that the strain pulse is not its triggering cause. Fig. 6.12 (b) allows then to conclusively establish that the switching of  $M$  observed in static magnetotransport measurements for as-grown Mn591 is induced by the TA heat pulse rather than strain pulses. Nevertheless, this does not exclude the possibility that the strain pulse might have effects on  $M$  of a transient nature, like those observed in [147, 148], that cannot be detected at the time resolution of this experiment.

It could be thought that the influence of the LA and TA heat pulses on the magnetic properties of (Ga,Mn)(As,P) is due to their heating of the holes. Since the holes in (Ga,Mn)(As,P) mediate, via the  $p$ - $d$  hybridization mechanism, the ferromagnetic interaction between  $\text{Mn}_{\text{Ga}}$  local moments, their temperature  $T_h$  could indeed affect the magnetic properties of the material. In particular, an increase in  $T_h$  would induce a decrease in the magnetic anisotropy energy of the material. Since, as explained in Section 6.4.3, the dependence on temperature of the resistance of the interface between (Ga,Mn)(As,P) and the metal contacts is expected to be negligible, then the value reached by  $T_h$  under the influence of the heat pulses can be determined from the comparison of the sixth pulse trace in Fig. 6.12 (a) with the  $\rho_{xx}$  vs  $T$  curve of Fig. 6.7. The values of  $T_h$ <sup>5</sup> thus obtained for a laser pulse with  $J = 12$  mJ/cm<sup>2</sup> are  $\sim 2.2$  K and  $\sim 2.7$  K for LA and TA heat pulses, respectively, in good agreement with theoretical estimations based upon balancing the rates of energy absorption from the heat pulses and of energy emission by the heated holes (that relax emitting phonons) [163]. The stronger effect that the TA heat pulse has on heating the holes in (Ga,Mn)(As,P) with respect to the LA heat pulse is commonly observed in GaAs [155] and is due several reasons, among which the strong focussing of the TA phonons along the GaAs (001) direction [164] and the rapid anharmonic decay of the THz LA phonons in GaAs [165] play a major role.

However, if the increase in  $T_h$  was the only reason for which the TA heat pulse causes  $M$  to switch, then it would be reasonable to expect the LA heat pulse to have a much bigger influence on the variation of  $M$  than the observed one, given that its effect on heating the holes is  $\sim 60\%$  of that of the TA heat pulse. A similar incongruence in the heating explanation given could be found looking at the sixth laser pulse traces shown in Fig. 6.13 for different values of  $J$ .

---

<sup>5</sup>It is important to notice that  $T_h$  is a nonequilibrium temperature, different from the lattice temperature  $T_l$ , whose change due to single laser pulses is negligible.

Since, as explained, these traces contain just the contribution to the change in  $R$

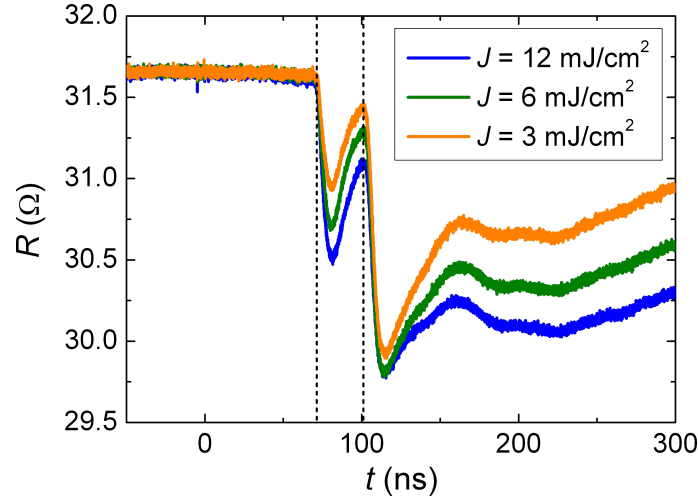


Figure 6.13:  $R$  vs  $t$  measured at  $T = 1.7$  K with  $H = -0.5$  kOe, applied along the [001] direction, while emitting the sixth laser pulse with  $J = 12$  mJ/cm<sup>2</sup> (blue),  $J = 6$  mJ/cm<sup>2</sup> (green) and  $J = 3$  mJ/cm<sup>2</sup> (orange).  $t = 0$  corresponds to the time at which the laser pulses are emitted and the dashed vertical lines mark the arrival times of the LA and TA polarisations.

due to the transient heating of the holes, it can be seen that the heating effects caused by the TA heat pulse with different values of  $J$  are comparable, while the amplitude of the induced switching of  $M$  clearly scales with  $J$ , as observed in Fig. 6.12 (b). Actually there would seem to be a correlation between the heating caused by the tail of the TA heat pulse, rather than the pulse itself, and the amplitude of the switching of  $M$ . Indeed, both the cause of the switching and the much different response of (Ga,Mn)(As,P) to the LA and TA polarizations are still open questions, in need of theoretical analysis.

The switching of  $M$  takes a time of  $\sim 35$  ns and so is a relatively slow process, compared to the leading edge of the TA heat pulse, which is again consistent with its occurring via magnetic domains dynamics.

## 6.7 Conclusions

This Chapter has shown that short incoherent phonon pulses (heat pulses) can be used to irreversibly switch the magnetization direction in the ferromagnetic semiconductor (Ga,Mn)(As,P), while no switching was found to be induced by coherent phonon pulses (strain pulses).

Both coherent and incoherent phonon pulses were generated by focusing intense fs laser pulses on a metal film deposited on the back of the sample substrate and their arrival at the (Ga,Mn)(As,P) film on the other side of the substrate was

detected electrically, by measuring the change in resistance of the film, patterned into a Corbino disk geometry. The direction of the magnetization in the film was also derived from measurements of its resistance, via the out-of-plane AMR.

Before the experiment was started, a thorough characterization of the as-grown 100 nm thick layer of  $(\text{Ga}_{0.94},\text{Mn}_{0.06})(\text{As}_{0.91},\text{P}_{0.09})$  was carried out. XRD measurements proved the presence of a small in-plane tensile strain in the film, while SQUID magnetometry measurements showed that the film is characterized by in-plane magnetic anisotropy and that the reversal of  $M$  from the positive to the negative perpendicular-to-plane direction and vice versa occurs in two switching steps, as desired. MOKE imaging measurements revealed the formation of magnetic domains during these switching steps. Finally, transport measurements showed that the resistivity of the film is relatively large, as is typical of as-grown  $(\text{Ga},\text{Mn})(\text{As},\text{P})$  samples. However the chosen Corbino disk geometry allowed to work with a low value of the resistance, which is necessary to achieve good temporal resolution in electrical detection measurements.

Static magnetotransport measurements clearly demonstrated that the acoustic excitation is effective in varying the magnetic anisotropy of the sample and, in particular, that a single laser pulse can be used to assist an irreversible switch of the magnetization between an almost in-plane direction to the perpendicular-to-plane direction. Time-resolved magnetotransport measurements were then performed and it was found that the switching process is not triggered by the strain pulse, but rather by the TA heat pulse, that reaches the sample  $\sim 30$  ns after the strain pulse. It was moreover shown that this switching takes a time of  $\sim 35$  ns and so is a relatively slow process, compared to the leading edge of the TA heat pulse, which is consistent with its occurring via magnetic domains dynamics. The switching of the magnetization could be ascribed to the heat pulses transiently heating-up the holes in the material, given that the holes mediate the ferromagnetic interaction in  $(\text{Ga},\text{Mn})(\text{As},\text{P})$  and hence dictate its magnetic anisotropy. However this explanation is not entirely convincing and the cause of the switching of the magnetization as well as the lack of a switching effect from the strain pulse are still open questions. It is though necessary to remark that these results do not exclude the possibility that the strain pulse might have effects on the magnetization of a transient nature that cannot be detected at the time resolution of this experiment.

# Chapter 7

## Summary and future work

Within the research field of semiconductor spintronics, the ferromagnetic semiconductor (Ga,Mn)As has played a major role. The large spin-orbit interaction characteristic of the holes in the valence band of (Ga,Mn)As is responsible for some of its most interesting properties, such as the magnetocrystalline anisotropy, the magnetoelastic coupling and the extraordinary contributions to the magnetotransport. Furthermore, the interplay between ferromagnetism and semiconductivity, arising from the hole-mediated nature of the ferromagnetic interaction in (Ga,Mn)As, allows for the remarkable possibility of manipulating its magnetic properties by varying the state of the holes using non-magnetic parameters like electric fields, electric currents, light or strain. This circumstance could be technologically useful to avoid the inefficient use of magnetic fields to write data in magnetic memories. It must be remarked though that the highest Curie temperature so far obtained for (Ga,Mn)As is still well below room temperature and it does seem unlikely that (Ga,Mn)As will become a relevant material for future technological applications. Nonetheless the study of (Ga,Mn)As remains a fervent research area since it allows to explore a variety of novel functionalities and spintronics concepts that could in future be implemented in other systems. For this reason (Ga,Mn)As is often referred to as a test bench material for semiconductor spintronics.

This Thesis contains the results of three experimental investigations that demonstrate how different nonmagnetic approaches can be used to efficiently manipulate the magnetic anisotropy in (Ga,Mn)As thin films. These include generating strain via growing the magnetic film on lattice-mismatched substrates (Chapter 4) or bonding it to a piezoelectric actuator (Chapter 5), and using short phonon pulses (Chapter 6). The details of the results achieved in each experimental Chapter are detailed in the following, together with plans for future work.

In Chapter 4 the properties of the ferromagnetic semiconductor (Ga,Mn)(As,P), obtained by co-doping (Ga,Mn)As with phosphorus, were investigated through

structural, magnetometry, transport and magnetotransport measurements. A series of 25 nm thick  $(\text{Ga}_{0.94}, \text{Mn}_{0.06})(\text{As}_{1-y}, \text{P}_y)$  layers with  $y = 3\% - 10\%$  were grown on GaAs substrates via LT-MBE for this study. By varying  $y$  it was possible to vary the sign of the in-built growth strain, to which the magnetic anisotropy in (Ga,Mn)As is extremely sensitive. The fact that all the as-grown samples were characterized by an in-plane magnetic easy axis, even when under in-plane tensile strain, was ascribed to their high degree of carrier compensation. The as-grown sample with  $y = 10\%$  was even found to have a dependence of resistivity with temperature typical of insulating (Ga,Mn)As. On the other hand, annealed tensile-strained (Ga,Mn)(As,P) layers, i.e. with  $y \geq 9\%$ , were characterized by a perpendicular-to-plane magnetic easy axis, consistent with their much lower resistivities.  $T_C$  was found to decrease upon increasing  $y$  for both as-grown and annealed samples. Finally, it was demonstrated that a gradual reorientation of the magnetic easy axis from an in-plane direction to the perpendicular-to-plane direction can occur in tensile-strained samples not only upon post-growth annealing, but also upon increasing the temperature. Considering all these aspects (Ga,Mn)(As,P) results to be not only a useful material for studies where perpendicular magnetic anisotropy is a necessary requirement, but also an extremely interesting type of ferromagnetic semiconductor in itself, in which several schemes to tune in-plane and perpendicular magnetic anisotropies are possible. For this reason it could be useful in future to fully characterize also the magnetotransport properties of this material, that have just been briefly addressed at the end of the Chapter.

In Chapter 5 the effects of piezoelectric-induced strain on the magnetic anisotropy of a highly-doped annealed (Ga,Mn)As sample were explored. Two devices were prepared for magnetotransport and SQUID magnetometry measurements, respectively consisting of two (Ga,Mn)As samples, one patterned into a Hall bar and one left unpatterned, each bonded to a piezoelectric actuator, after thinning their substrates. The measurements were all performed at a much higher temperature (150 K) than previous investigations, where larger strains can be generated by the actuators. It was shown that large and reversible rotations of the magnetic easy axis can be achieved in these samples by varying the voltage applied to the piezoelectric actuator, thus demonstrating that strain-mediated electric control of ferromagnetism is effective even in the limit of high doping levels and high Curie temperatures, where direct electric control of ferromagnetism via carrier manipulation is not possible. Furthermore, the results obtained from magnetotransport and SQUID magnetometry measurements were compared, extracting the dependence of the piezo-induced uniaxial magnetic anisotropy constant upon strain in both cases and discussing why the magnetotransport measurements

were believed to be more accurate than SQUID magnetometry measurements in evaluating the inverse magnetostriction effects in (Ga,Mn)As-piezoelectric actuator hybrid systems.

For future investigations, measurements of the piezoelectric-induced rotation of the magnetic easy axis could be improved in several ways. Firstly it would be interesting to find out whether the epoxy layer induces a strain on the (Ga,Mn)As film in the absence of the piezoelectric actuator. Secondly it would be useful to measure the initial strain state in (Ga,Mn)As that could arise from the anisotropic nature of the thermal contraction of the piezoelectric actuator. For this purpose a full-bridge strain gauge (i.e. four strain gauges connected in a Wheatstone bridge configuration) should be used, since its intrinsic compensation for thermal-generated strain would allow one to measure just the strain induced on (Ga,Mn)As by the anisotropic contraction of the actuator while cooling the device from room temperature down to the desired temperature. Furthermore, it could be useful to use 100  $\mu\text{m}$  or 150  $\mu\text{m}$  thick GaAs substrates in order to avoid the process of thinning the substrate by wet etching which could induce inhomogeneities in the substrate thickness and consequently in the transmission of strain to the (Ga,Mn)As layer, especially in large SQUID samples. Even with this improvement, however, the transmission of strain from the actuator to the (Ga,Mn)As layer could still occur unevenly due to inhomogeneities in the thickness of the epoxy layer, which is spread manually on top of the actuator. Indeed, this layer of epoxy certainly represents a limiting factor in the interpretation of the results and, more in general, in the reliability of the method. A possible solution to overcome this problem and achieve efficient and reliable transmission of strain from the actuator to the sample could be the direct deposition of a PZT ceramic film on (Ga,Mn)As. The synthesis of high quality PZT thin films is well established but typically requires temperatures in excess of 400  $^{\circ}\text{C}$ . Given the fact that exposing (Ga,Mn)As to temperatures above  $\sim 250$   $^{\circ}\text{C}$  would be detrimental to its ferromagnetic properties, the PZT film should be synthesized at low temperatures, using more unusual deposition techniques like the hydrothermal method [166, 167]. Finally, it would be interesting to use piezoelectric actuators to induce rotations of the magnetic easy axis from in-plane to out-of-plane directions. This could be achieved using actuators generating a biaxial strain and (Ga,Mn)(As,P) samples with Mn and P concentrations and post-growth annealing time carefully adjusted to obtain a small in-built growth strain.

Finally, Chapter 6 has presented the results of an investigation attempting to use ultrashort strain pulses to switch the magnetization direction in a (Ga,Mn)(As,P) sample on fast time scales. These pulses were generated by emitting intense fs laser pulses on a metal film deposited on the back of the sample

substrate and their arrival at the (Ga,Mn)(As,P) film on the other side of the substrate, as well as their effect on the magnetic properties of the film, was detected electrically. It was indeed demonstrated that a single laser pulse can be used to assist an irreversible switch of the magnetization between an almost in-plane direction to the perpendicular-to-plane direction. However, time-resolved magnetotransport measurements showed that the switching is not triggered by the strain pulse, but rather by the transverse heat pulse, the latter being generated at the same time as the strain pulse during the optical excitation of the metal film. It was shown that the switching is a relatively slow process, since it occurs via magnetic domains dynamics; while possible mechanisms were speculated, some aspects of the results still remain unclear, including the lack of a switching effect induced by the strain pulse.

The greatest improvement to this experiment could be obtained by performing optical pump-probe measurements rather than electrical one to increase the temporal resolution. This could allow to detect the presence of possible transient effects of the strain pulse on the magnetic properties of the sample. Furthermore, the effects of the strain pulse might be increased using a thin (Ga,Mn)(As,P) layer ( $\sim 25$  nm) with a thicker GaAs layer ( $\sim 200$  nm) grown on top of it. In this way the strain pulse would be maximized in the (Ga,Mn)(As,P) layer without suffering the reduction of amplitude caused by the destructive interference between the strain pulse travelling towards the open surface and back away from it. The only drawback of this approach would be the impossibility of annealing the (Ga,Mn)(As,P) layer.

# Appendix A

## Angles definition

The angles consistently used throughout this thesis are defined in Fig. A.1.

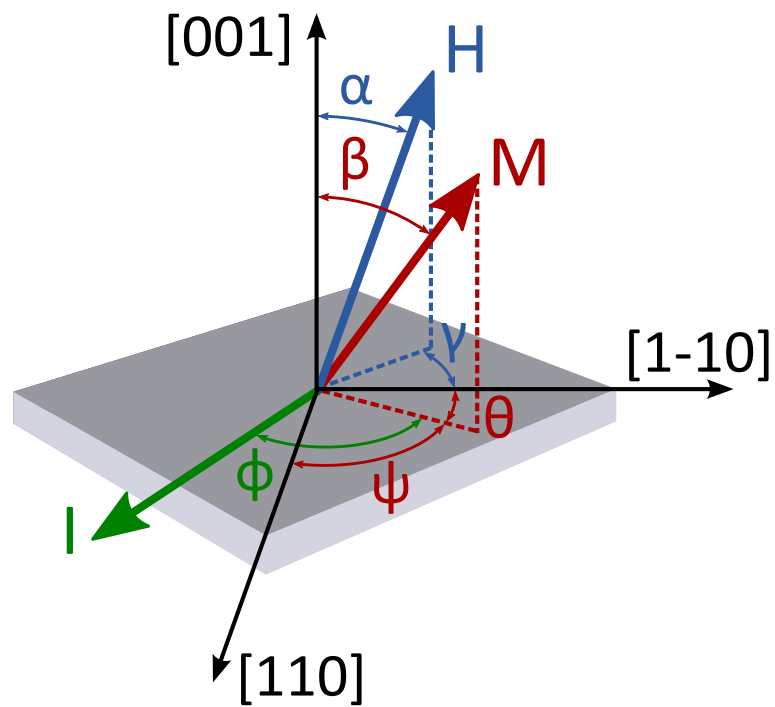


Figure A.1: Definition of the angles consistently used throughout this thesis.

# Appendix B

## List of acronyms

**AHE** Anomalous Hall Effect

**AMR** Anisotropic MagnetoResistance

**BEP** Beam Equivalent Pressure

**DC** Direct Current

**DMM** Digital MultiMeter

**DMS** Dilute Magnetic Semiconductors

**GMR** Giant MagnetoResistance

**IMR** Isotropic MagnetoResistance

**LA** Longitudinal Acoustic

**LT-MBE** Low-Temperature Molecular Beam Epitaxy

**MBE** Molecular Beam Epitaxy

**MOKE** Magneto-Optical Kerr Effect

**MRAM** Magnetoresistive Random Access Memory

**NPBS** Non-Polarizing Beam Splitter

**OHE** Ordinary Hall Effect

**PZT** lead (Pb) zirconate (Zr) titanate (Ti)

**RAM** Random Access Memory

**RF** Radio Frequency

**RHEED** Reflection High-Energy Electron Diffraction

**SAW** Surface Acoustic Wave

**SQUID** Superconducting QUantum Interference Device

**TA** Transverse Acoustic

**TMR** Tunneling MagnetoResistance

**XMCD** X-ray Magnetic Circular Dichroism

**XRD** X-Ray Diffraction

# Appendix C

## Conversion of magnetic units

The units of the magnetic quantities used in this thesis are listed in Tab. C.1 for both the cgs (centimetre-gram-second) and SI (Système International) unit systems, alongside the conversion factors between them.

Quantity	Symbol	cgs units	Conversion factor	SI units
Magnetic induction	$\mathbf{B}$	G	$10^{-4}$	T
Magnetic field strength	$\mathbf{H}$	Oe	$10^3/4\pi$	A/m
Volume magnetization	$\mathbf{M}$	emu/cm <sup>3</sup>	$10^3$	A/m
Magnetic moment	$\mathbf{m}$	emu, erg/G	$10^{-3}$	A·m <sup>2</sup> , J/T
Volume susceptibility	$\chi$	emu/cm <sup>3</sup>	$4\pi$	dimensionless
Energy density	$E$	erg/cm <sup>3</sup>	$10^{-1}$	J/m <sup>3</sup>
Magnetic anisotropy constant	$K$	erg/cm <sup>3</sup>	$10^{-1}$	J/m <sup>3</sup>

Table C.1: List of the units of the magnetic quantities used in this thesis for both the the cgs and SI unit systems. The SI units are obtained multiplying the cgs units by the corresponding conversion factor.

The definition of the quantities  $\mathbf{B}$ ,  $\mathbf{H}$  and  $\mathbf{M}$  differs in the two unit systems, being:

$$\mathbf{B} = \mathbf{H} + 4\pi\mathbf{M}, \quad (\text{C.1})$$

in the cgs system and:

$$\mathbf{B} = \mu_0(\mathbf{H} + \mathbf{M}), \quad (\text{C.2})$$

in the SI system, where  $\mu_0$  is the vacuum permeability.

# Bibliography

- [1] G. E. MOORE, *Electronics* **38**, 8 (1965).
- [2] P. S. PEERCY, *Nature* **406**, 1023 (2000).
- [3] [HTTP://WWW.ITRS.NET/](http://www.itrs.net/).
- [4] G. BOURIANOFF, M. BRILLOUËT, R. K. CAVIN, T. HIRAMOTO, J. A. HUTCHBY, A. M. IONESCU, and K. UCHIDA, *Proceeding of the IEEE* **98**, 1986 (2010).
- [5] G. A. PRINZ, *Science* **282**, 1660 (1998).
- [6] S. A. WOLF, D. D. AWSCHALOM, R. A. BUHRAM, J. M. DAUGHTON, S. VON MOLNÁR, M. L. ROUKES, A. Y. CHTCHELKANOVA, and D. M. TREGER, *Science* **294**, 1488 (2001).
- [7] W. THOMSON, *Proceedings of the Royal Society of London* **8**, 546 (1857).
- [8] M. JULLIÈRE, *Phys. Lett. A* **54**, 225 (1975).
- [9] M. N. BAIBICH, J. M. BROTO, A. FERT, F. NGUYEN VAN DAU, F. PETROFF, P. ETIENNE, G. CREUZET, A. FRIEDERICH, and J. CHAZELAS, *Phys. Rev. Lett.* **61**, 2472 (1988).
- [10] G. BINASCH, P. GRÜNBERG, F. SAURENBACH, and W. ZINN, *Phys. Rev. B* **39**, 4828 (1989).
- [11] B. N. ENGEL, J. ÅKERMAN, B. BUTCHER, R. W. DAVE, M. DE-HERRERA, M. DURLAM, G. GRYNKEWICH, J. JANESKY, S. V. PIETAMBARAM, N. D. RIZZO, J. M. SLAUGHTER, K. SMITH, J. J. SUN, and S. TEHRANI, *IEEE Trans. Magn.* **42**, 132 (2005).
- [12] R. P. COWBURN and M. E. WELLAND, *Science* **287**, 1466 (2000).
- [13] D. A. ALLWOOD, G. XIONG, C. C. FAULKNER, D. ATKINSON, D. PETIT, and R. P. COWBURN, *Science* **309**, 1688 (2005).

- [14] W. ZHAO, E. BELHAIRE, Q. MISTRAL, E. NICOLLE, T. DEVOLDER, and C. CHAPPERT, *Proc. ICSICT*, 799 (2006).
- [15] T. DIETL, *Lectures Notes* **712**, 1 (2007).
- [16] H. OHNO, *Science* **281**, 951 (1998).
- [17] H. OHNO, F. MATSUKURA, and Y. OHNO, *JSAP International* **5**, 4 (2002).
- [18] I. ŽUTIĆ, J. FABIAN, and S. DAS SARMA, *Reviews of Modern Physics* **76**, 323 (2004).
- [19] L. KOWALCZYK, A. MYCIELSKI, L. ŚNIADOWER, and R. R. GAŁĄZKA, *Phys. stat. sol. (c)* **1**, 985 (2004).
- [20] S. DATTA and B. DAS, *Appl. Phys. Lett.* **56**, 665 (1990).
- [21] D. D. AWSCHALOM and M. E. FLATTÉ, *Nature Physics* **3**, 153 (2007).
- [22] Z. H. XIONG, D. WU, Z. V. VARDENY, and J. SHI, *Nature* **427**, 821 (2004).
- [23] C. L. KANE and J. E. MOORE, *Physics World* **24**, 32 (2011).
- [24] A. H. CASTRO NETO, *Science* **332**, 315 (2011).
- [25] A. MAUGER and C. GODART, *Phys. Rep.* **141**, 51 (1986).
- [26] J. F. GREGG, *Nature Materials* **6**, 798 (2007).
- [27] J. K. FURDYNA and J. KOSSUT, *Semiconductors and semimetals* **25** (1998).
- [28] A. HAURY, A. WASIELA, A. ARNOULT, J. CIBERT, S. TATARENKO, T. DIETL, and Y. MERLE D'AUBIGNÉ, *Phys. Rev. Lett.* **79**, 511 (1997).
- [29] D. FERRAND, J. CIBERT, C. BOURGOGNON, S. TATARENKO, A. WASIELA, G. FISHMAN, A. BONANNI, H. SITTE, S. KOLEŚNIK, J. JAROSZYŃSKI, A. BARCZ, and T. DIETL, *J. Cryst. Growth* **214-215**, 387 (2000).
- [30] H. MUNEKATA, H. OHNO, S. VON MOLNÁR, A. SEGMÜLLER, and L. L. CHANG, *Phys. Rev. Lett.* **63**, 1849 (1989).
- [31] H. OHNO, A. SHEN, F. MATSUKURA, A. OIWA, A. ENDO, S. KATSUMOTO, and Y. IYE, *Appl. Phys. Lett.* **69**, 363 (1996).
- [32] F. MATSUKURA, H. OHNO, A. SHEN, and Y. SUGAWARA, *Phys. Rev. B* **57**, R2037 (1998).

- [33] H. OHNO, D. CHIBA, F. MATSUKURA, T. OMIYA, E. ABE, T. DIETL, Y. OHNO, and K. OHTANI, *Nature* **408**, 944 (2000).
- [34] D. CHIBA, M. YAMANOUCHI, F. MATSUKURA, and H. OHNO, *Science* **301**, 943 (2003).
- [35] D. CHIBA, Y. SATO, T. KITA, F. MATSUKURA, and H. OHNO, *Phys. Rev. Lett.* **93**, 216602 (2004).
- [36] M. YAMANOUCHI, D. CHIBA, F. MATSUKURA, and H. OHNO, *Nature* **428**, 539 (2004).
- [37] S. KOSHIHARA, A. OIWA, M. HIRASAWA, S. KATSUMOTO, Y. IYE, C. URANO, H. TAKAGI, and H. MUNEKATA, *Phys. Rev. Lett.* **78**, 4617 (1997).
- [38] H. BOUKARI, P. KOSSACKI, M. BERTOLINI, D. FERRAND, J. CIBERT, S. TATARENKO, A. WASIELA, J. A. GAJ, and T. DIETL, *Phys. Rev. Lett.* **88**, 207204 (2002).
- [39] A. SHEN, H. OHNO, F. MATSUKURA, Y. SUGAWARA, N. AKIBA, T. KUROIWA, A. OIWA, A. ENDO, S. KATSUMOTA, and Y. IYE, *J. Cryst. Growth* **175-176**, 1069 (1997).
- [40] J. WENISCH, C. GOULD, L. EBEL, J. STORZ, K. PAPPERT, M. J. SCHMIDT, C. KUMPF, G. SCHMIDT, K. BRUNNER, and L. W. MOLENKAMP, *Phys. Rev. Lett.* **99**, 077201 (2007).
- [41] A. W. RUSHFORTH, E. DE RANIERI, J. ZEMEN, J. WUNDERLICH, K. W. EDMONDS, C. S. KING, E. AHMAD, R. P. CAMPION, C. T. FOXON, B. L. GALLAGHER, K. VÝBORNÝ, J. KUČERA, and T. JUNGWIRTH, *Phys. Rev. B* **78**, 085314 (2008).
- [42] C. CHAPPERT, A. FERT, and F. NGUYEN VAN DAU, *Nature Materials* **6**, 813 (2007).
- [43] M. WANG, R. P. CAMPION, A. W. RUSHFORTH, K. W. EDMONDS, C. T. FOXON, and B. L. GALLAGHER, *Appl. Phys. Lett.* **93**, 132103 (2008).
- [44] T. DIETL, *Nature Materials* **9**, 965 (2010).
- [45] H. OHNO, *Nature Materials* **9**, 952 (2010).
- [46] D. DESIMONE, C. E. C. WOOD, and C. A. EVANS, *J. Appl. Phys.* **53**, 4938 (1982).

- [47] R. P. CAMPION, K. W. EDMONDS, L. X. ZHAO, K. Y. WANG, C. T. FOXON, B. L. GALLAGHER, and C. STADDON, *J. Cryst. Growth* **247**, 42 (2003).
- [48] R. P. CAMPION, V. A. GRANT, K. W. EDMONDS, B. L. GALLAGHER, and C. T. FOXON, *Phys. Stat. Sol. (b)* **244**, 2944 (2007).
- [49] T. JUNGWIRTH, J. SINOVA, J. MAŠEK, J. KUČERA, and A. H. MACDONALD, *Rev. Mod. Phys.* **78**, 809 (2006).
- [50] K. M. YU, W. WALUKIEWICZ, T. WOJTOWICZ, I. KURYLISZYN, X. LIU, Y. SASAKI, and J. K. FURDYNA, *Phys. Rev. B* **65**, 201303 (2002).
- [51] D. T. J. HURLE, *J. Appl. Phys.* **85**, 6957 (1999).
- [52] J. BLINOWSKI and P. KACMAN, *Phys. Rev. B* **67**, 121204 (2003).
- [53] K. W. EDMONDS, N. R. S. FARLEY, T. K. JOHAL, G. VAN DER LAAN, R. P. CAMPION, B. L. GALLAGHER, and C. T. FOXON, *Phys. Rev. B* **71**, 064418 (2005).
- [54] K. W. EDMONDS, K. Y. WANG, R. P. CAMPION, A. C. NEUMANN, N. R. S. FARLEY, B. L. GALLAGHER, and C. T. FOXON, *Appl. Phys. Lett.* **81**, 4991 (2002).
- [55] K. W. EDMONDS, P. BOGUSŁAWSKI, K. Y. WANG, R. P. CAMPION, S. N. NOVIKOV, N. R. S. FARLEY, B. L. GALLAGHER, C. T. FOXON, M. SAWICKI, T. DIETL, M. BUONGIORNO NARDELLI, and J. BERNHOLC, *Phys. Rev. Lett.* **92**, 037201 (2004).
- [56] D. E. BLISS, W. WALUKIEWICZ, J. W. A. III, E. E. HALLER, K. T. CHAN, and S. TANIGAWA, *J. Appl. Phys.* **71**, 1699 (1992).
- [57] A. SHEN, F. MATSUKURA, S. P. GUO, Y. SUGAWARA, H. OHNO, M. TANI, H. ABE, and H. C. LIU, *J. Cryst. Growth* **201/202**, 679 (1999).
- [58] L. X. ZHAO, C. R. STADDON, K. Y. WANG, K. W. EDMONDS, R. P. CAMPION, B. L. GALLAGHER, and C. T. FOXON, *Appl. Phys. Lett.* **86**, 0711902 (2005).
- [59] G. M. SCHOTT, W. FASCHINGER, and L. W. MOLENKAMP, *Appl. Phys. Lett.* **79**, 1807 (2001).
- [60] J. SZCZYTKO, A. TWARDOWSKI, K. ŚWIĄTEK, M. PALCZEWSKA, M. TANAKA, T. HAYASHI, and K. ANDO, *Phys. Rev. B* **60**, 8304 (1999).
- [61] P. W. ANDERSON, *Phys. Rev. B* **79**, 350 (1950).

- [62] C. ZENER, *Phys. Rev.* **81**, 440 (1951).
- [63] T. DIETL, H. OHNO, F. MATSUKURA, J. CIBERT, and D. FERRAND, *Science* **287**, 1019 (2000).
- [64] K. Y. WANG, R. P. CAMPION, K. W. EDMONDS, M. SAWICKI, T. DIETL, C. T. FOXON, and B. L. GALLAGHER, *ICPS-27 Proceedings* **772**, 333 (2005).
- [65] J. SCHLIEMANN and A. H. MACDONALD, *Phys. Rev. Lett.* **88**, 137201 (2002).
- [66] G. ZARAND and B. JANKO, *Phys. Rev. Lett.* **89**, 047201 (2002).
- [67] T. JUNGWIRTH, J. MAŠEK, K. Y. WANG, K. W. EDMONDS, M. SAWICKI, M. POLINI, J. SINOVA, A. H. MACDONALD, R. P. CAMPION, L. X. ZHAO, N. R. S. FARLEY, T. K. JOHAL, G. VAN DER LAAN, C. T. FOXON, and B. L. GALLAGHER, *Phys. Rev. B* **73**, 165205 (2005).
- [68] B. D. CULLITY and C. D. GRAHAM, *Introduction to magnetic materials*, 1972.
- [69] S. BLUNDELL, *Magnetism in condensed matter*, 2001.
- [70] M. ABOLFATH, T. JUNGWIRTH, J. BRUM, and A. H. MACDONALD, *Phys. Rev. B* **63**, 054418 (2001).
- [71] T. DIETL, H. OHNO, and F. MATSUKURA, *Phys. Rev. B* **63**, 195205 (2001).
- [72] X. LIU, Y. SASAKI, and J. K. FURDYNA, *Phys. Rev. B* **67**, 205204 (2003).
- [73] M. SAWICKI, F. MATSUKURA, A. IDZIASZEK, T. DIETL, G. M. SCHOTT, C. RUESTER, C. GOULD, G. KARCZEWSKI, G. SCHMIDT, and L. W. MOLENKAMP, *Phys. Rev. B* **70**, 245325 (2004).
- [74] U. WELP, V. K. VLASKO-VLASOV, A. MENZEL, H. D. YOU, X. LIU, J. K. FURDYNA, and T. WOJTOWICZ, *Appl. Phys. Lett.* **85**, 260 (2004).
- [75] S. PIANO, X. MARTI, A. W. RUSHFORTH, K. W. EDMONDS, R. P. CAMPION, M. WANG, O. CAHA, T. U. SCHÜLLI, V. HOLÍ, and B. L. GALLAGHER, *Appl. Phys. Lett.* **98**, 152503 (2011).
- [76] M. KOPECKÝ, J. KUB, F. MÁCA, J. MAŠEK, O. PACHEROVÁ, A. W. RUSHFORTH, B. L. GALLAGHER, R. P. CAMPION, V. NOVÁK, and T. JUNGWIRTH, *Phys. Rev. B* **83**, 235324 (2011).

- [77] J. ZEMEN, J. KUČERA, K. OLEJNÍK, and T. JUNGWIRTH, *Phys. Rev. B* **80**, 155203 (2009).
- [78] K. Y. WANG, M. SAWICKI, K. W. EDMONDS, R. P. CAMPION, S. MAAT, C. T. FOXON, B. L. GALLAGHER, and T. DIETL, *Phys. Rev. Lett.* **95**, 217204 (2005).
- [79] H. B. CALLEN and E. CALLEN, *J. Phys. Chem. Solids* **27**, 1271 (1966).
- [80] M. SAWICKI, K. Y. WANG, K. W. EDMONDS, R. P. CAMPION, C. R. STADDON, N. R. S. FARLEY, C. T. FOXON, E. PAPIS, E. KAMIŃSKA, A. PIOTROWSKA, T. DIETL, and B. L. GALLAGHER, *Phys. Rev. B* **71**, 121302 (2005).
- [81] E. C. STONER and E. P. WOHLFARTH, *Phil. Trans. Roy. Soc. A* **240**, 599 (1948).
- [82] T. SHONO, T. HASEGAWA, T. FUKUMURA, F. MATSUKURA, and H. OHNO, *Appl. Phys. Lett.* **77**, 1363 (2000).
- [83] U. WELP, V. K. VLASKO-VLASOV, X. LIU, J. K. FURDYNA, and T. WOJTOWICZ, *Phys. Rev. Lett.* **90**, 167206 (2003).
- [84] A. VAN ESCH, L. VAN BOCKSTAL, J. DE BOECK, G. VERBANCK, A. S. VAN STEENBERGEN, P. J. WELLMANN, B. GRIETEN, R. BOGAERTS, F. HERLACH, and G. BORGHIS, *Phys. Rev. B* **56**, 13103 (1997).
- [85] P. M. KRSTAJIC, F. M. PEETERS, V. A. IVANOV, V. FLEUROV, and K. KIKOIN, *Phys. Rev. B* **70**, 195215 (2004).
- [86] V. NOVÁK, K. OLEJNÍK, J. WUNDERLICH, M. CUKR, K. VÝBORNÝ, A. W. RUSHFORTH, K. W. EDMONDS, R. P. CAMPION, B. L. GALLAGHER, J. SINOVA, and T. JUNGWIRTH, *Phys. Rev. Lett.* **101**, 077201 (2008).
- [87] T. JUNGWIRTH, B. L. GALLAGHER, and J. WUNDERLICH, *Semiconduct. Semimet.* **82**, 135 (2008).
- [88] T. R. MCGUIRE and R. I. POTTER, *IEEE Trans. Magn.* **11**, 1018 (1975).
- [89] E. H. HALL, *Amer. Jour. Math.* **2**, 287 (1879).
- [90] F. MATSUKURA, M. SAWICKI, T. DIETL, D. CHIBA, and H. OHNO, *Physica E* **21**, 1032 (2004).
- [91] K. Y. WANG, K. W. EDMONDS, R. P. CAMPION, L. X. ZHAO, C. T. FOXON, and B. L. GALLAGHER, *Phys. Rev. B* **72**, 085201 (2005).

- [92] W. DÖRING, *W. Ann. Phys.* **424**, 259 (1938).
- [93] A. W. RUSHFORTH, K. VÝBORNÝ, C. S. KING, K. W. EDMONDS, R. P. CAMPION, C. T. FOXON, J. WUNDERLICH, A. C. IRVINE, P. VAŠEK, V. NOVÁK, K. OLEJNÍK, J. SINOVA, T. JUNGWIRTH, and B. L. GALLAGHER, *Phys. Rev. Lett.* **99**, 147207 (2007).
- [94] T. OMIYA, F. MATSUKURA, T. DIETL, Y. OHNO, T. SAKON, M. MOTOKAWA, and H. OHNO, *Physica E* **7**, 976 (2000).
- [95] L. BERGER and G. BERGMANN, *The Hall effect and its applications*, 1979.
- [96] T. JUNGWIRTH, Q. NIU, and A. H. MACDONALD, *Phys. Rev. Lett.* **88**, 207208 (2002).
- [97] K. W. EDMONDS, R. P. CAMPION, K. Y. WANG, A. C. NEUMANN, B. L. GALLAGHER, C. T. FOXON, and P. C. MAIN, *J. Appl. Phys.* **93**, 6787 (2003).
- [98] T. JUNGWIRTH, K. Y. WANG, J. MAŠEK, K. W. EDMONDS, J. KÖNIG, J. SINOVA, M. POLINI, N. A. GONCHARUK, A. H. MACDONALD, M. SAWICKI, A. W. RUSHFORTH, R. P. CAMPION, L. X. ZHAO, C. T. FOXON, and B. L. GALLAGHER, *Phys. Rev B* **72**, 165204 (2005).
- [99] M. SAWICKI, W. STEFANOWICZ, and A. NEY, *Semicond. Sci. Technol.* **26**, 064006 (2011).
- [100] A. HUBERT and R. SCHÄFER, *Magnetic domains: the analysis of magnetic microstructures*, 1998.
- [101] M. A. SCARPULLA, B. L. CARDOZO, R. FARSHCHI, W. M. HLAING OO, M. D. MCCLUSKEY, K. M. YU, and O. D. DUBON, *Phys. Rev. Lett.* **95**, 207204 (2005).
- [102] J. L. XU and M. VAN SCHILFGAARDE, *J. Magn. Magn. Mater.* **305**, 63 (2006).
- [103] J. MAŠEK, J. KUDRNOVSKÝ, F. MÁČA, J. SINOVA, A. H. MACDONALD, R. P. CAMPION, B. L. GALLAGHER, and T. JUNGWIRTH, *Phys. Rev. B* **75**, 045202 (2007).
- [104] P. R. STONE, J. W. BEEMAN, K. M. YU, and O. D. DUBON, *Physica B* **401-402**, 454 (2007).
- [105] P. R. STONE, K. ALBERI, S. K. Z. TARDIF, J. W. BEEMAN, K. M. YU, W. WALUKIEWICZ, and O. D. DUBON, *Phys. Rev. Lett.* **101**, 087203 (2008).

- [106] R. BOUZERAR, F. MÁCA, J. KUDRONVSKÝ, and L. BERGQVIST, *Phys. Rev. B* **82**, 035207 (2010).
- [107] A. W. RUSHFORTH, M. WANG, N. R. S. FARLEY, R. P. CAMPION, K. W. EDMONDS, C. R. STADDON, C. T. FOXON, and B. L. GALLAGHER, *J. Appl. Phys.* **104**, 073908 (2008).
- [108] A. LEMAÎTRE, A. MIARD, L. TRAVERS, O. MAUGUIN, L. LARGEAU, C. GOURDON, V. JEUDY, M. TRAN, and J.-M. GEORGE, *Appl. Phys. Lett.* **93**, 021123 (2008).
- [109] S. N. PIRAMANAYAGAM, *J. Appl. Phys.* **102**, 011301 (2007).
- [110] D. RAVELOSONA, D. LACOUR, J. A. KATINE, B. D. TERRIS, and C. CHAPPERT, *Phys. Rev. Lett.* **95**, 117203 (2005).
- [111] S.-W. JUNG, W. KIM, T.-D. LEE, K.-J. LEE, and H.-W. LEE, *Appl. Phys. Lett.* **92**, 202508 (2008).
- [112] L. THEVENARD, L. LARGEAU, O. MAUGUIN, G. PATRIARCHE, and A. LEMAÎTRE, *Phys. Rev. B* **73**, 195331 (2006).
- [113] K. Y. WANG, A. W. RUSHFORTH, V. A. GRANT, R. P. CAMPION, K. W. EDMONDS, C. R. STADDON, C. T. FOXON, B. L. GALLAGHER, J. WUNDERLICH, and D. A. WILLIAMS, *J. Appl. Phys.* **101**, 106101 (2007).
- [114] S. HAGHGOO, M. CUBUKCU, H. J. VON BARDELEBEN, L. THEVENARD, A. LEMAÎTRE, and C. GOURDON, *Phys. Rev. B* **82**, 041301 (2010).
- [115] K. Y. WANG, K. W. EDMONDS, A. C. IRVINE, G. TATARA, E. DE RANIERI, J. WUNDERLICH, K. OLEJNÍK, A. W. RUSHFORTH, R. P. CAMPION, D. A. WILLIAMS, C. T. FOXON, and B. L. GALLAGHER, *Appl. Phys. Lett.* **97**, 262102 (2010).
- [116] M. CUBUKCU, H. J. VON BARDELEBEN, K. KHAZEN, J. L. CANTIN, O. MAUGUIN, L. LARGEAU, and A. LEMAÎTRE, *Phys. Rev. B* **81**, 041202 (2010).
- [117] M. CUBUKCU, H. J. VON BARDELEBEN, J. L. CANTIN, and A. LEMAÎTRE, *Appl. Phys. Lett.* **96**, 102502 (2010).
- [118] P. WADLEY, A. CASIRAGHI, M. WANG, K. W. EDMONDS, R. P. CAMPION, A. W. RUSHFORTH, B. L. GALLAGHER, C. R. STADDON, K. Y. WANG, G. VAN DER LAAN, and E. ARENHOLZ, *Appl. Phys. Lett.* **99**, 022502 (2011).

- [119] A. CASIRAGHI, A. W. RUSHFORTH, M. WANG, N. R. S. FARLEY, P. WADLEY, J. L. HALL, C. R. STADDON, K. W. EDMONDS, R. P. CAMPION, C. T. FOXON, and B. L. GALLAGHER, *Appl. Phys. Lett.* **97**, 122504 (2010).
- [120] L. X. ZHAO, R. P. CAMPION, P. F. FEWSTER, R. W. MARTIN, B. YABER, A. P. KOVARSKY, C. R. STADDON, K. Y. WANG, K. W. EDMONDS, C. T. FOXON, and B. L. GALLAGHER, *Semicond. Sci. Technol.* **20**, 369 (2005).
- [121] X. LIU, W. L. LIM, L. V. TITOVA, M. DOBROWOLSKA, J. K. FURDYNA, M. KUTROWSKI, and T. WOJTOWICZ, *J. Appl. Phys.* **98**, 063904 (2005).
- [122] A. WINTER, H. PASCHER, H. KRENN, X. LIU, and J. K. FURDYNA, *J. Appl. Phys.* **108**, 043921 (2010).
- [123] N. A. SPALDIN and M. FIEBIG, *Science* **309**, 391 (2005).
- [124] W. EERENSTEIN, M. WIORA, J. L. PRIETO, J. F. SCOTT, and N. D. MATHUR, *Nature Materials* **6**, 348 (2007).
- [125] D. CHIBA, F. MATSUKURA, and H. OHNO, *Appl. Phys. Lett.* **89**, 162505 (2006).
- [126] M. H. S. OWEN, J. WUNDERLICH, V. NOVÁK, K. OLEJNÍK, J. ZEMEN, K. VÝBORNÝ, S. OGAWA, A. C. IRVINE, A. J. FERGUSON, H. SIRRINGHAUS, and T. JUNGWIRTH, *New J. Phys.* **11**, 023008 (2009).
- [127] J. WUNDERLICH, A. C. IRVINE, J. ZEMEN, V. HOLÝ, A. W. RUSHFORTH, E. DE RANIERI, U. RANA, K. VÝBORNÝ, J. SINOVA, C. T. FOXON, R. P. CAMPION, D. A. WILLIAMS, B. L. GALLAGHER, and T. JUNGWIRTH, *Phys. Rev. B* **76**, 054424 (2007).
- [128] M. SHAYEGAN, K. KARRAI, Y. P. SHKOLNIKOV, K. VAKILI, E. P. DE POORTERE, and S. MANUS, *Appl. Phys. Lett.* **83**, 5235 (2003).
- [129] S. T. B. GOENNENWEIN, M. ALTHAMMER, C. BIHLER, A. BRANDLMAIER, S. GEPRÄGS, M. OPEL, W. SCHOCH, W. LIMMER, R. GROSS, and M. S. BRANDT, *Phys. stat. sol. (RRL)* **3**, 96 (2008).
- [130] M. OVERBY, A. CHERNYSHOV, L. P. ROKHINSON, X. LIU, and J. K. FURDYNA, *Appl. Phys. Lett.* **92**, 192501 (2008).
- [131] C. BIHLER, M. ALTHAMMER, A. BRANDLMAIER, S. GEPRÄGS, M. WEILER, M. OPEL, W. SCHOCH, W. LIMMER, R. GROSS, M. S. BRANDT, and S. T. B. GOENNENWEIN, *Phys. Rev. B* **78**, 045203 (2008).

- [132] A. CASIRAGHI, A. W. RUSHFORTH, J. ZEMEN, J. A. HAIGH, M. WANG, K. W. EDMONDS, R. P. CAMPION, and B. L. GALLAGHER, *arXiv:1205.3725v1 [cond-mat]* (unpublished).
- [133] V. V. KOCHERVINSKIĬ, *Crystallogr. Rep.* **48**, 649 (2003).
- [134] R. C. BARRETT and C. F. QUATE, *Rev. Sci. Instrum.* **62**, 1393 (1991).
- [135] J. A. HAIGH, A. W. RUSHFORTH, C. S. KING, K. W. EDMONDS, R. P. CAMPION, C. T. FOXON, and B. L. GALLAGHER, *App. Phys. Lett.* **95**, 232102 (2009).
- [136] H. W. SCHUMACHER, C. CHAPPERT, P. CROZAT, R. C. SOUSA, P. P. FREITAS, J. MILTAT, J. FASSBENDER, and B. HILLEBRANDS, *Phys. Rev. Lett.* **90**, 017201 (2003).
- [137] P. E. HOHAGE, J. NANNEN, S. HALM, G. BACHER, M. WAHLE, S. F. FISCHER, U. KUNZE, D. REUTER, and A. D. WIECK, *Appl. Phys. Lett.* **92**, 241920 (2008).
- [138] J. QI, Y. XU, N. H. TOLK, X. LIU, J. K. FURDYNA, and I. E. PERAKIS, *Appl. Phys. Lett.* **91**, 112506 (2007).
- [139] Y. HASHIMOTO, S. KOBAYASHI, and H. MUNEKATA, *Phys. Rev. Lett.* **100**, 067202 (2008).
- [140] E. ROZKOTOVÁ, P. NĚMEC, P. HORODYSKÁ, D. SPRINZL, F. TROJÁNEK, P. MALÝ, V. NOVÁK, K. OLEJNÍK, M. CUKR, and T. JUNGWIRTH, *Appl. Phys. Lett.* **92**, 122507 (2008).
- [141] G. V. ASTAKHOV, A. V. KIMEL, G. M. SCHOTT, A. A. TSVETKOV, A. KIRILYUK, D. R. YAKOVLEV, G. KARCZEWSKI, W. OSSAU, G. SCHMIDT, L. W. MOLENKAMP, and T. RASING, *Appl. Phys. Lett.* **86**, 152506 (2005).
- [142] C. KITTEL, *Phys. Rev.* **110**, 836 (1958).
- [143] O. Y. BELYAEVA, S. N. KARPACHEV, and L. K. ZAREMBO, *Usp. Fiz. Nauk* **162**, 107 (1992).
- [144] J. WANG, Y. HASHIMOTO, J. KONO, A. OIWA, H. MUNEKATA, G. D. SANDERS, and C. J. STANTON, *Phys. Rev. B* **72**, 153311 (2005).
- [145] J. QI, J. A. YAN, H. PARK, A. STEIGERWALD, Y. XU, S. N. GILBERT, X. LIU, J. K. FURDYNA, S. T. PANTELIDES, and N. TOLK, *Phys. Rev. B* **81**, 115208 (2010).

- [146] L. THEVENARD, E. PERONNE, C. GOURDON, C. TESTELIN, M. CUBUKCU, E. CHARRON, S. VINCENT, A. LEMAÏTRE, and B. PER-  
RIN, *Phys. Rev. B* **82**, 104422 (2010).
- [147] A. V. SCHERBAKOV, A. S. SALASYUK, A. V. AKIMOV, X. LIU, M. BOMBECK, C. BRÜGGEMANN, D. R. YAKOVLEV, V. F. SAPEGA, J. K. FURDYNA, and M. BAYER, *Phys. Rev. Lett.* **105**, 117204 (2010).
- [148] M. BOMBECK, A. S. SALASYUK, B. A. GLAVIN, A. V. SCHERBAKOV, C. BRÜGGEMANN, D. R. YAKOVLEV, V. F. SAPEGA, X. LIU, J. K. FURDYNA, A. V. AKIMOV, and M. BAYER, *arXiv:1121.3394v1 [cond-mat]* (unpublished).
- [149] T. L. LINNIK, A. V. SCHERBAKOV, D. R. YAKOVLEV, X. LIU, J. K. FURDYNA, and M. BAYER, *Phys. Rev. B* **84**, 214432 (2011).
- [150] S. DAVIS, A. BARUTH, and S. ADENWALLA, *Appl. Phys. Lett.* **97**, 232507 (2010).
- [151] A. CASIRAGHI, P. WALKER, A. V. AKIMOV, K. W. EDMONDS, A. W. RUSHFORTH, E. DE RANIERI, R. P. CAMPION, B. L. GALLAGHER, , and A. J. KENT, *Appl. Phys. Lett.* **99**, 262503 (2011).
- [152] R. BERMAN, *Thermal conduction in solids*, 1976.
- [153] R. J. VON GUTFELD and A. H. NETHERCOT, *Phys. Rev. Lett.* **12**, 641 (1964).
- [154] M. N. WYBOURNE and J. K. WIGMORE, *Rep. Prog. Phys.* **51**, 923 (1988).
- [155] R. J. VON GUTFELD, *Physical acoustics*, volume 5, W. P. Mason, Academic, New York, 1968.
- [156] B. TAYLOR, H. J. MARIS, and C. ELBAUM, *Phis. Rev. Lett.* **23**, 416 (1969).
- [157] G. A. NORTHROP and J. P. WOLFE, *Phis. Rev. Lett.* **43**, 1424 (1979).
- [158] [HTTP://EN.WIKIPEDIA.ORG/WIKI/PICOSECOND\\_ULTRASONICS](http://en.wikipedia.org/wiki/Picosecond_ultrasonics).
- [159] C. THOMSEN, J. STRAIT, Z. VARDENY, H. J. MARIS, and J. TAUC, *Phys. Rev. Lett* **53**, 989 (1984).
- [160] H. Y. HAO and H. J. MARIS, *Phis. Rev. B* **63**, 224301 (2001).
- [161] G. TAS and H. J. MARIS, *Phys. Rev. B* **49**, 15046 (1994).
- [162] G. GIULIANI, *Europhys. Lett.* **81**, 60002 (2008).

- [163] A. J. KENT, R. E. STRICKLAND, K. R. STRICKLAND, and M. HENINI, *Phys. Rev. B* **54**, 2019 (1996).
- [164] J. P. WOLFE, *Imaging phonons: acoustic wave propagation in solids*, 1998.
- [165] S. TAMURA, *Phys. Rev. B* **31**, 2574 (1985).
- [166] T. MORITA, Y. WAGATSUMA, Y. CHO, H. MORIOKA, H. FUNAKUBO, and N. SETTER, *Appl. Phys. Lett.* **84**, 5094 (2004).
- [167] W. S. AHN, W. W. JUNG, and S. K. CHOI, *J. Appl. Phys.* **99**, 014103 (2006).